Design of Shape-Morphing Structures Based on Smart Materials

Mechanically Intelligent Structures

Master thesis

Tarish Virash Ghaurish Kalpoe

Delft University of Technology

TU Delft

Design of Shape-Morphing Structures Based on Smart Materials

Mechanically Intelligent Structures

by

Tarish Virash Ghaurish Kalpoe

in partial fulfilment of the requirements for the degree of

Master of Science

in Mechanical Engineering

at the Department of Maritime and Transport Technology of Faculty Mechanical Engineering of Delft University of Technology.

To be defended publicly on Monday, March 3rd, 2025 at 14:00.

Student number:	4549317	
MSc Track:	Multi-Machine Engineering	
Report number:	2024.MME.8895	
Thesis Committee:	Qianyi (Aaron) Chen	TU Delft Supervisor, ME
	Dr. Jovana Jovanova	TU Delft Committee chair, ME
	Dr. Sid Kumar	TU Delft Committee, Me
Date:	February 18th, 2025	

An electronic version of this thesis is available at `http://repository.tudelft.nl/`.

Cover: Picture of a 3D printed SMP geometry taken by the Author

TU Delft

“Life without knowledge is death in disguise.”

– Talib Kweli Greene

Preface

Dear Reader,

This thesis represents the culmination of my academic journey at Delft University of Technology, where I pursued a Master's degree in Mechanical Engineering with a specialisation in the Multi-Machine Engineering track. What began as a simple research assignment evolved into a full thesis project, ultimately resulting in the publication of two research papers. This journey has been both challenging and rewarding, filled with opportunities to grow as a researcher and an engineer.

The topic of my thesis, "*Shape-Morphing Structure Made of Smart Materials Applied in an Actuator*", provided me with the opportunity to showcase my creativity in 3D modelling and design while deepening my knowledge of materials and their applications. Throughout this project, I gained significant expertise in modelling and developed a deeper understanding of material behaviour in engineering simulations.

I would like to express my sincere gratitude to my supervisors, Q. Chen and Dr J. Jovanova, for their invaluable guidance, encouragement, and expertise throughout this process. Aaron, in particular, introduced me to the fascinating world of Smart Materials, and his enthusiasm and insights have greatly influenced my academic growth. Their support and feedback have been instrumental in shaping my work, motivating me to strive for excellence, and ultimately achieving two published papers.

A special and heartfelt acknowledgement goes to my mother, G. Goelella, whose unwavering support, unconditional love, and tireless encouragement have been the foundation of my success. Your sacrifices and belief in me have been a constant source of strength throughout my academic journey, and I am forever grateful for everything you have done to make this possible. This achievement is as much yours as it is mine.

I would also like to express my gratitude to A. Alsudani, K. Beyina, R. Jagernath, Y. Jokhoe, J. Ramautar and A. Sitaram for their invaluable support throughout the completion of this thesis. Your encouragement, insights, and assistance have been instrumental in helping me navigate the challenges of this work, and I truly appreciate your contributions.

I am also grateful to my friends, family, and colleagues who have supported me throughout this journey. Your encouragement and belief in me, in ways big and small, have made a meaningful difference.

As I conclude this chapter, I look forward to the opportunities and challenges that lie ahead. I hope that this thesis not only demonstrates my creativity and technical skills but also serves as a foundation for further advancements in engineering design and innovation.

Tarish Virash Ghaurish Kalpoe
Delft, February 2025

Summary

This research investigates the design and development of shape-morphing structures using smart materials, including hydrogels, Shape Memory Polymers (SMPs), and Shape Memory Alloys (SMAs), with applications in soft robotics. By leveraging the unique properties of these materials, the study aims to develop adaptive and responsive structures capable of controlled deformation, providing solutions for robotics, biomedical devices, and adaptive engineering systems. The main research question guiding this study is:

"How can smart materials be used to develop a shape-morphing structure applied to soft actuators?"

To address this research question, a theoretical foundation was laid, and modelling techniques for shape-morphing structures using smart materials specifically hydrogels, SMPs, and SMAs were explored. These materials enable controlled and reversible deformations in response to external stimuli, making them ideal for applications in soft robotics, aerospace, and biomedical engineering. The role of morphology in shaping deformation behaviour was examined, highlighting how geometric configurations influence structural adaptability. Finite Element Analysis (FEA) was introduced as the primary tool for modelling and predicting material behaviour, facilitating the optimisation of shape-morphing actuators. The research further investigates how smart materials can be structured, actuated, and combined to achieve efficient morphing while ensuring stability, functionality, and durability. Special emphasis is placed on bending deformation as a key performance indicator (KPI) for evaluating actuator efficiency.

Hydrogels were extensively examined for their stimuli-responsive properties, particularly their ability to swell and deform in response to external factors such as temperature changes. Various hydrogel-based structures were modelled, including ball-to-ball setups, flexible fingers, can structures, and surface grids. The results highlighted the critical role of geometric arrangements in determining deformation characteristics—symmetrical designs facilitated smooth and predictable morphing, whereas denser frameworks provided controlled folding and structural integrity. Material orientation significantly influenced deformation directionality, while overall structure length impacted computational complexity without drastically affecting morphing efficiency. A maximum expansion factor of 1.37 in diameter and 2.59 in volume at 275 K was observed, demonstrating the potential for substantial volumetric change in shape-morphing applications.

For SMPs and SMAs, structural configurations were explored to enhance shape-morphing efficiency. A key development was the integration of the intelligent building block into a cylindrical geometry, designed for precise and controlled deformation. Material properties were analysed to identify factors influencing mechanical response, and constitutive equations were implemented in Abaqus to simulate thermo-mechanical behaviour under various loading and thermal conditions. Geometric parameters, including block width (B_w), block height (B_h), segment ratio (R_s), and cylinder thickness (C_t), were systematically optimised, revealing key interactions that affect morphing performance. Taller and wider blocks increased bending, while higher segment ratios and thicker cylinders exhibited reduced deformation. A Design of Experiments (DoE) methodology confirmed that geometric tuning enhances shape-morphing effectiveness. This design also showed that the maximum bending angle achievable was 60.0 degrees. Additional studies on cylinder orientations relative to the actuation direction demonstrated that minor misalignments had minimal impact on bending performance. Various geometric alternatives, including square, circular, elliptical, and hexagonal shapes, were evaluated, though the intelligent building block remained the most effective for precise, scalable deformation. Multi-cylinder configurations demonstrated multi-directional morphing, expanding the versatility of these materials for dynamic applications.

The integration of SMPs, SMAs, and hydrogels into a unified shape-morphing framework underscores the potential of smart materials for advanced robotic and engineering applications. This study not only provides a strong theoretical foundation for the controlled actuation of these materials but also presents practical design principles for their implementation in soft robotic actuators, bio-inspired devices, and

adaptable structures. By bridging theoretical principles with experimental validation, this research lays the groundwork for future advancements in smart material-based technologies.

Future studies should focus on further optimising material properties, exploring hybrid actuation mechanisms, and incorporating torsional deformation to expand the capabilities of shape-morphing structures. Additionally, integrating these systems with external control feedback and real-world testing will be crucial for transitioning smart material actuators from simulation to real-world applications, particularly in soft robotics and adaptive mechanical systems.

Keywords: soft robotics, shape-morphing actuator, SMA, SMP, hydrogel, smart materials, FEA.

Contents

List of Figures

List of Tables

Nomenclature

Abbreviations

Abbreviation	Definition
BC	Boundary condition
CAD	Computer-Aided Design
DoE	Design of Experiments
FEA	Finite Element Analysis
FEM	Finite Element Method
LCST	Lower Critical Solution Temperature
PLA	Polylactic acid
PVC	Polyvinyl chloride
PMMA	Poly(methyl methacrylate)
PNIPAM	Poly(N-isopropylacrylamide)
SE	Superelasticity
SME	Shape Memory Effect
SMA	Shape Memory Alloy
SMC	Shape Memory Ceramic
SMM	Shape Memory Material
SMP	Shape Memory Polymer
UCST	Upper Critical Solution Temperature

Symbols

Symbol	Definition	Unit
B_w	Block width of the folding block	[mm]
B_h	Block height of the folding block	[mm]
C_t	Cylinder thickness	[mm]
R_x	Rotation in the x-direction	[-]
R_y	Rotation in the y-direction	[-]
R_z	Rotation in the z-direction	[-]
R_s	Segment ratio folding block	[-]
T	Temperature	[K]
T_g	Glass Temperature	[K]
T_{trans}	Transition Temperature	[K]
m	Mass	[kg]
F	Force	[N]
K_B	Boltzmann constant	[-]
U_x	Displacement in the x-direction	[mm]
U_y	Displacement in the y-direction	[mm]
U_z	Displacement in the z-direction	[mm]
ρ	Density	[kg/m^3]
λ	Principle stretch	[-]
ϕ	Bending angle hydrogel models	[deg]
$\phi^\star$	Specific bending angle hydrogel models	[deg]
θ	Bending angle SMP models	[deg]
ψ	Orientation angle SMP models	[deg]

1

Introduction

1.1. Background

In recent years, the field of robotics has evolved beyond traditional rigid mechanisms to embrace soft robotics. This resulted in a transformative approach inspired by natural flexibility and adaptability. Unlike conventional robots, soft robots are designed from compliant materials that can bend, stretch, and conform to diverse shapes, allowing them to perform tasks in complex, dynamic environments [1, 2]. This shift is essential in applications that require safe human interaction, precision in handling delicate objects, or adaptability to unpredictable spaces. Examples include medical devices, agricultural automation, and search-and-rescue operations.

A key innovation driving the advancement of soft robotics is shape-morphing structures, which are systems capable of changing their shape, configuration, or mechanical properties in response to external stimuli such as temperature, light, or humidity. The desire to emulate the shape-changing capabilities mastered by nature over billions of years has spurred the development of these artificial structures [3]. Shape-morphing structures offer unique advantages in their ability to adapt to dynamic environments and simplify mechanical systems by replacing traditional rigid components with smart materials. These capabilities make them critical for addressing real-world challenges in sectors that demand flexibility, precision, and resilience.

These structures are powered by smart materials such as shape memory alloys (SMAs), shape memory polymers (SMPs), and hydrogels, which respond predictably to environmental changes, enabling dynamic adaptability without rigid mechanical systems [4–6]. Together, soft robotics and shape-morphing structures address the growing demand for technologies that can operate autonomously, navigate diverse and unstructured environments, and maximise efficiency across sectors. By significantly reducing energy consumption and mechanical complexity, these innovations align with global trends in sustainability, automation, and miniaturisation, making them indispensable for next-generation systems.

Fields such as robotics [7], biomedical engineering [8], aerospace [9, 10], automotive [11] and civil infrastructure [12] are already witnessing the potential of smart materials to enhance adaptability and resilience. For instance, in robotics, shape-morphing grippers can safely handle fragile or irregular objects, while in aerospace, morphing wings enhance aerodynamics and fuel efficiency [13]. By utilizing smart materials, such as hydrogels, SMPs, and SMAs, engineers can design responsive structures that integrate seamlessly into both autonomous and human-assisting systems. By enabling the development of more effective, flexible, and responsive systems, these materials have the potential to revolutionize conventional engineering techniques [14]. The creation and deployment of shape-morphing structures represent a major step forward in meeting the demands of our increasingly automated and connected world.

1.2. Research objective

The objective of this research is to design shape-morphing structures using smart materials such as hydrogels, SMPs, and SMAs to develop mechanically intelligent systems with potential applications in robotics. This study emphasises both design and optimisation, aiming to create adaptable structures for real-world scenarios. A critical component of this research is the use of finite element analysis (FEA) simulations to predict the behaviour of these materials under various conditions. FEA provides a robust framework for understanding the interplay between material properties, geometric morphology, and deformation precision, enabling improvements in the efficiency and durability of shape-morphing structures.

Looking at the above, this study seeks to answer the primary research question:

> ***How can smart materials be used to develop a shape-morphing structure applied into soft actuators?***

These sub-questions are designed to systematically guide the research towards answering the main. However, it is worth noting that the research is split into the third and fourth chapters. Meaning that these chapters are structured parallel to approach the main research question.

What types of smart materials are appropriate to use for a shape-morphing actuator?

This subquestion will be answered with a literature review to understand the types of smart materials that have properties that can be tailored and to see which of these are most applicable for shape-morphing and how to formulate a strategy to translate a material into a design.

How can a model-based design framework be implemented to model and predict the behaviour of structures with integrating smart materials? This subquestion will be in Chapter 2 answered with a literature review on FEA modelling and constitutive equations used to implement the behaviour of these materials.

How can shape-morphing structures be developed by using smart materials?

This will be answered in Chapter 4 by designing multiple configurations and adjusting these configurations and geometries based on a case found in the literature.

How can multiple smart materials be integrated into the shape-morphing structure with multiple functionalities?

This will be answered in Chapter 5 by following a design process to produce an integrated structure with multiple Shape memory materials and adjusting parameters in the design to improve shape-morphing.

1.3. Research scope

The scope of this research is focused exclusively on bending deformation as the primary mode of interest. Other deformation modes, such as linear extension, torsion, or spiral twisting, fall outside the scope and are not considered in this study. Additionally, force analysis or evaluations of load-bearing capacity are not included. Instead, the research is limited to the deformation behaviour of these structures, with simulations and validations performed using FEA to model and experimentally assess bending angles and deformation patterns. This focused approach provides a comprehensive understanding of how material properties and morphology influence bending performance, laying the groundwork for advancing shape-morphing systems for practical applications.

1.4. Methodology

An overview of the methodology followed in this thesis is presented in Figure 1.1. The methodology is designed to address the research questions systematically and serves as a roadmap for this thesis. The overarching objective of this thesis is to develop shape-morphing structures by using smart materials suitable for practical applications. The study begins with a comprehensive literature review to investigate the properties, applications, and modelling techniques of smart materials, focusing on

their potential for developing shape-morphing structures. This review establishes a foundational understanding of the theoretical concepts and identifies key gaps in the existing research.

Subsequently, the research transitions to computational modelling and simulation, utilising finite element methods (FEM) to analyse and optimise material behaviour. Two primary case studies are explored: one focusing on hydrogel-silicone configurations, and the other on SMPs combined with SMAs. Each case involves a detailed mesh sensitivity analysis, parameter studies, and convergence assessments to ensure simulation reliability. Key mechanical outputs, such as bending angles and deformation patterns, are examined for various configurations and geometries.

The methodology also incorporates exploratory simulations of alternative designs and loading scenarios, including variations in geometry and the addition of new parameters to evaluate torsion and orientation effects. Practical considerations, such as computational efficiency and scalability, are assessed throughout the study.

Finally, the results are analysed to derive insights into the potential applications of smart materials in shape-morphing structures. The thesis concludes with a synthesis of findings, along with recommendations for future research directions.

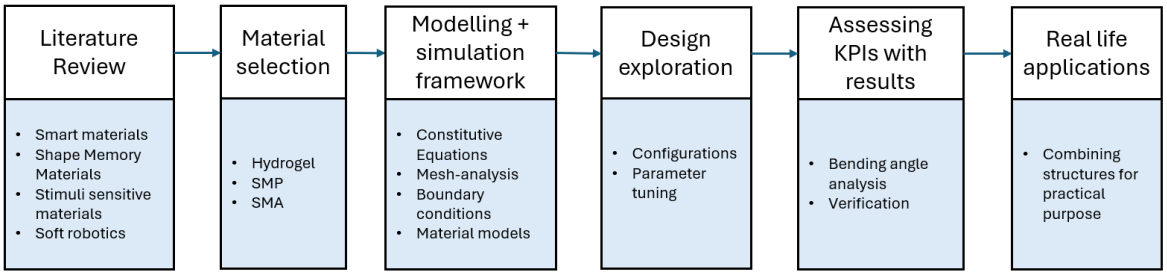

Figure 1.1: Schematic representation of the research methodology, detailing the sequential stages from literature review to future applications.

1.5. Thesis outline

The outline of this thesis is structured as follows. Chapter 1 introduces the research by outlining the main question, highlighting the motivation for exploring shape-morphing structures, and presenting the research objective and scope. Chapter 2 provides a literature review that explores relevant methodologies and approaches, discusses the properties and applications of smart materials, and examines their role in soft robotics and morphology. 4 focuses on hydrogel-based systems, detailing the constitutive equations, modelling approaches, and simulation results to understand their deformation behaviour. 5 shifts to shape memory polymers (SMPs) and shape memory alloys (SMAs), presenting their configurations, designs, modelling techniques, and results. Together, Chapters 4 and 5 offer a comprehensive analysis of two distinct material systems for shape morphing. Finally, Chapter 6 concludes the thesis by summarising key findings, discussing implications, and providing recommendations for future research.

2

Literature Review of materials applied in shape-morphing structures

This chapter provides a comprehensive exploration of the theoretical foundation and current state of knowledge relevant to this research. It begins by reviewing the properties, applications, and modelling techniques of smart materials, with a particular focus on their potential for developing shape-morphing structures. By examining various classes of smart materials, including hydrogels, SMAs, and SMPs, this chapter highlights their unique characteristics, activation mechanisms, and relevance to applications in robotics, aerospace, and biomedical engineering. Furthermore, the implementation of FEA in this study is discussed, detailing its role in modelling and predicting the behaviour of shape-morphing structures. The concept of shape morphing is explored in depth, including its advantages over traditional rigid-link mechanisms and its integration into soft robotics. It is worth noting that sections of this chapter are published in [15], underscoring its contribution to the broader scientific community.

2.1. Smart materials

Smart materials play a crucial role in this research, as they are central to the design and functionality of the proposed systems. Given their significance, it is important to explore their characteristics in more detail. This section examines various types of smart materials, discussing their properties, activation mechanisms, and applications in several fields.

2.1.1. Classification of Smart Materials

Smart materials, also known as intelligent or responsive materials, are materials that exhibit adaptive or dynamic properties in response to external stimuli such as temperature, light, pressure, electric fields, or magnetic fields [12, 16]. These materials can be classified into several categories based on their underlying mechanisms and functionalities. The inner workings of smart materials are mimicking biological systems, which is shown in Figure 2.1. Smart materials gather information from their surroundings by sensing and creating chemical or physical effects for brain decision-making control [17]. Smart materials are classified to provide a systematic framework for understanding and categorizing their unique properties and behaviours. By categorizing smart materials, specific applications are achievable by tailoring the design and optimizing the performance of smart materials.

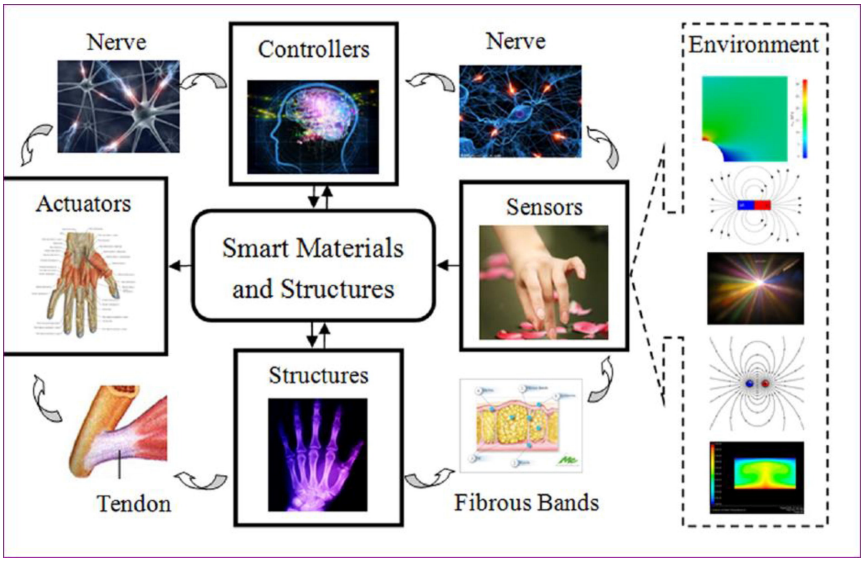

Figure 2.1: Principle of smart materials compared to humans [17].

The most significant distinction made in smart materials is between the main classes 'active' and 'passive' [5, 11]. Passive smart materials are responsive to external stimuli but do not actively generate a response. Instead, their properties change passively in reaction to specific environmental conditions. Passive materials can transfer energy, for instance when used as fibre optic [18, 19]. However, while being 'smart', they do not possess the characteristics to transduce energy. They are mostly used to function as a sensor instead of an actuator or transducer [20]. Subsequently, active materials can change their characteristics when exposed to external effects. Furthermore, some of the active smart materials can convert energy from one form such as thermal, mechanical or chemical to another form. Active smart materials possess some properties which distinguish them from other materials such as immediacy: short response time, self-actuation: form and shape can be changed due to external stimuli, self-diagnostic: imperfections or cracks can be detected and self-healing: materials can repair themselves when damaged.

2.1.2. Common Smart Materials:

The field of smart materials is diverse and continuously evolving, with new materials and functionalities being discovered and developed. Overall, the classification of smart materials promotes efficient utilization, integration, and advancement in various industries. A summarized overview can be found in Table 2.1 among others with their respective outputs and inputs.

Below is an overview of widely used smart materials, highlighting their properties and key uses.

Piezoelectric materials generate an electric charge under mechanical stress and deform when an electric field is applied. These materials must be dielectric and lack a centre of symmetry [21, 22]. The direct effect involves charge generation from mechanical forces, while the inverse effect involves deformation from an electric charge. They are widely used in actuators, sensors, and energy harvesting devices, particularly in automotive systems and flexible devices [23, 24].

Photostrictive materials deform under light exposure by combining piezoelectric and photovoltaic properties [25, 26]. Through the photovoltaic effect, these materials generate an electric charge, which then triggers deformation via the piezoelectric effect. Their wireless actuation capability eliminates the need for external power sources, making them suitable for remote-controlled systems like microelectrochemical systems (MEMS), solar energy devices, and actuators [27, 28].

Electrostrictive materials deform in response to an electric field due to the alignment of electric dipoles [29]. Their rapid response and precision make them ideal for applications in robotics, aerospace, and biomedical engineering. These materials are used in advanced devices like actuators, sensors, and tunable lenses [30].

Table 2.1: Smart material types with their respective inputs and outputs [15]

Material	Input	Output
Piezoelectric	Electric field	Mechanical strain
	Mechanical load	Electric potential
Photostrictive	Incident light	Mechanical strain
Magnetostrictive	Magnetic field	Mechanical strain
	Mechanical load	Magnetization
Electrostrictive	Electric field	Mechanical strain
	Mechanical load	Electric potential
Thermoelectric	Thermal load	Electric potential
	Electric field	Temperature change
Shape memory materials	Thermal load Magnetic load	Mechanical strain
Photovoltaic	Incident light	Electric potential
Magneto- Electro- } rheological fluids	Magnetic field Electric field	Mechanical strain
Photo- Thermo- Magneto- Electro- } chromic	Incident light Thermal load Magnetic field Electric field Mechanical load	Colour change

Magnetostrictive materials deform under magnetic fields as their magnetic domains align [31]. Terfenol-D, made of terbium, dysprosium, and iron, is a widely used example due to its significant magnetostrictive properties [32]. These materials are ideal for high-precision actuators, sensors, and energy harvesters. Their ability to deliver high force output and fast response times is critical in robotics and adaptive structures [33].

Thermoelectric materials convert heat into electricity using their unique combination of high electrical conductivity and low thermal conductivity [34, 35]. These properties make them suitable for harnessing waste heat in industrial and automotive processes, enabling power generation in remote or compact settings [36, 37].

Electrochromic materials undergo reversible optical changes under electrical stimulation [38]. Found in smart windows, displays, and privacy glass, these materials adjust transparency and colour via ion migration. Their energy efficiency and adaptability make them essential for glare reduction and customizable shading applications [39].

Photochromic materials alter their optical state under specific light wavelengths, changing colour or transparency [40]. Commonly used in lenses and windows, their reversible chemical rearrangements provide real-time light adaptation, such as darkening in sunlight and clearing in lower light [41].

Electro-rheological (ERFs) and magneto-rheological fluids (MRFs) change viscosity under electric or magnetic fields [42, 43]. ERFs are used in vibration isolators and automotive components, while MRFs are commonly applied in dampers, clutches, and manufacturing processes [44, 45].

In Figure 2.2 some applications can be found regarding the main classes mentioned.

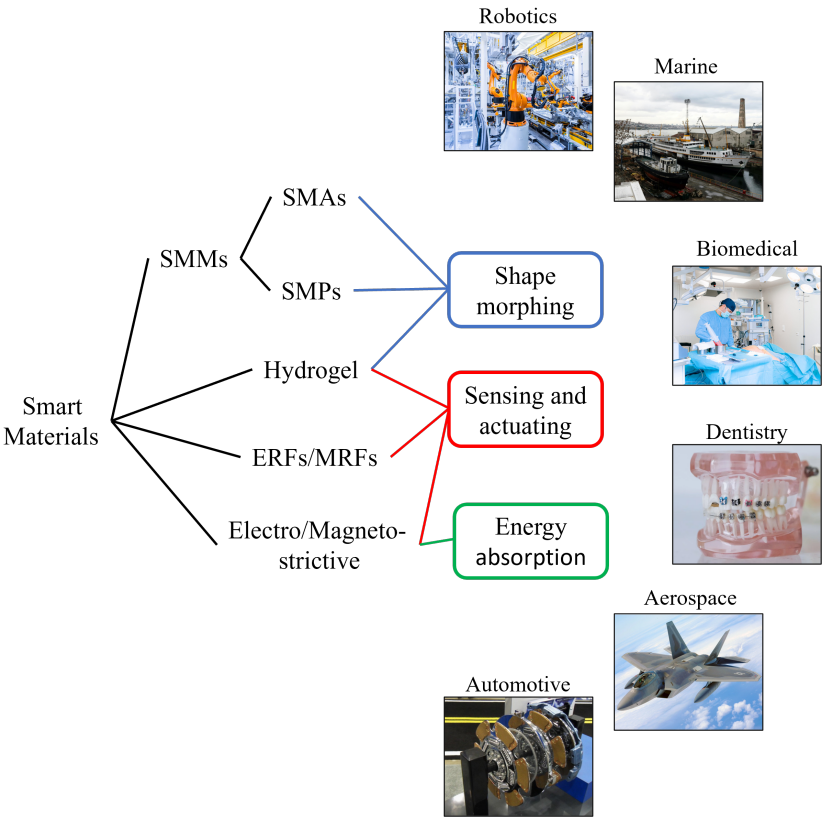

Figure 2.2: Potential applications of the main types of smart materials.

The materials hydrogels, SMAs, and SMPs will be more prominent in this research. Therefore, these are explained here in greater detail.

Hydrogel

Hydrogels are three-dimensional networks of polymer chains capable of absorbing and retaining significant amounts of water or other solvents. As smart materials, they exhibit notable swelling or shrinking in response to environmental stimuli such as temperature, pH, light, or specific chemicals [46]. Hydrogels can be formed through various physical interactions or chemical reactions, with the specific synthesis method tailored to the intended application [47]. This versatility has enabled their use across a wide range of fields. For example, photoresponsive hydrogels have been developed to mimic the dynamic nature of living tissues, responding to biomechanical changes [48]. More recently, hydrogels have found applications in electronics and electronic devices, leveraging their unique properties for innovative designs [49]. They are also utilized as gel actuators and in water-blocking materials for agricultural and biochemical applications [50–52].

Hydrogels operate based on the Shape Change Effect (SCE), unlike materials that rely on the Shape Memory Effect (SME). The SCE occurs when the transition between two states happens instantaneously or nearly instantaneously, requiring little to no energy barrier. In contrast, the SME involves a higher energy barrier, necessitating additional energy to achieve the transition. Depending on the operating environment, a material may exhibit either the SME or the SCE. Hydrogels, by this definition, are water-responsive materials governed by the SCE. This distinction is illustrated schematically in Figure 2.3.

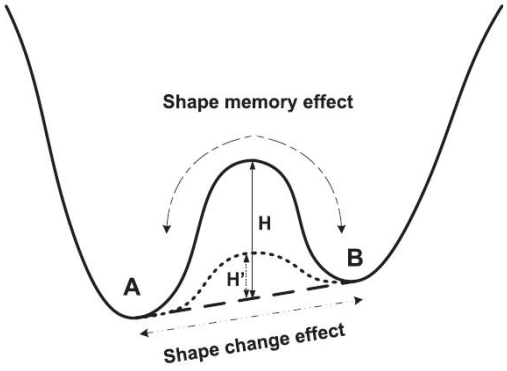

Figure 2.3: Visualization of two energy states of a material (A and B), with H and H_0 indicating the different energy barrier levels [50].

Despite their versatility, hydrogels face challenges that limit their broader use. Key areas for improvement include reducing their sensitivity to environmental conditions to maintain consistent properties and addressing deterioration caused by repeated swelling and shrinking cycles. Ongoing research aims to overcome these limitations and further expand the potential applications of hydrogel-based systems [53].

PNIPAM hydrogel

Thermoresponsive hydrogels made from thermosensitive polymers are extensively studied, simplified in Figure 2.5. These polymers can exhibit either negative or positive thermosensitivity. Polymers with negative thermosensitivity have a Lower Critical Solution Temperature (LCST) and contract when the temperature rises above this critical point. Conversely, positively thermosensitive polymers have an Upper Critical Solution Temperature (UCST) and contract as the temperature decreases below their critical value [54]. More accurately, around the critical temperature, the polymer in solution undergoes a phase shift from a soluble to an insoluble state. Among the various types of hydrogels, PNIPAM hydrogels, made from poly(N-isopropylacrylamide), stand out for their unique thermosensitive behaviour. PNIPAM hydrogels exhibit an LCST of approximately 32–35°C in water. Below this temperature, the polymer chains are hydrophilic, enabling the hydrogel to swell significantly as it absorbs water. Above the LCST, the polymer becomes hydrophobic, causing the hydrogel to expel water and collapse into a compact, dense structure. This phase transition is reversible, allowing PNIPAM hydrogels to alternate between swollen and collapsed states based on temperature changes [55]. Even under pressure, the absorbed water can almost not be removed. This unique behaviour places PNIPAM hydrogels in the category of “smart” or responsive hydrogels. Their ability to adapt to temperature changes has opened doors to numerous applications. In biomedical engineering, for instance, they are used in drug delivery systems, where temperature changes can trigger controlled drug release, and in tissue engineering, as scaffolds that mimic the properties of soft tissues [56, 57]. In addition, PNIPAM plays a critical role in soft robotics, where their responsiveness to environmental conditions and mechanical flexibility is particularly advantageous [58, 59]. An overview of applications for PNIPAM hydrogels can be found in Figure 2.4.

However, PNIPAM hydrogels are not without challenges [60]. There is slow thermoresponsive behaviour, which is caused by the formation of an impenetrable surface structure that hinders water flow during the collapse. Moreover, their long-term stability, especially in biomedical applications, can be a concern, requiring chemical modifications to ensure consistent performance over time. Lastly, their mechanical strength is often limited, necessitating the integration of reinforcing materials or crosslinking agents to improve durability [61].

Shape Memory Materials (SMMs)

SMMs have the ability to “remember” their original shape and recover it when subjected to certain stimuli such as heat, stress, or magnetic fields, this mechanism is also known as the Shape Memory Effect (SME) [62]. SMMs are one of the most commonly used intelligent materials for industrial purposes.

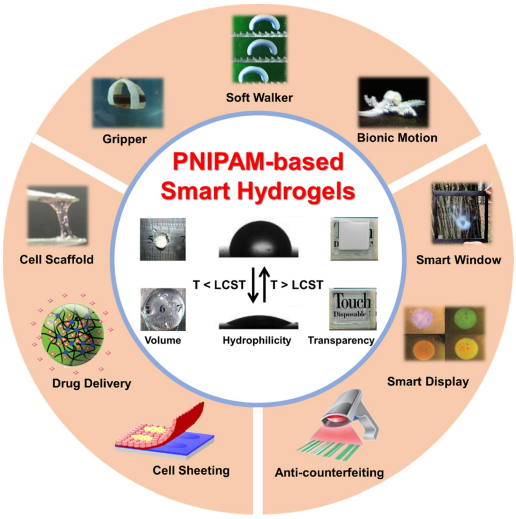

Figure 2.4: Overview of PNIPAM applications as found in [61].

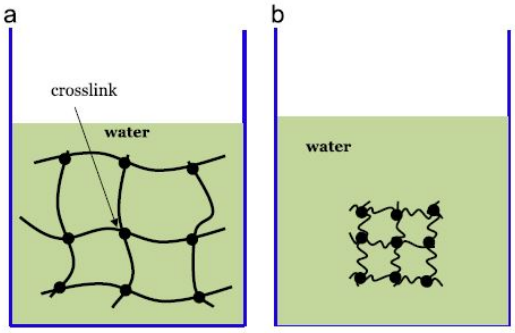

Figure 2.5: Schematics of a temperature-sensitive hydrogel as mentioned in [55].

SMMs have a lot of common groups such as SMAs, SMPs and Shape Memory Ceramics (SMCs) [6, 63]. These common groups will be discussed in the sections below.

(1) Shape Memory Alloys (SMAs)
SMAs are a remarkable class of smart materials known for their ability to recover a pre-defined shape after being deformed [64]. This shape recovery is triggered by external stimuli, most commonly heat, and is rooted in a solid-state phase transformation. Few applications of SMAs can be found in industrial engineering [65]. SMAs are utilized to strengthen concrete beams in structural applications to decrease damage caused by corrosion, fire or mechanical loads [66]. In the aerospace sector, SMAs could be potentially used as sensors and controls [67]. In the marine industry, SMAs can be used in the shipyard for manufacturing and combining pipes [68]. Also, they are used for operating undersea vehicles which are based on change of shape. An overview of some applications is given in Figure 2.6.

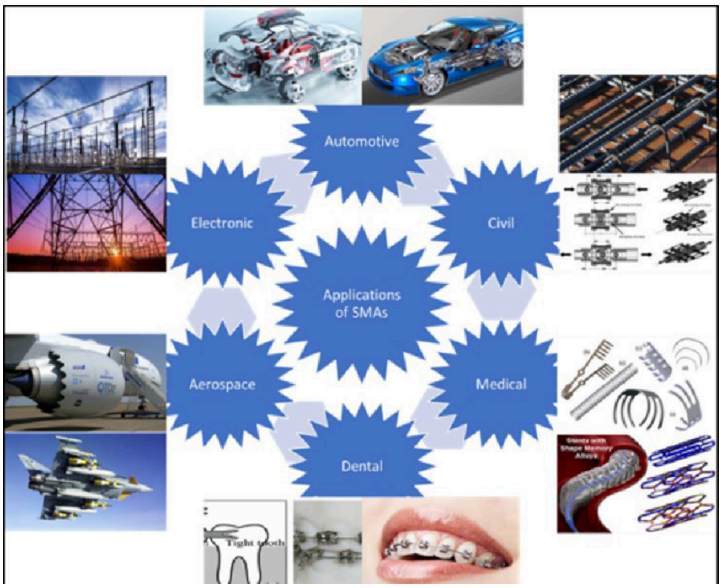

Figure 2.6: Overview of applications of shape memory alloys [65].

SMAs are advanced materials characterized by their ability to recover a predefined shape after deformation through thermal or mechanical stimuli. This behaviour is primarily governed by a reversible

phase transformation between two solid-state structures. At high temperatures, the crystalline structure of the material is densely packed, having a hexagonal lattice (austenite). While at low temperatures, the structure is more loose having a body-centred lattice resulting in Martensite, making the material easier to be deformed. this is also depicted in Figures 2.7 and 2.8.

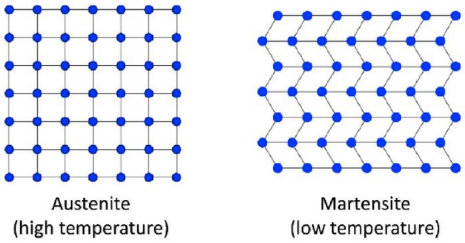

Figure 2.7: Crystalline structure of SMAs at different temperatures [63].

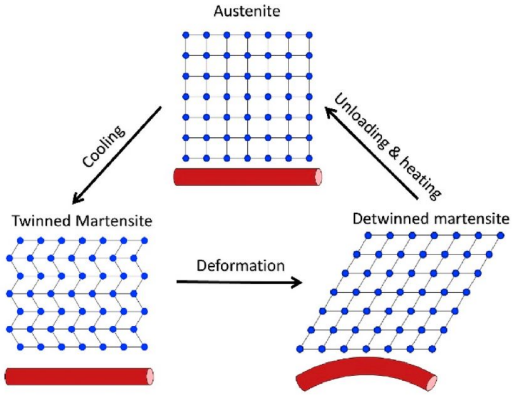

Figure 2.8: Basic mechanism of the Shape Memory Effect for SMAs [63].

SMAs exhibit two distinct and highly useful features: SME and SE [69]. The SME occurs when an SMA is deformed in its low-temperature martensitic phase and then heated. This heating triggers a phase transformation to the high-temperature austenitic phase, enabling the material to recover its original shape. This effect is particularly valuable in applications requiring precise and repeatable movements, as it allows the SMA to provide controlled motion and force.

Superelasticity on the other hand, occurs when SMAs are loaded in their high-temperature austenitic phase. During this process, the material can endure significant strains—up to 8-10%—and fully recover its original shape upon unloading. This behaviour results from stress-induced martensitic transformations that reverse upon removal of the load. SE not only enables SMAs to recover from large deformations but also allows them to store and release energy efficiently.

These remarkable properties stem from the unique crystallographic reorientation and phase transformation mechanisms of SMAs, which facilitate high force generation during shape recovery and enable repeated deformation and restoration cycles without degradation. These characteristics make SMAs indispensable for applications requiring energy absorption, precise actuation, and adaptability [70]. Furthermore, applications can be found in the biomedical field as dental diagnosis or neurosurgical stents [71, 72]. Yet, SMAs also face difficulties in their potential applications. One of the biggest improvements can be made in the high costs associated with SMAs made from nickel-titanium, they are expensive and difficult to manufacture [5, 63].

(2) Shape Memory Polymers (SMPs)

A specific type of SMM is the SMP. SMPs maintain a permanent shape at room temperature, when exposed to a higher transition temperature they deform. After cooling down, the initial shape/form is obtained. Currently, the SME can be activated in SMPs by essentially three types of external stimuli, which consist of heat (thermo-responsive SMPs), chemicals (chemoresponsive SMPs) and the last one being light (photo-responsive and photo-thermal responsive SMPs) [73]. However, most SMPs are thermally responsive [74].

Applications are mostly affiliated with heat-shrinkable objects, such as heat-shrinkable tubes or labels. Examples of more high-tech devices include self-deployable hinges or biomedical devices, such as smart surgery devices [75, 76]. SMPs allow for more deformation compared to SMAs, lower costs, tunable stiffness and ease of fabrication. Recently, the mechanical properties have been improved enormously due to the reinforcement with other materials, leading to SMPs gain more attention [63].

Furthermore, new research on the effect of printing parameters on SMPs has been conducted, leading to a broader aspect for future applications [77].

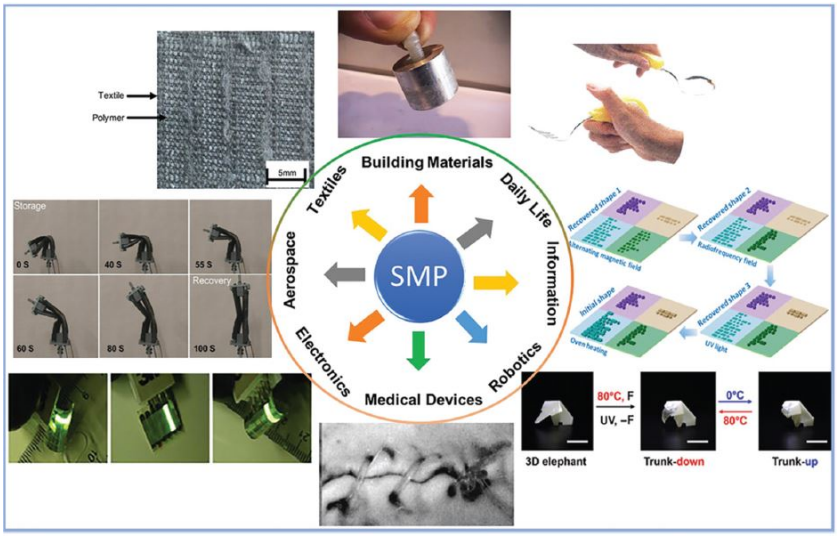

Figure 2.9: Overview of applications of shape memory polymers [76].

Currently, many studies have been conducted on one-way, two-way and multiple SMPs [78]. The first kind, one-way, can be traced in conventional crosslinked polymers [79]. Due to this, one-way SMPs have been utilized in general applications for a long time. Therefore, making it one of the most common smart materials. Applications are mostly affiliated with heat-shrinkable objects, such as heat-shrinkable tubes or labels. Examples of more high-tech devices include self-deployable hinges or biomedical devices, such as smart surgery devices [75]. Some of these applications among others can be found in Figure 2.9. Two-way SMPs are also known as reversible SMPs. This term refers to polymers which can deform at high temperatures and return between two shapes at low temperatures. The principle behind the two-way shape memory effect depends on the directional placement of the molecular chain when a temperature change is present. The last of the three SMPs, multiple SMPs, are polymers which are able to memorize more than one temporary shape. The multiple-shape memory phenomenon enables the polymer to switch between different shapes by programming [80]. SMPs allow for more deformation compared to SMAs, lower costs, tunable stiffness and ease of fabrication. The progress made in the creation and development of two-way SMPs with adequate mechanical properties and shape memory properties can lead to the replacement of SMAs by SMPs in the future.

The molecular architecture of SMPs consists of netpoints and domains. In Figure 2.10 several aspects such as entanglement and cross-linking can be seen. When the SME takes place, the memorization of the former/original appearance is related to the netpoints which are the reason for the permanent shape. In contrast, the reversible shape change is related to the switching of the domains. The flexibility of the chains of the polymer is dependent on the transition temperature (T_{trans}). For amorphous polymers, this equals the glass temperature (Tg) or (T_m) for semi-crystalline polymers. So by heating SMPs to a temperature higher than the T_{trans} the polymer chains will have high flexibility and can be deformed. This process is explained in the figure mentioned before [73].

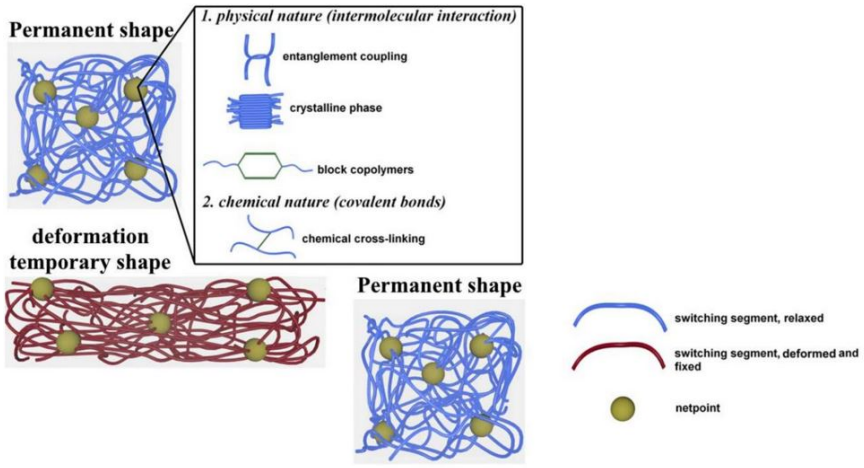

Figure 2.10: Schematics of the molecular mechanism for activation of shape memory in SMPs given in [74].

Additionally, another aspect of printing SMPs worth mentioning is the rise of 4D printing, which is an advanced additive manufacturing process [81]. It is the process of a 3D-printed object is capable of changing or modifying its structure due to external influences, such as light or temperature. Therefore making smart or stimuli-responsive materials one the most important components needed for 4D printing [82]. The big difference with standard 3D printing is that a new function is added to change shape over time visualised in Figure 2.11. Making the structure capable of self-healing. For instance, in the case of a damaged pipe, the structure possesses the ability to self-heal. A specific example would be, the 4D printing of Polyvinylchloride (PVC) with good shape memory effects [83]. Another example would be self-assembling. This could take place when small components are moved through tiny holes in the human body, the structure will be able to assemble later for medical purposes when needed [84–86]. Nevertheless, SMPs are associated with lower structural properties, such as their mechanical strength. Therefore, incorporating a second material or creating a composite is often beneficial for most applications [63].

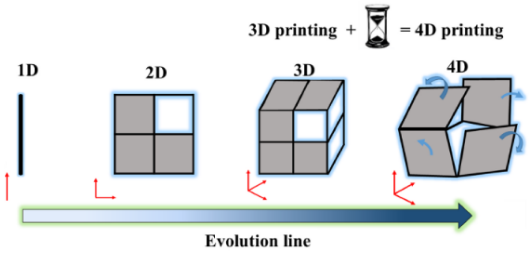

Figure 2.11: The concept of 4D printing [87].

(3) Shape Memory Ceramics (SMCs)

The last common group of SMMs are SMCs. They provide many advantages compared to metallic alloys, such as higher strength and higher operating temperatures [88]. SMCs are less likely to degrade due to creep and oxidation at higher temperatures than SMAs. Compared to SMAs a higher actuation stress and strain can be exhibited, with a bigger transformation temperature range. Shape memory behaviour is seen by a reversible martensitic phase transformation. Out of the current SMCs, ceramics based on zirconia (ZrO_2) have gained a lot of interest, due to the similarity to SMAs regarding thermo-mechanical capabilities [89]. Ceramics that are zirconia-based consist of the largest family of SMCs with shape memory behaviour and mechanisms similar to SMAs [90]. The brittleness of SMCs can still be improved since this would make the material more suitable for potential applications. Further research could also find a solution for the activation energy needed for SMCs, which is higher than for other SMMs [63].

2.2. Modelling Smart materials - FEA

Smart materials are meticulously modelled with advanced software tools suited for numerical simulations, facilitating the utilization of constitutive equation-based models [91]. Depending on the complexity of the model and various other considerations, such as the material's mechanical properties, these models are tailored to accurately describe nonlinear behaviours of smart materials [92, 93].

FEA is based on the Finite Element Method (FEM), which is unquestionably one of the most commonly used numerical tools for understanding physical systems with complicated boundary conditions [94, 95]. Therefore, FEA is an efficient approach to investigate the nonlinear behaviours of smart materials. Due to its broad application, the implementation of constitutive equations in FE software, such as COMSOL, ANSYS and ABAQUS has been gaining a lot of attention [84, 96]. ABAQUS has been chosen in this study since it integrates well with CAD software such as Solidworks, where most of the geometries will be created. Furthermore, if one works with complex structural mechanics, especially involving nonlinear material behaviour, contact mechanics, and dynamic analysis, ABAQUS is a good option [97]. In addition to this, ABAQUS provides advanced material models and user-defined material (UMAT) options, which are crucial for representing the unique constitutive behaviour of smart materials. The ABAQUS CAE (Complete Abaqus Environment) is used which enables one to quickly create, monitor and visualize advanced ABAQUS analyses. Modelling smart materials using FEA involves several steps [98, 99]:

For each material or structure, the geometry needs to be defined. The geometry is discretized into smaller elements by meshing. The material properties need to be specified and will depend on the type of smart material being modelled. For instance, for SMMs, phase transformations would be needed in combination with corresponding temperatures and mechanical properties.

To model industrial scenarios appropriate boundary conditions need to be applied. This consists of fixing nodes/surfaces, applying loads and adding thermal/electrical boundary conditions. A suitable solver must be chosen within the FEA algorithm since they can vary in speed and accuracy. Smart materials often have complex constitutive models that relate to various physical parameters. It is important that FEA algorithm supports the constitutive equations for integration and implementation [91].

The software/solver will solve the equations governing the material behaviour of the smart material based on the given material properties, boundary conditions and geometry. In addition, convergence of the solution is essential to establish stability and acceptability. Furthermore, data visualization through plots and quantitative data extraction are imperative for analysis. Subsequently, comparison with experimental data will validate the results, prompting adjustments in parameters. Finally, conducting sensitivity analysis will explain the impact of material properties and other parameters on the desired behaviour within the model [100].

The accuracy of the FEA model depends on the fidelity of the material properties, the mesh quality, the chosen solver, and the adequacy of boundary conditions. The physics associated with the model needs to be included as accurately as possible to create a precise model. It is important to note that, besides FEA, other methods are available for modelling smart materials, such as phase-field modelling and multi-scale modelling. However, these methods are more suited for atomic or microscale investigations and are not viable for this research, which focuses on the macroscale [101, 102]. Since the outputs in this study are deformations observed at the macroscale, FEA remains the most appropriate method for accurately capturing the material behaviour and performance under the defined conditions.

2.3. Shape-Morphing structures

Shape morphing is essential for achieving adaptability and responsiveness in structures, enabling them to deform in response to external stimuli. This transformation allows for functionalities such as gripping, locomotion, and shape adaptation, making morphing structures highly valuable in applications requiring flexibility and compliance [103]. These systems integrate materials, geometry, and actuation mechanisms to achieve controlled deformations. Compared to rigid structures, they provide smooth, continuous motion without mechanical joints, reducing friction, wear, and maintenance while enabling lightweight, bio-inspired designs [104]. Unlike traditional rigid systems that rely on discrete movements, morphing structures naturally adapt to external conditions, improving energy efficiency and versatility [105].

Morphology plays a crucial role in the performance of these structures by defining their form, spatial arrangement, and deformation pathways. To achieve mechanically intelligent, self-actuating morphing structures, smart materials must be integrated to respond to external stimuli such as temperature, light, or mechanical forces. This integration enables autonomous reconfiguration, eliminating the need for external actuation. By leveraging both geometric and microstructural properties, morphology dictates reversible shape transformations, bridging the gap between form and function. It combines material science, geometry, and engineering principles to create adaptable systems [106, 107].

Shape-morphing solar shading systems utilize SMAs, SMPs, and hybrids to dynamically adjust in response to solar radiation and temperature changes. This adaptation enhances energy efficiency by reducing reliance on artificial lighting and cooling systems while improving visual and thermal comfort for occupants. Inspired by natural plant movements, these systems optimize light penetration and heat control with minimal energy input, making them a sustainable and low-maintenance alternative to traditional mechanical shading devices [108, 109].

Shape morphing in aircraft wings enhances aerodynamic performance by dynamically adjusting their shape using smart materials like SMAs and SMPs. This allows modifications in wing span, chord length, camber, and twist, optimizing lift, fuel efficiency, and manoeuvrability without relying on traditional hinged control surfaces. SMA-actuated flexural structures reduce weight while supporting aerodynamic loads, enabling efficient, adaptive flight. By integrating shape morphing, aircraft achieve lower drag, improved fuel efficiency, and greater flight adaptability to varying conditions [13, 110].

Shape morphing in robotic grippers enhances adaptability by dynamically adjusting stiffness using flexure hinges with morphable flaps. This approach, inspired by origami folding, integrates pneumatically actuated pouches to control the stiffness of flexible robotic fingers, enabling secure grasps of objects with varying shapes and rigidity. The variable stiffness design allows efficient grasping without complex control systems, making it ideal for applications in industrial automation and teleoperation [59, 111].

Ongoing research continues to refine multi-scale designs and hybrid materials, enhancing the adaptability, efficiency, and scalability of morphing systems. By integrating SMAs and SMPs these systems are evolving to function effectively across various applications, including solar shading facades, bio-inspired robotics, aerospace structures, medical devices, and soft robotic grippers. Their ability to operate in dynamic and unstructured environments makes them increasingly valuable across multiple industries.

2.4. Conclusion

This chapter has established the foundation for understanding and modelling shape-morphing structures using smart materials by addressing the following subquestion: **“What types of smart materials are appropriate to use for a shape-morphing actuator”** By focusing on hydrogels, SMPs, and SMAs, the discussion explored their unique properties, deformation behaviours, and applications in fields such as soft robotics and adaptive systems. FEA was highlighted as the primary tool for modelling and predicting deformation behaviour, particularly in relation to bending deformation, which serves as the primary focus of this research. In addition, this chapter provided deeper insight into the concept of shape-morphing, exploring how this concept works and what applications it has been used to. Building on this foundation, the next chapter focuses on hydrogels as the first smart material studied. It explores their stimuli-responsive properties and deformation behaviour, using modelling to investigate different configurations and their potential for shape-morphing applications.

3

Design strategy

This chapter outlines a design strategy for morphing structures, examining different smart material approaches and their potential for shape adaptation. Various performance indicators are considered to assess effectiveness in applications like robotic gripping. The following sections define the framework and evaluation criteria, providing a foundation for simulations and validation.

3.1. Design strategy

The development of morphing structures is guided by a structured design strategy that leverages smart materials with dynamic shape transformation capabilities. A key requirement in designing these structures is the ability to achieve stiffness variation and adaptive morphing, enabling controlled deformation across different functional applications. Figure 3.1 illustrates this framework, highlighting the pathways involved in achieving tailored morphing behaviours. At the core of the diagram, morphing structures serve as the foundation, branching into two primary approaches: single smart material morphing structures and multiple smart material morphing structures. These pathways represent different strategies for enabling shape adaptation based on material selection and their inherent mechanical properties.

Smart materials exhibit tunable properties in response to external stimuli, allowing for controlled shape transformation. The first approach explores the use of a single smart material, such as hydrogel, which morphs through swelling and deswelling mechanisms. The figure depicts this pathway, where hydrogels undergo reversible deformations, making them suitable for applications requiring soft, compliant, and stimulus-responsive materials.

The second approach integrates multiple smart materials, specifically SMAs and SMPs, to enhance morphing efficiency. By combining these materials, the design benefits from SMA's thermally activated phase transformations and SMP's viscoelastic properties, which allow for tunable stiffness and controlled shape retention. This pathway is depicted in the figure, where the multi-material structure is reinforced through an advanced mechanical system.

A notable aspect of this framework is the feedback mechanism, represented by dashed arrows, which suggests iterative refinement and material selection processes. This indicates that morphing structures are not fixed but rather optimized through performance evaluation and adaptive modifications. The figure underscores how stiffness modulation bridges the gap between the flexibility of soft materials like hydrogels and the structural rigidity provided by SMA-SMP hybrids, allowing for tailored morphing responses across various applications.

By presenting a structured selection and integration process for smart materials, this design strategy ensures that morphing structures are effectively tailored for specific functional requirements. This strategy provides a structured approach to selecting and integrating smart materials into morphing structures. The following chapters explore hydrogel-based simulations and SMA-SMP hybrid modelling in greater detail, demonstrating their effectiveness in morphing applications. The applications found in Figure 3.1 will be further elaborated on in the next chapters.

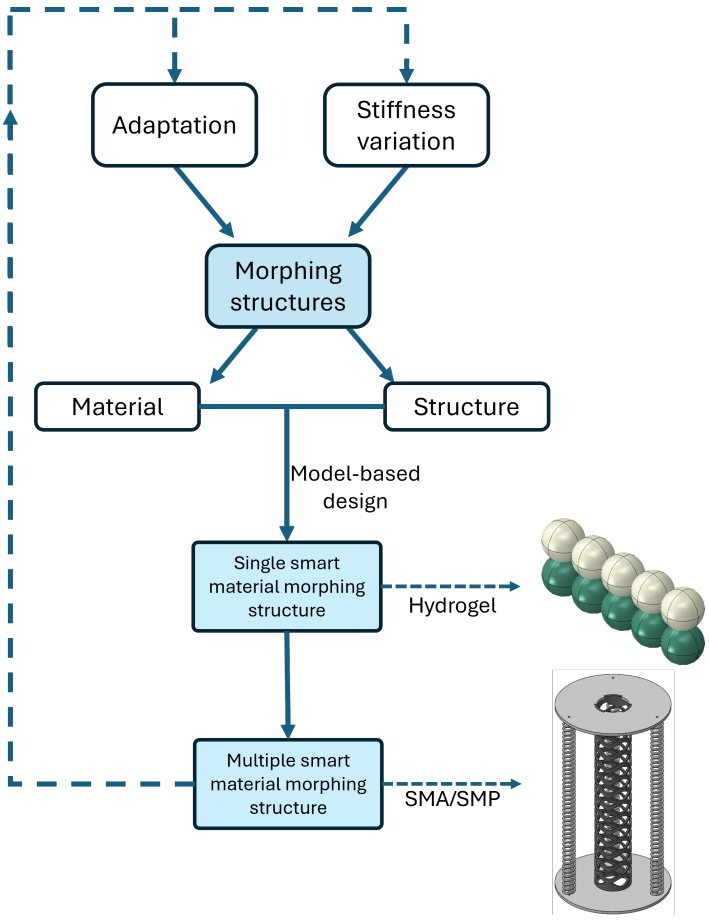

Figure 3.1: Overview of the design strategy for morphing structures.

3.2. Key Performance Indicator (KPI)

To systematically assess the effectiveness of these morphing structures, it is essential to define a KPI that captures their functional capabilities. In soft robotics, various deformation modes such as linear extension, bending, torsion, and spiral twisting, as illustrated in Figure 3.2, serve different functional purposes within actuating systems. These deformation modes allow soft robots to achieve a wide range of motions, from simple elongation to complex helical deformation. Linear extension is particularly effective for elongation or contraction tasks, torsion enables twisting actions and spiral twisting facilitates helical deformations. However, for many soft robotics applications, bending is selected as the primary KPI due to its relevance in tasks requiring flexible yet controlled motion.

Bending, as a mode of deformation, is pivotal in scenarios such as gripping, conformal contact with surfaces, and flexible arm structures. These tasks require a precise degree of curvature and adaptability, which bending excels at providing. The bending angle, as a measurable parameter, is critical in linking material properties, geometric morphology, and functional performance. It provides a direct and quantifiable measure of the actuator's deformation capacity and enables comparison across different designs and materials.

By focusing on the bending angle as the KPI, this research aims to establish a comprehensive framework for evaluating the performance of soft actuators. This will not only facilitate the development of advanced shape-morphing systems but also support their integration into practical, real-world robotics applications. The bending angle will be the key metric to assess how effectively these designs are.

Table 3.1: The KPIs defined in this study.

Symbol	Name
ϕ	Bending angle (hydrogel)
θ	Bending angle (SMP)

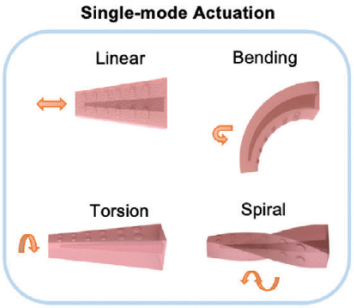

Figure 3.2: The fundamental deformation modes: linear, bending, torsion, and spiral [112].

3.3. Conclusion

This chapter answered the following question: **'How can a model-based design framework be implemented to model and predict the behaviour of structures with integrating smart materials?"**. The chapter outlined a structured design strategy for morphing structures, comparing single-material and multi-material approaches. Bending was identified as the KPI for evaluating shape adaptability. These insights provide the foundation for the following chapters, which focus on simulation, validation, and practical applications.

4

Smart material actuated shape-morphing structures: Smart hydrogel

This chapter explores the potential of smart materials in designing morphing structures, with hydrogel serving as a case study to examine its suitability as a morphing medium. The process of simulating hydrogels in combination with silicone using ABAQUS is explained, with a focus on the constitutive equations governing hydrogel behaviour. Various configurations, ranging from ball-to-ball interactions to complex geometries such as surfaces and shells, are introduced to demonstrate their deformation and morphing capabilities. Finally, a detailed discussion of the simulation results and the insights they reveal is provided. It is worth noting that sections of this chapter are published in [113].

4.1. Hydrogel in morphing structures

Hydrogels are highly suitable for shape-morphing applications due to their remarkable responsiveness to environmental stimuli and their ability to undergo substantial volumetric changes. Their unique properties, such as softness, adaptability, and biocompatibility, make them ideal for creating dynamic, shape-morphing systems in applications ranging from robotics to soft actuators. In this section, the role of hydrogels in enabling shape-morphing behaviours is explored, with a focus on their suitability for responsive and adaptive designs. Hydrogels stand out as a key material for innovative morphing systems, offering smooth and controlled deformation with minimal energy requirements.

Thermal Responsiveness in Shape Morphing

Thermally responsive hydrogels, such as PNIPAM, are particularly effective in shape-morphing systems due to their reversible swelling and deswelling behaviour. When exposed to temperature changes, hydrogels dynamically adjust their volume, enabling precise shape transformations. Below their LCST, hydrogels swell, increasing their size and creating expansive forces. Above the LCST, they contract, expelling water and returning to their original state. This thermal responsiveness makes hydrogels an excellent candidate for applications requiring reversible deformation, such as actuators, adaptive surfaces, and soft robotics.

Hybrid Systems for Controlled Deformation

Hydrogels are often integrated with structural materials like silicone to create hybrid systems that enhance their functionality. In these systems, hydrogels provide the driving force for deformation, while the structural material ensures stability and guides the morphing behaviour. For instance, in a bending or curling actuator, the hydrogel's expansion drives the motion, while the silicone framework constrains the deformation to achieve predictable and repeatable shapes. This synergy allows for the creation of multi-directional and complex morphing behaviours, which are critical in adaptive systems.

Applications in Shape Morphing
Hydrogels excel in applications requiring significant, smooth deformation, particularly in environments where softness and biocompatibility are essential. Their ability to produce controlled, adaptive shape changes makes them suitable for soft robotic grippers. Furthermore, hydrogels' capability to synchronise with external stimuli, such as temperature, allows for precise control of morphing behaviours. This adaptability makes hydrogels a critical material for advancing technologies in robotics.

Constitutive equations Hydrogel

A generalized theory has been created to specify different kinds of hydrogel, even if the hydrogels differ by their stimulus. This section gives the constitutive equations for neutral Gel and more specifically temperature-sensitive Gel. The latter model is an adaptation of the former model by including terms for temperature. The constitutive equations of hydrogel make use of the Neo-Hookean hyperelastic material model [114, 115], whose strain-energy function is given in Equation 4.1 where T is the absolute temperature, k_B is the Boltzmann constant, N is the crosslink density, λ is the principles stretch in each direction and W is the strain-energy. This equation is chosen since hydrogels are a hyperelastic material type.

$$W = \frac{1}{2} N k_B T (\lambda_1 + \lambda_2 + \lambda_3 - 3) \tag{4.1}$$

Neutral Gel

The most frequently studied type of gel, is the neutral gel. The neutral gel has one single stimulus which is external exposure to water. Since there are no other stimuli, the constitutive model is fundamental. By combining the Flory–Rehner free-energy function due to stretching a network of polymers with the three principal normal stresses [116], the general form can then be expressed as follows in Equation 4.2,

$$\frac{s_{iK}}{k_B T / v} = N v \left(F_{iK} - H_{iK}\right) + \left[J \log\left(1 - \frac{1}{J}\right) + 1 + \frac{\chi}{J} - \frac{\mu_p}{kT} J \right] H_{iK} \tag{4.2}$$

Equation 4.2 connects the stress component to the deformation gradient in the case of the gel being held at a not-varying chemical potential by a reservoir of solvent molecules. With s_{iK} being one of the three nominal stresses, v is the specific volume, F_{iK} is the deformation gradient with i=1,2,3, μ_p is the chemical potential, J is the volumetric strain, and χ is the dimensionless measure of the enthalpy of mixing [117].

Temperature-sensitive Gel

Temperature-sensitive hydrogels, also known chemically as PNIPAM hydrogels, are hydrogels that can withstand large changes in volume due to temperature changes [55, 60]. Because of their distinctive characteristic of exhibiting a sharp macromolecular transition from hydrophilic to hydrophobic, temperature-sensitive hydrogels constitute a significant branch within the realm of hydrogels. In addition to this, these types of hydrogels are transparent, elastic and flexible. The constitutive equation is similar to the one of neutral gel, the only addition is the interaction parameter χ with χ_0, χ_1 and ϕ (Equation 4.3) being dependent on experimental data obtained for PNIPAM [118].

$$\chi = \chi_0 + \chi_1 \cdot \phi \tag{4.3}$$

By combining Equation 4.2 of the neutral gel with Equation 4.3 and the uniaxial load case the following system of equations seen in 4.4 can be obtained. With s being the stress, V is the volume of the gel and V_0 is the volume of the referential state.

$$A\nu\left(\lambda_1^2-1\right)+\left(\frac{V}{V_0}\right)\log\left[1-\left(\frac{V}{V_0}\right)^{-1}\right]+1+(\chi_0-\chi_1)\left(\frac{V}{V_0}\right)^{-1}+2\chi_1\left(\frac{V}{V_0}\right)^{-2}=0,$$
$$\frac{1}{\lambda_3}\left[N\nu\left(\lambda_3^2-1\right)+\left(\frac{V}{V_0}\right)\log\left[1-\left(\frac{V}{V_0}\right)^{-1}\right]\right]+\frac{1}{\lambda_3}\left[1+(\chi_0-\chi_1)\left(\frac{V}{V_0}\right)^{-1}+2\chi_1\left(\frac{V}{V_0}\right)^{-2}\right]=\frac{s\nu}{k_BT} \tag{4.4}$$

4.1.1. Silicone

As mentioned before, hydrogels need sufficient strength to grip objects securely when applied in soft robotics. Therefore a second material is needed to add some strength to the hydrogel and keep the material together. The material chosen for this is silicone, or more precisely Ecoflex 00-10. In the field of soft robotics, components are often constructed from hyperelastic materials such as silicone rubber, due to its Young's modulus typically ranging from 10^4 to 10^9 Pa [119].

Silicone is mechanically robust and elastic, providing structural support to hydrogel components. Despite being extremely soft, Ecoflex 00-10 provides a decent mix of stretch and tear resistance, allowing it to flex without easily tearing. Furthermore, the material is known for its durability, it can be used repeatedly while maintaining its properties [120]. Common applications can be found in prosthetics, due to their lifelike texture. Its skin-like properties also make it suitable for medical simulation models. Lastly, in the field of soft robotics, it is often used to create soft and flexible parts, aiming for more natural movements [121].

Constitutive equations Silicone

Silicone materials like Ecoflex 00-10 are often modelled as hyperelastic materials in FEA. Hyperelastic materials describe large deformations under load, and their behaviour is as mentioned before typically characterized by a strain energy density function, W. The Neo–Hookean model is used as the constitutive model to characterize the mechanical properties of the silicone with μ_N being the Neo-Hookean parameter and λ the stretch.

$$W=\mu_N(\lambda^2+\frac{2}{\lambda}-3) \tag{4.5}$$

Based on [122] the derivation can be made for μ_N. By taking into account the isotropic, nonlinear, and incompressible characteristics as described in Equation 4.5, the Engineering Stress-Stretch (σ_E - λ) relationship for the Neo-Hookean model can be expressed as:

$$\sigma_E=2C_1(\lambda-\frac{1}{\lambda^2}) \tag{4.6}$$

To compute the material constant (C_1) for the Neo-Hookean model, the Engineering Stress-Stretch (σ_E - λ) relationship from Equation 4.6 was rearranged, yielding the final expression shown in Equation 4.7.

$$C_1=\frac{\sigma_E}{2(\lambda-\frac{1}{\lambda^2})} \tag{4.7}$$

Finally, μ_N can then be found by using Equation 4.8.

$$C_1=\frac{\mu_N}{2} \tag{4.8}$$

4.2. Ball to ball

This section investigates ball-to-ball simulations of hydrogel and silicone to explore the effects of hydrogel expansion, using spherical geometries inspired by the droplet models in Downs et al. [123]. These models focus on the deformations caused by hydrogel swelling, where spheres serve as simple yet effective geometries. While hydrogel alone primarily leads to isotropic size increases, the inclusion of silicone introduces a second material that enables diverse and controlled deformation patterns. By analyzing the interactions and mechanical behaviours of these balls, the simulations provide insights into the fundamental dynamics of hydrogel-silicone composites.

4.2.1. Simulation setup

As previously noted, ABAQUS will be employed to simulate the hydrogel balls. This multi-physics modelling and simulation software will be utilized for finite element analysis of the hydrogel balls [97]. The simulation process will be conducted in multiple stages. Initially, the material properties and geometry will be defined. Subsequently, multiple assemblies comprising the balls to be modelled will be constructed. Following this, environmental dynamics relevant to the model will be incorporated, and finally, appropriate boundary conditions will be applied to complete the setup.

Material

ABAQUS will be used to determine the deformation and expansion of various hydrogel configurations. Since the properties of hydrogel are not inherently available in ABAQUS, a user-defined hyperelastic material subroutine is required to perform the simulations [124]. The equations outlined in section 4.1 are implemented within this subroutine, which is provided in the Appendix (section B.2). Due to the nonlinear nature of hydrogel, hyperelastic inputs are essential in the material library. These inputs include:

- Initial swelling ratio (λ_0 = 1.5),
- Equilibrium chemical potential (μ = -0.0343), and
- Dimensionless parameter (Nv = 0.01), representing the crosslink density.

The specific hydrogel type simulated in this study is PNIPAM. Additionally, a secondary material, silicone (Ecoflex 00-10), with rubber-like properties, is incorporated as the structural framework for the hydrogel balls [125]. Due to the nonlinear nature of silicone, hyperelastic inputs are also essential in the material library. The input used in Abaqus can be found by using Equation 4.8:

- The Neo-Hookean parameter (μ_N = 0.224) [126]

Geometry

The mentioned materials will be assigned to a spherical solid geometry with a diameter of 20 mm each. To ensure that these balls remain fixed together, a slight overlap of 1 mm is introduced at every contact between balls. A schematic front view of multiple balls, showing the overlap, is provided in Figure 4.1. In this figure, green balls represent silicone, while light grey balls represent hydrogel. This colour distinction will be applied across other configurations as well. An isometric view of a merged geometry in ABAQUS is shown in Figure 4.2.

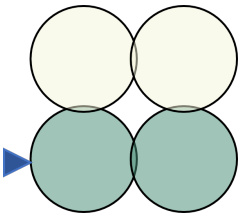

Figure 4.1: Initial configuration of the combined hydrogel and silicone part.

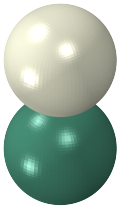

Figure 4.2: The isometric view of a merged configuration in ABAQUS.

Mesh

To discretize the geometry, the balls were meshed for the simulation using the C3D8H element type [127], chosen for its use of a hexagonal mesh and hybrid formulation, which is essential for hydrogels due to their incompressible behaviour [128]. A mesh sensitivity analysis is a critical step in FEM to ensure accurate and reliable simulation results. In this study, the bending angle was selected as the primary variable to evaluate the impact of mesh size on model performance. The default mesh size in Abaqus, set at 1 mm, served as a baseline, with additional analyses conducted for mesh sizes ranging from 2.5 mm (coarse) to 0.4 mm (fine). The number of elements in these analyses spanned approximately from 900 to $4.25 \cdot 10^5$, as detailed in Table 4.1, and the corresponding plot is shown in Figure C.1. Finer mesh sizes are expected to improve accuracy by capturing intricate deformations but come with a significant increase in computational cost. A convergence study was conducted to identify an optimal balance between computational efficiency and accuracy. This study systematically refined the mesh and monitored changes in the bending angle to determine the point at which further refinement led to negligible variations, indicating sufficient mesh resolution. As illustrated in Figure 4.3, convergence was achieved when the curve flattened or approached an asymptote.

Table 4.1: Mesh sizes with a corresponding number of elements and bending angles for hydrogel-silicone model mesh sensitivity analysis.

Mesh size [mm]	Number of elements [-]	ϕ [deg]
0.4	$4.25 \cdot 10^5$	64.65
0.45	$2.82 \cdot 10^5$	64.61
0.5	$2.08 \cdot 10^5$	64.53
0.55	$1.64 \cdot 10^5$	64.48
0.6	$1.10 \cdot 10^5$	64.40
0.75	$5.74 \cdot 10^4$	64.19
1	$2.73 \cdot 10^4$	64.03
1.25	$1.10 \cdot 10^4$	63.75
1.5	$3.70 \cdot 10^3$	63.41
2.5	$9.28 \cdot 10^2$	63.25

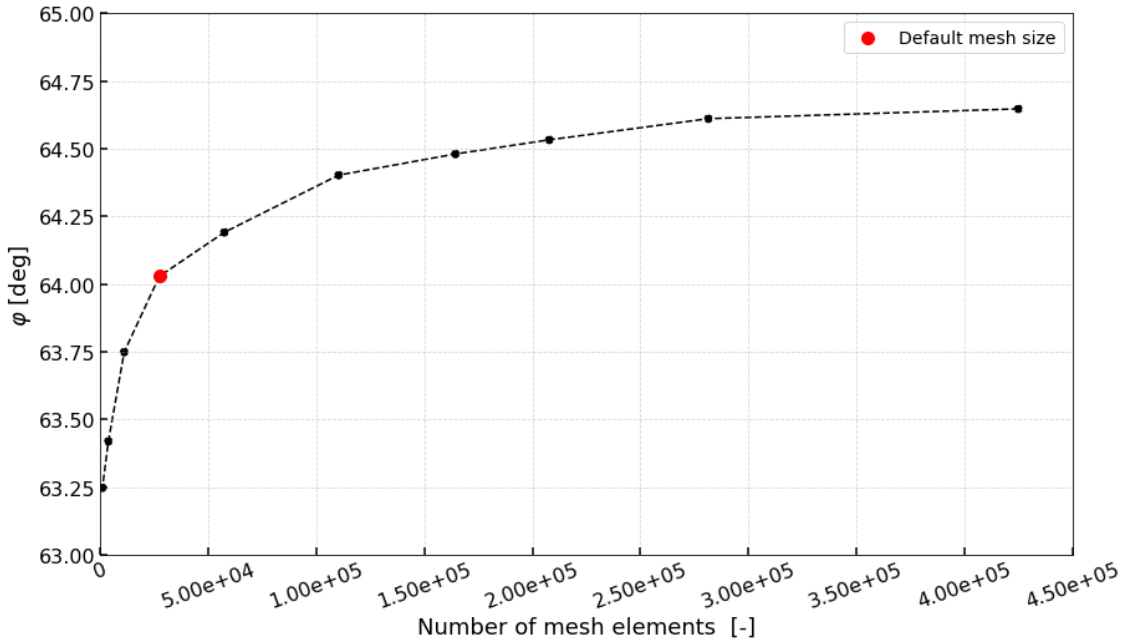

Figure 4.3: The bending angle plotted against the number of mesh elements for Hydrogel-silicone models.

Quantitative convergence was assessed using a threshold, defined as a percentage change in the

bending angle between successive refinements. A predefined threshold of 1 % was applied to determine convergence. The convergence study was performed using Equation 4.9, where ϕ_n represents the refined result and ϕ_{n-1} the previous angle. The analysis results are depicted in Figure C.2 in section C.1.

$$\Delta_{c,h} = \left| \frac{\phi_n - \phi_{n-1}}{\phi_{n-1}} \right| \times 100 \tag{4.9}$$

While finer meshes enhance accuracy, they significantly increase computational time, necessitating a balance between precision and efficiency. The hydrogel was found to exhibit stable behaviour, converging relatively quickly and showing minimal changes in bending angle with further refinement. However, in this section the relative bending angle compared to the most accurate result will be discussed. For this Equation 4.10 was used with ϕ_N being the most accurate bending angle, corresponding with the largest number of mesh elements.

$$\Delta_{f,h} = \left| \frac{\phi_N - \phi_n}{\phi_n} \right| \times 100 \tag{4.10}$$

This resulted in the difference in bending angle relative to the bending angle with the largest number of mesh elements to be plotted in Figure 4.4. From these results, it is evident that the bending angle deviated by less than 0.5% when the number of mesh elements exceeded $1.64 \cdot 10^3$, which can be found in Table 4.2. Therefore, a corresponding mesh size of 0.55 mm was selected as an optimal balance between accuracy and computational efficiency.

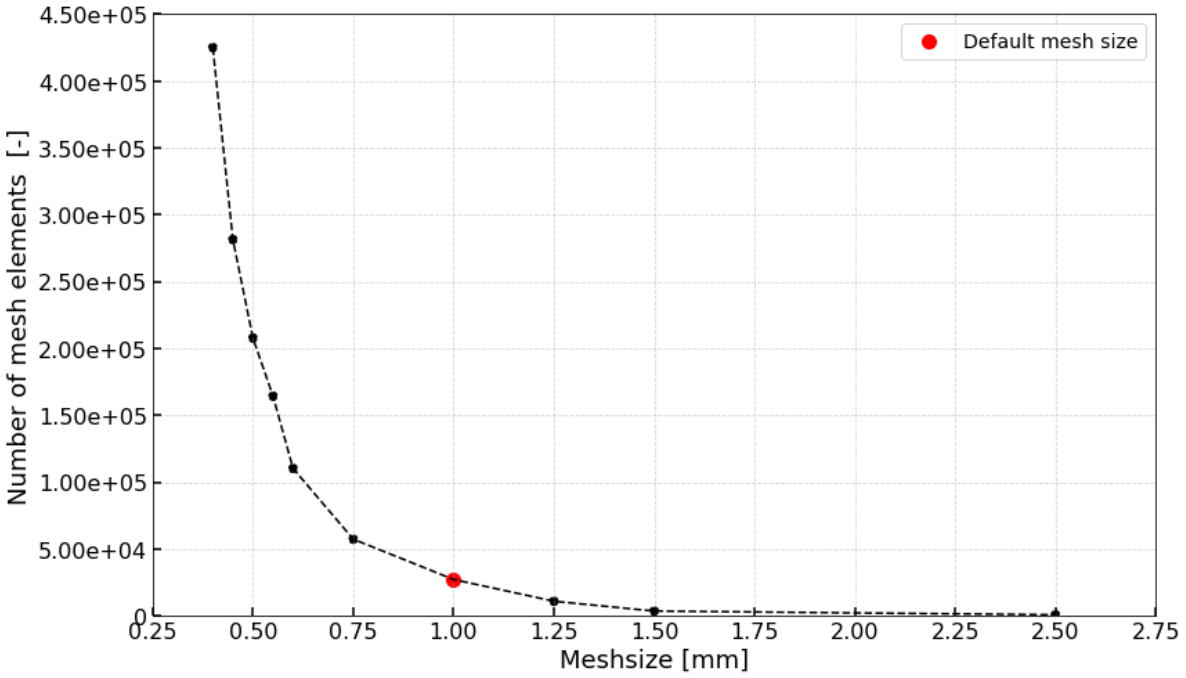

Figure 4.4: Plot showing the percentage difference in bending angle, relative to the final (most accurate) mesh configuration, for varying mesh element counts for Hydrogel-silicone models.

Table 4.2: Percentage difference in bending angle for various mesh element counts, calculated relative to the final (most accurate) mesh configuration of the hydrogel-silicone model. The chosen number of elements is indicated in bold.

Number of elements [-]	$\Delta_{f,h}$ in $\%$
$4.25 \cdot 10^5$	0.00
$2.82 \cdot 10^5$	0.0561
$2.08 \cdot 10^5$	0.177
$1.64 \cdot 10^5$	0.258
$1.10 \cdot 10^5$	0.378
$5.74 \cdot 10^4$	0.705
$2.73 \cdot 10^4$	0.956
$1.10 \cdot 10^4$	1.39
$3.70 \cdot 10^3$	1.90
$9.28 \cdot 10^2$	2.16

Timesteps

The simulation employs timesteps to accurately model the expansion of the balls. A static general analysis approach is used, with each timestep divided into increments ranging from 10 to 30, depending on the complexity of the simulation. For each timestep, a predefined field is assigned with a specific temperature value. This results in five additional steps, each corresponding to a distinct temperature level. Each step is set to last for 1 second, leading to a total simulation time of 5 seconds. A full Newton solver technique is implemented, employing a direct solver approach rather than an iterative one.

Boundary conditions

Since the objective of this study is to observe the movement of hydrogel balls resulting from expansion, external forces such as gravity and friction were considered irrelevant and were therefore excluded from the model. To ensure controlled deformation, a single boundary condition was applied: a fixed constraint on the leftmost silicone ball in nearly all configurations. This constraint prevented any translations in the x, y, and z directions ($U_x = U_y = U_z = 0$) as well as any rotations around the x, y, and z axes ($R_x = R_y = R_z = 0$).

The purpose of this constraint was to prevent the entire assembly from floating freely within the simulation domain due to hydrogel expansion. Without it, tracking the motion and deformation of the balls would be difficult, as the entire structure would drift uncontrollably. By fixing a single silicone ball, the simulation could accurately capture the relative movement and expansion effects within the system. The application of this constraint is schematically represented in Figure 4.1 with a blue triangle and is consistently applied across all configurations discussed in this section.

In this study, the balls are subjected to cooling, requiring the creation of multiple fields with progressively lower temperatures. The initial temperature is set at 300 K and decreases in increments of 5 K until a final temperature of 275 K is reached.

Table 4.3: Parameters used in the simulation setup for the ball to ball setups of hydrogel.

Parameters	**Value/type**	**Unit**
Material 1	PNIPAM	-
Material 2	Ecoflex 00-10	-
Ball diameter	20	mm
Overlap distance	1	mm
Initial temperature	300	K
Final temperature	275	K
Temperature step	5	K
Duration step	1	s

4.2.2. Configurations

This section examines hydrogel and silicone models across multiple configurations, progressively increasing in complexity. Starting with simple arrangements, the models evolve to incorporate intricate designs, analyzing interactions and mechanical behaviours. This approach highlights the impact of configuration complexity on performance, offering insights into bending, gripping, and the potential applications of hydrogel-silicone composites in soft robotics.

Reference case-C1

The configuration uses balls which are 40 times bigger in diameter than the one mentioned in the example of the paper [123], but the design setup is the same. The referenced configuration consisted of five balls of each material type in a row. Two of these rows were placed on top of each other, forming a configuration with ten balls. Each row had its specific polymer properties depending on the material being silicon or hydrogel. The purpose of this configuration was to obtain bending around the Z-axis. For further analysis, the number of balls used in the reference case was increased, these configurations were labelled under the first configuration (C1). Thus extending the configuration with a hydrogel ball and silicon ball. The reason for this was to obtain a larger curved area. The goal was to find out how many balls were needed to obtain a circle and how the elongation of the configuration would influence the bending between balls. The schematic 2D depiction of the configuration with the respective 'fix' constraint can be found in Figure 4.5a. In Figure 4.5b an example is given of 20 balls, with the red rectangle indicating a 'ball pair'.

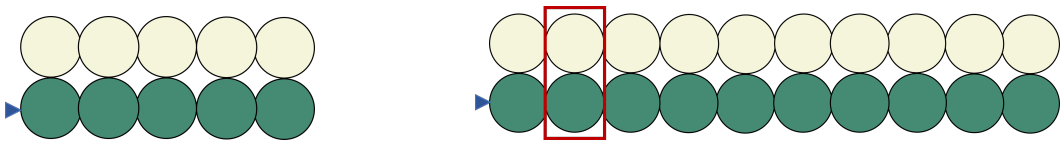

(a) The reference case **(b)** C1 with ten pairs

Figure 4.5: Overview of the different C1 configurations.

C2

The second configuration consisted of twice the initial configuration and a reversal of the material type in the middle. This could have resulted in alternations between the orientations. An example is given here, with 20 balls as shown in Figure 4.6a. With this, an 'S' shape could be obtained by bending in two directions for each of the five ball pairs. This would have been useful for an object with a varying width. In addition to this, two alternative options to this configuration were made, showcased in Figure 4.6.

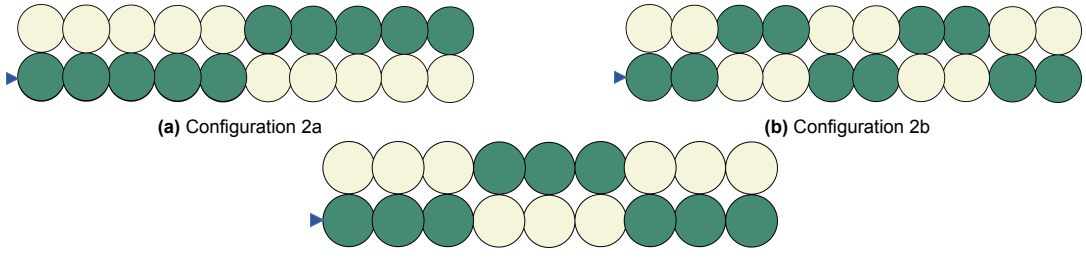

(a) Configuration 2a **(b)** Configuration 2b

(c) Configuration 2c

Figure 4.6: Schematic overviews of the different C2 structures.

C3

The first combined configuration was developed by extending Configuration 2 with multiple pairs from Configuration 1, as shown in Figure 4.7. This arrangement comprised a total of 32 balls, maintaining a 1:1 ratio of hydrogel to silicone. The objective of this combined configuration was to investigate whether a "hook" or "tentacle" structure could be achieved. This was approached by inducing bending in two opposite orientations, followed by a longer segment composed of identical ball pairs at the end. An isometric view of this configuration is presented in Figure 4.7.

C4

The final configuration was a combination of two perpendicular arrangements, as illustrated in Figure 4.8. This setup included 37 hydrogel balls and 37 silicone balls, providing sufficient material for the "fingers" to curl towards each other and enclose a spherical object. Additionally, a single ball was positioned at the centre to serve as a fixed constraint. This arrangement formed two intersecting crosses of 36 balls each, with a ball pair at the centre, resulting in a total of 74 balls. This configuration was the first to demonstrate potential functionality as a gripper. The central silicone ball, fixed in place (indicated in red), served as the anchor for the entire structure, enabling the "fingers" to curl inward toward the centre.

Figure 4.7: C3: 'The hook'

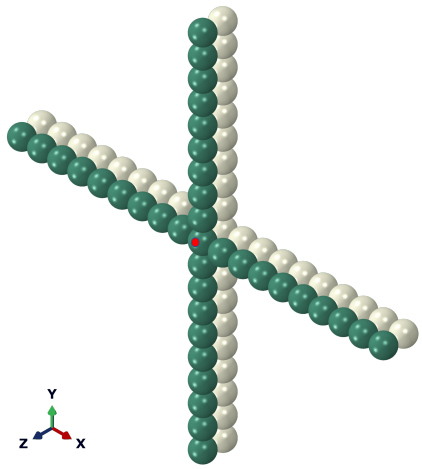

Figure 4.8: C4: 'The gripper'

A list with all the setups tried with the spherical geometries can be found in Table 4.4.

Table 4.4: Summary of all the configurations with the ball-to-ball combinations.

#	Type	Name
1	-	Single hydrogel ball
2	-	Hydrogel + silicone ball
3	C1	Reference case (10 balls)
4	C1	20 balls
5	C1	26 balls
6	C1	32 balls
7	C1	40 balls
8	C1	44 balls
9	C2	20 balls with alteration after 5
10	C2	20 balls with alteration after 2
11	C2	18 balls with alteration after 3
12	C3	Hook (32 balls)
13	C4	Gripper (74 balls)

4.3. Results shape-morphing hydrogel-silicone models

All the models mentioned in Table 4.4 have been simulated and the results will be discussed below. The output of the simulations will be evaluated by looking at bending angles, expansion and deformation.

Verification of the PNIPAM hydrogel

The first simulation yielded the expansion of one single hydrogel ball with a temperature decrease from 300 K to 275 K. The expansion given below in Table 4.5 is expressed in the diameter ratio and volume ratio.

Table 4.5: Expansion single hydrogel ball.

T [K]	**D** $[mm]$	D/D_0 [-]	V/V_0 [-]
300	20.00	1.00	1.00
295	22.84	1.14	1.50
290	24.44	1.22	1.82
285	25.65	1.28	2.11
280	26.62	1.33	2.36
275	27.45	1.37	2.59

To investigate the expansion rate a plot has been made with the diameter as a function of time as can be seen in Figure 4.9. Each red dot represents the final temperature reached at the end of a time step. In this plot, the data points show a decreasing expansion rate. The expansion slows down with each timestep as the temperature decreases. By looking at the function, a logarithmic curve can be observed.

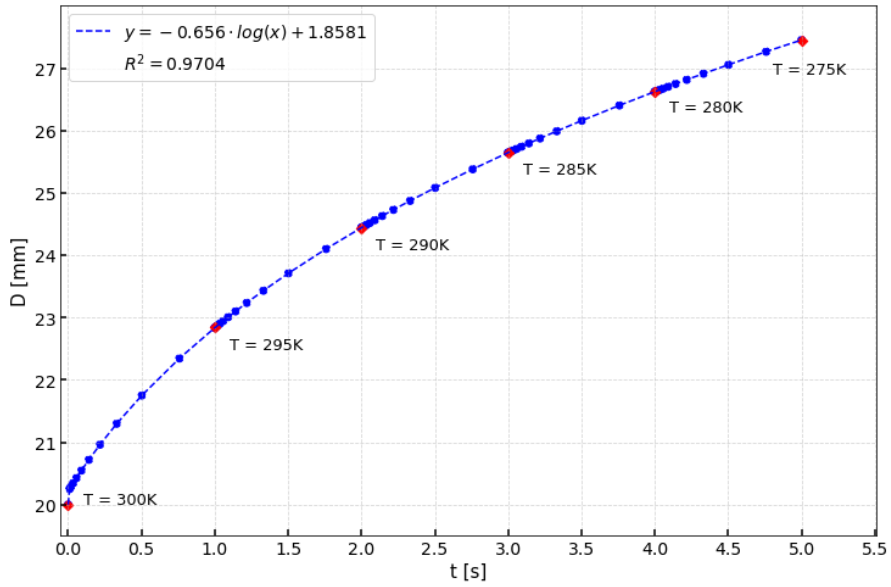

Figure 4.9: Expansion plotted against the time.

First configuration - reference case With lowering the temperature, bending can be observed along the five ball pairs. In Figure 4.10 the final state of the configuration can be found. The corresponding bending angle, ϕ between the outer pairs at the final step of each of the five temperatures has been obtained. This bending angle and the corresponding difference in angle, $\Delta\phi$, between each temperature can be found in Figure 4.6. It should be noted that the given bending angle depends on the configuration. The specific angle, ϕ*, can be determined with Equation 4.11. In this case, n is the number of ball pairs. This is a more accurate representation since the bending angle would be greater if the chain of ball pairs were extended. Furthermore, it is important to note that the proposed configuration has been verified by earlier research [59].

$$\phi^* = \frac{\phi}{n-1} \tag{4.11}$$

4.3.1. Effect of different design parameters

Here the results of the multipair simulations can be found. The simulation of the setup used had been performed with 20, 26, 32, 40 and 44 balls. It must be stated that by estimations, it was found that 44 is the minimum to reach a full circle with the given set-up. Therefore, the last simulation of 44 balls has

Table 4.6: Bending angles and differences reference case.

T [*K*]	ϕ [deg]	$\Delta\phi$ [deg]	ϕ***** [deg]	$\Delta\phi$***** [deg]
300	0	0	0	0
295	28.1	28.1	7.03	7.03
290	41.1	13.0	10.29	3.26
285	52.2	11.1	13.05	2.76
280	59.8	7.6	14.95	1.90
275	65.7	5.9	16.43	1.48

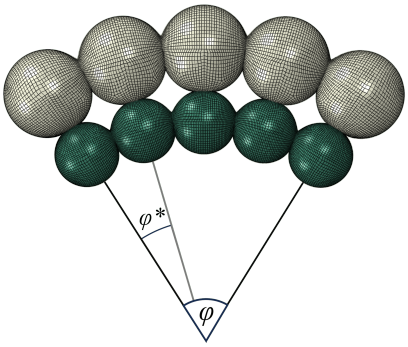

Figure 4.10: Reference case at T = 275 K

specifically been chosen. The deformation at the final temperature for various cases can be seen in Figure 4.11 respectively. As can be seen, the type of deformation is not influenced by the amount of balls. The same curling behaviour can be observed in both cases. The radius in each case between the centre of the curl and the balls does not differ.

(a) C1 structure with 20 balls

(b) C1 structure with 26 balls

(c) C1 structure with 32 balls

(d) C1 structure with 40 balls

Figure 4.11: Multipair configurations in the deformed state at T = 275 K.

Important to note is that the simulation did not account for interactions. For example, by looking at Figure 4.12, one could assume that a perfect circle had been formed with the 44 balls. However, by zooming in this is not the case. In the zoom-in of the figure, a clear connection between both ends can be found, with this connection having a bigger overlap than the neighbouring overlaps. Two circles (blue and red) with the same diameter have been placed at the connecting point to highlight the difference in overlap. Meaning that this is not a perfect circle and the balls were moving in one another due to

the lack of interaction constraints. In reality, the balls would push against one another. It is important to note that the number 44 is the minimum needed to obtain the circle, any amount lower than this will leave a considerable gap in between the balls.

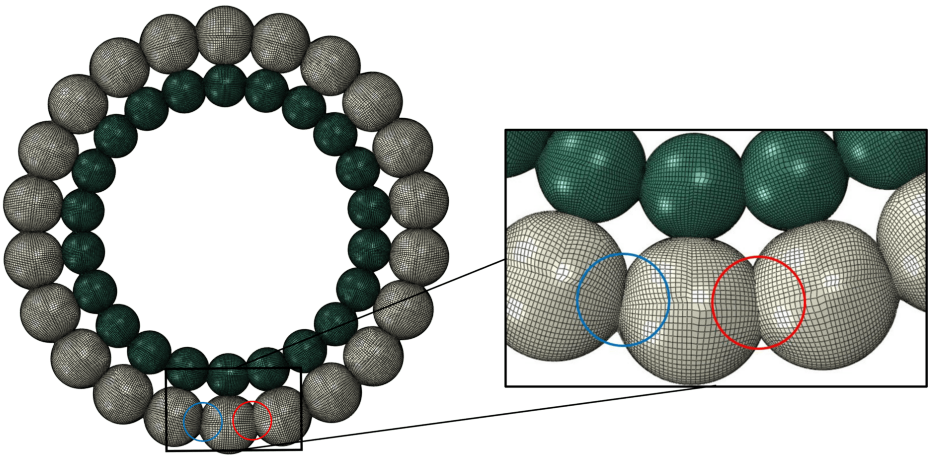

Figure 4.12: C1 with 44 balls in the deformed state at T = 275 K.

One aspect that continued to show is the influence of the boundary condition, in this case, the 'fix' constraint placed on the silicone ball. This fixed constraint functions as a hinge in every direction, which can be observed in Figure 4.17. The hinge point only influences the orientation but not the deformation. Secondly, it can be noticed that with larger configurations, out-of-the-plane rotations can also be observed. Almost all the longer configurations have been slightly rotated out of the X-Y plane. Most of the configurations were made in the X-Y plane and are deformed and bent in this plane. However, the longer configurations tended to rotate around the fixed silicone ball in the Z-direction. This can be seen in Figure 4.13 for the C1 with 32 balls. Rotation around the X-axis and Y-axis can be found. A vertical and horizontal axis have been drawn with dotted lines to indicate the angle made with the axis. Even though these rotations seem to be small, this could influence the determined bending angle, since this was done by looking at the X-Y plane. For the next step, the intention is to delve deeper into the interaction dynamics between silicone and hydrogels, aiming to enhance stabilizing the entirety of the structure.

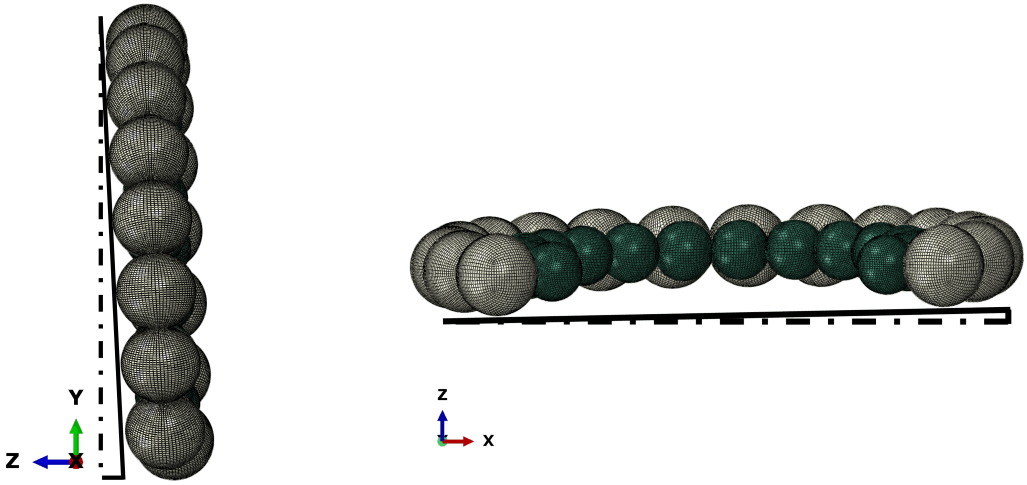

(a) Z-Y view **(b)** Z-X view

Figure 4.13: Out of plane rotations - 32 balls in the deformed state at T = 275 K.

The specific bending angles for the four configurations mentioned earlier and the reference case, consisting of ten balls, have been plotted in Figure 4.14. It can be seen that the bending angle is practically the same for all the configurations, regardless of the amount of balls. The bending behaviour seems to slow down over time, this is consistent with the expansion rate seen in Figure 4.9. This makes sense since the bending and expansion have a direct correlation. The bigger the expansion of the hydrogel balls, the greater the bending.

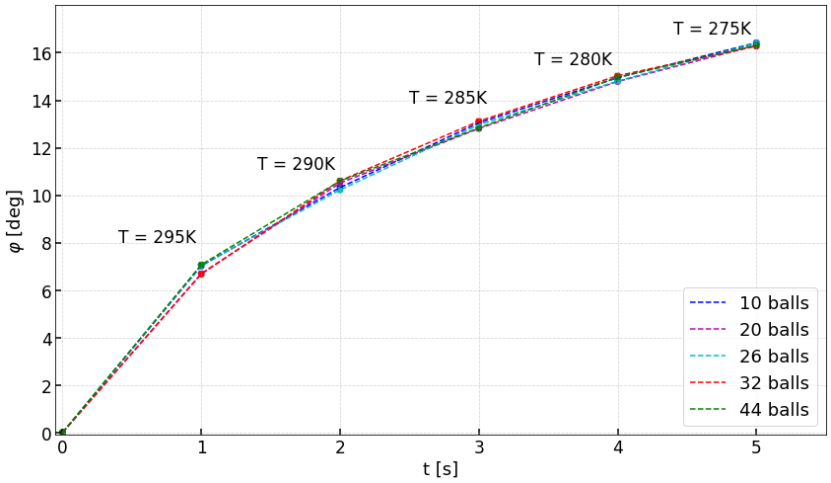

Figure 4.14: Bending angle plotted against the time.

To find the correlation between the expansion and bending, these two have been plotted against each other in Figure 4.15 with the specific bending angle on the vertical axis and the dimensionless diameter on the horizontal axis. The dimensionless diameter is the difference between the current and original diameter, D-D_0, divided by the original diameter, D_0. This gives a better impression of the expansion regardless of the original diameter of the ball. By adding a fitting curve for these five points, a seemingly linear relation can be found with the corresponding equation given in the legend of the graph. This is not surprising since the expansion has a direct impact on the bending angle. The R^2 value of 0.998 has been added to show the accuracy of the curve found, meaning that approximately 99.8% of the observed variation can be explained by the model's inputs.

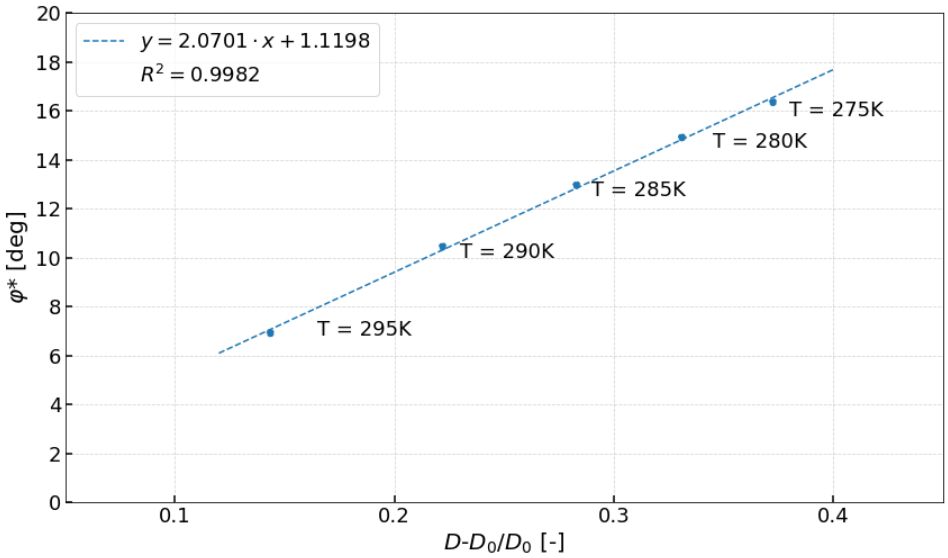

Figure 4.15: Specific bending angle plotted against the deformation.

C2 - Twists For the two different alterations, the bending behaviour observed in the C1 cases in a single direction is also present here. However, the bending direction varies depending on the material configuration, as illustrated in Figure 4.16a and Figure 4.16b. One important thing to note is that even though the material was slightly stretched the connection with the neighbouring balls stayed intact. This means that curvature in multiple directions was possible without destroying the bonds after an alteration. Furthermore, it can be observed that more bending was obtained by having more balls in the same material orientation. For example, in Figure 4.16b the 'amplitude' is much smaller than in Figure 4.16a even though both simulations made use of the same amount of balls.

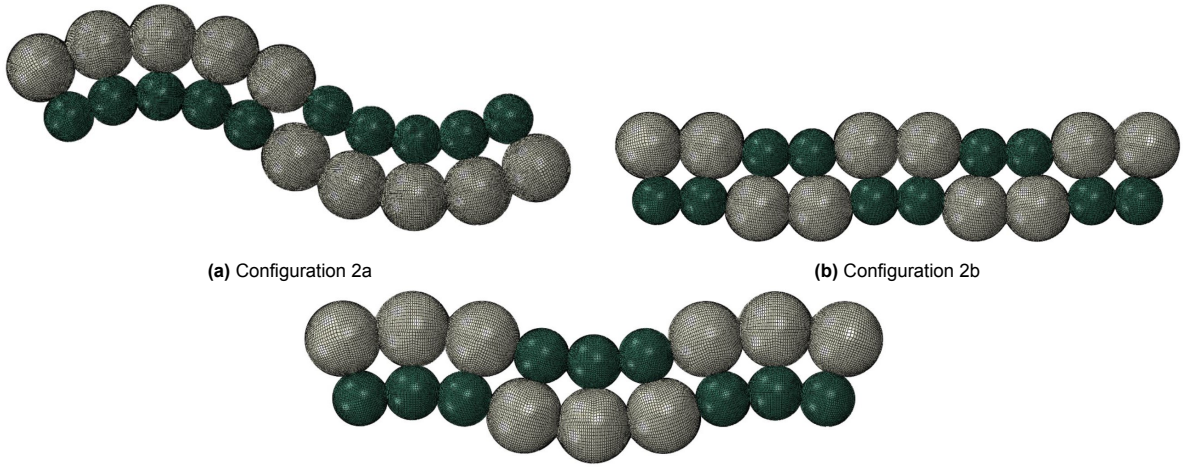

(a) Configuration 2a

(b) Configuration 2b

(c) Configuration 2c

Figure 4.16: Configurations with alterations in the deformed state at T = 275 K.

C3 - Hook For this configuration, a hook shaped configuration was the outcome, this was the first combined configuration with a different number of balls in each sub-configuration. Figure 4.17 shows how the entire structure hinged during the expansion of the hydrogel balls in the simulation, with stage 4 being the final form. The hinge point is again the fixed silicone ball on the left corner. The entire structure rotated approximately 240 degrees, which was probably due to the energy involved with the expansion but cannot be explained at this point in time based on the simulations performed within this research scope. However, this is the first configuration with an asymmetric bending pattern this might be the cause for the rotation around the hinge point.

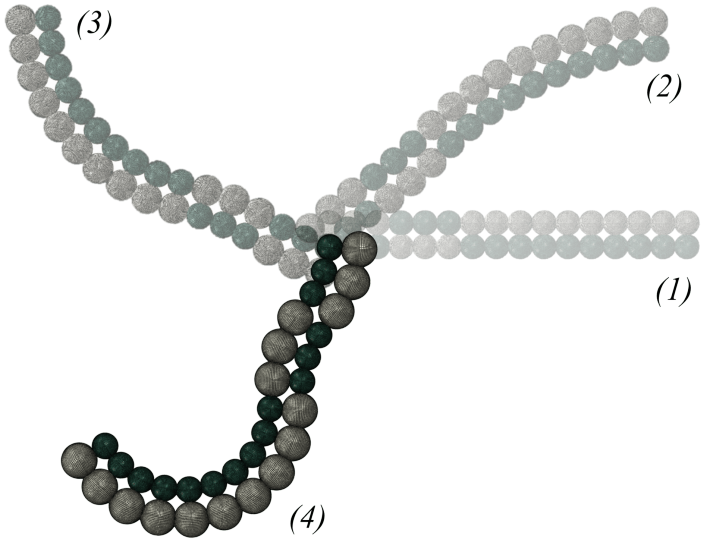

Figure 4.17: The deformed state of the C3 structure: 'The hook'.

C4 - Gripper The deformed state of this structure exhibits a transformation where the arms bend inward, forming a compact, enclosed shape, closely resembling a gripper. As seen in Figure 4.18, the four fingers curl symmetrically towards the centre, creating a spherical confinement, as evident in Figure 4.19a. The hydrogel's expansion effectively induces controlled morphing, while the silicone framework provides directional control, preventing isotropic expansion. The central region remains stable, reinforcing the role of silicone in maintaining structural integrity while allowing localized deformations.

This structure highlights the potential of hydrogel-silicone systems for adaptive gripping. The intentional design choice to leave an opening in the middle prevents numerical instability from overlapping hydrogel particles while still enabling gripping functionality. In Figure 4.19b, the circular confinement further emphasizes how hydrogel expansion allows passive conformation around an object.

Such a gripper could be integrated into robotic systems for handling fragile materials, leveraging its soft and adaptable grasp. The controlled curling motion enables conformation to various shapes while distributing pressure evenly, making it suitable for applications where the handling of fragile objects is required. Further refinements, such as optimizing hydrogel distribution or incorporating active control, could enhance precision and programmability.

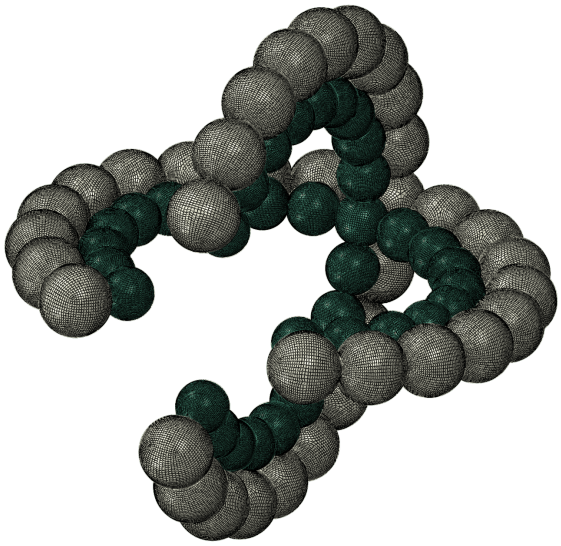

Figure 4.18: The deformed state of the C4 structure:'The gripper'.

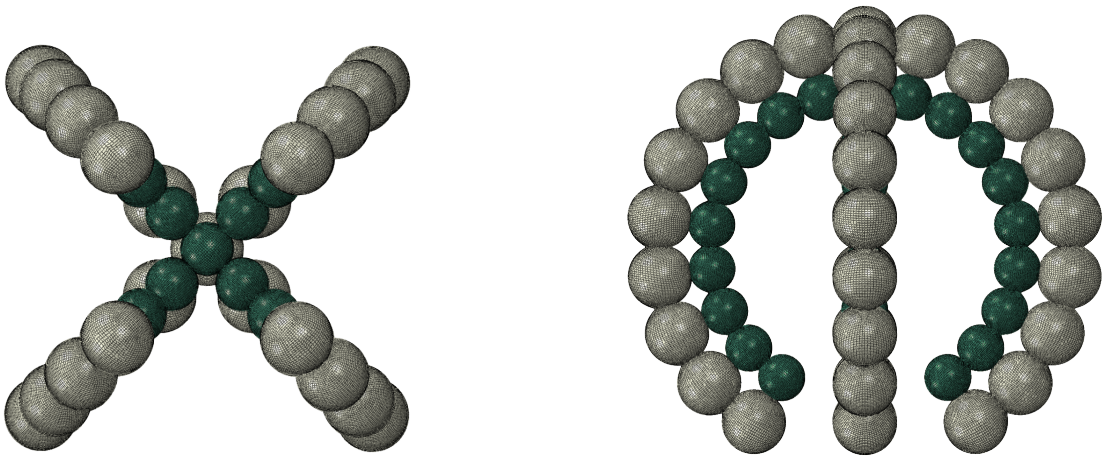

(a) Bottom view of the gripper.

(b) Side view of the gripper.

Figure 4.19: Additional views of the deformed C4 structure.

4.3.2. Meta structure design

The previous section focused on hydrogel-silicone simulations using ball-based geometries, specifically spherical configurations, to analyse their mechanical behaviour and interactions under temperature changes. However, the potential for shape morphing with hydrogels extends far beyond spherical forms, encompassing a wide range of geometric structures such as shells, surfaces, and other solid bodies.

This section shifts from a quantitative emphasis to an exploratory investigation, aiming to reveal the diverse shape transformations achievable with these alternative geometries. By focusing on the qualitative aspects of deformation and morphing, the analysis highlights the unique mechanical responses and design opportunities that emerge when different geometric forms are subjected to stimuli. This exploration seeks to uncover the interplay between geometry, material properties, and deformation, providing a broader understanding of the possibilities for complex and functional shape changes in advanced material systems. All the designs being discussed in this section are

The structure of Figure 4.20 demonstrates curling behaviour driven by hydrogel expansion and guided by the silicone framework. This structure is based on an example given in [129]. The uniform arrangement of silicone bands provides consistency in the flexing motion while preventing structural collapse. In the deformed state, the curling is evenly distributed across the finger segments, showcasing its potential as a gripper for soft robotics applications. This design is particularly effective for controlled gripping, as the silicone bands ensure predictable and repeatable deformation.

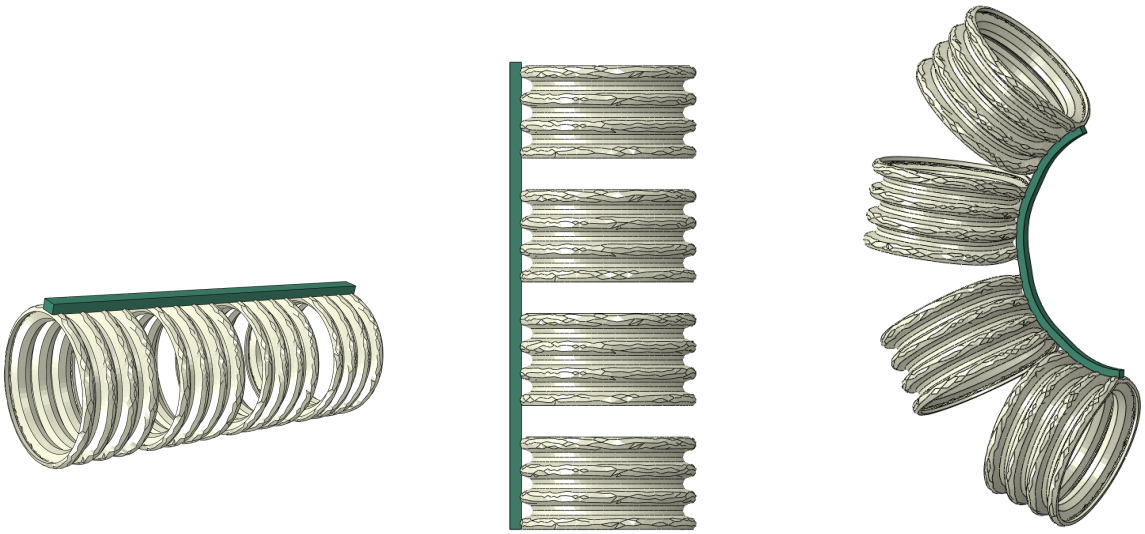

(a) Iso deformed **(b)** Side view **(c)** Undeformed

Figure 4.20: A flexible joint made of Hydrogel and Silicone to explore bending

.

The structure proposed in Figure 4.21 simplifies the structure in Figure 4.20. The curved cylinder are replaced by smooth cylinders. The deformed state reveals increased curling and folding, likely due to the additional flexibility provided by the hydrogel expansion. This model highlights the ability to achieve multi-directional gripping motions, making it suitable for applications requiring adaptable and versatile grip capabilities.

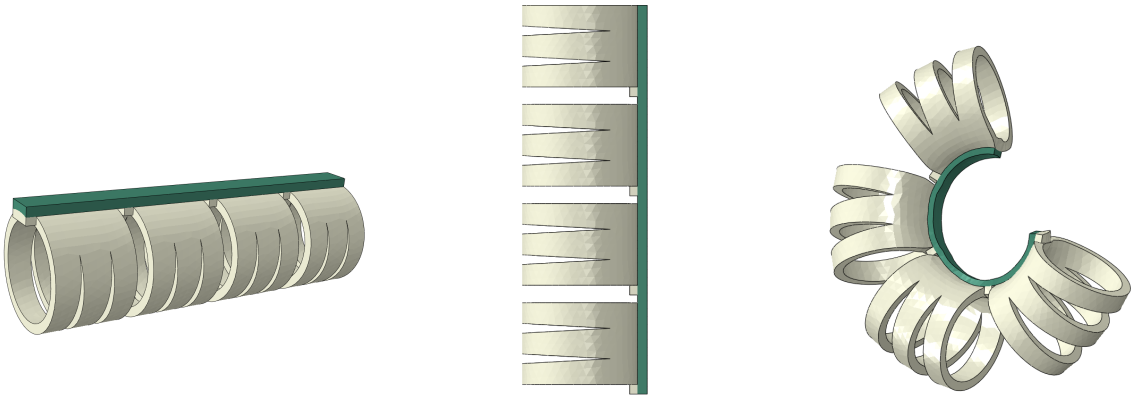

(a) Iso deformed **(b)** Side view **(c)** Undeformed

Figure 4.21: Alternate version of the flexible joint made of Hydrogel and Silicone, with no ribble structure.

The side views of both models reveal a consistent distribution of stress and deformation, reinforcing their reliability in practical use as flexible fingers in grippers in soft robotics.

Shell structures

Research into shell structures based on cylindrical geometries offers valuable insights into the deformation behaviours of hydrogel-silicone composites under expansion. The cylindrical shape, with circular outer edges made of silicone and an inner hydrogel core, serves as an excellent model for studying directional swelling and structural integrity. The contrast between the rigid silicone outer edges and the expandable hydrogel inner structure enables controlled expansion, mimicking scenarios where flexible materials deform predictably within structural constraints.

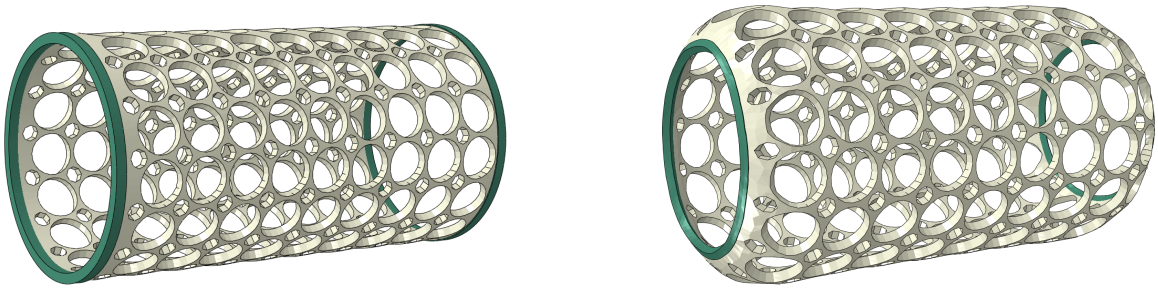

(a) Circular shell structure in the undeformed state. **(b)** Circular shell structure in the deformed state.

Figure 4.22: Shell structure using a circular structure.

The circular can design in Figure 4.22 features a grid of circular openings reinforced by silicone rings at the edges. This structure allows for significant deformation due to the larger voids in the hydrogel framework. In the deformed state, the circular openings expand uniformly, resulting in smooth and symmetric bulging. The design offers enhanced flexibility, enabling it to accommodate larger deformations effectively. However, due to the restrictions imposed by the silicone rings on either end, the side closer to the edge expands less. Therefore, making this design earn the title can, since it looks similar to a soda can.

(a) Hex-meta structure in the undeformed state.

(b) Hex-meta structure in the deformed state.

Figure 4.23: Shell structure combining honeycomb and meta structure.

The design in Figure 4.23 makes use of a hexagonal, honeycomb-like structure, and a meta-structure. While the hexagonal structure is more open in the middle, the meta-structure pattern is the opposite being more narrow in the middle. This design also includes silicone rings at both ends for structural stability. The honeycomb structure allows hydrogel swelling to produce uniform, isotropic deformation, as evident in the smooth bulging observed in the deformed state. The silicone rings constrain the deformation, ensuring the cylindrical geometry remains intact and preventing collapse or irregular bulges. It can be seen that the difference in pattern makes no difference in the deformation or expansion, only around the circular rings the meta structure opens up more due to the force narrowing of the structure diameter.

Surfaces

Research into simulations involving surface geometries, such as plates, is essential for understanding the mechanics of bending deformations and the role of material placement in achieving specific shapes. Surface geometries, compared to ball-based or volumetric structures, rely heavily on bending as a primary mode of deformation. In such systems, the intentional placement of hydrogel and silicone layers becomes a critical factor. Since hydrogel can expand in response to stimuli while silicone remains dimensionally stable, the spatial arrangement of these materials must be carefully designed to induce targeted bending behaviours. Simulating these interactions provides valuable insights into how material positioning and geometry interact to create controlled and predictable deformations, furthering the understanding of shape-morphing mechanisms in surface geometries.

The figures 4.24 til 4.28 below illustrate the deformation behaviour of various grid-based models (hexagonal, square, triangular, and circular) under hydrogel swelling. Each model combines hydrogel and silicone, with the undeformed and deformed states. These geometries highlight how silicone placement influences deformation patterns, including bending, bulging, and creasing, offering insights into controlled shape morphing for soft robotics and adaptive structures.

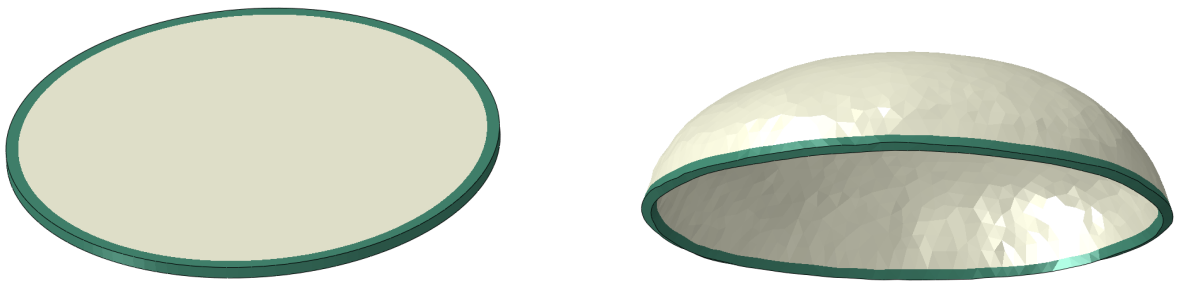

(a) Circular grid model in the undeformed state.

(b) Circular grid model in the deformed state.

Figure 4.24: Deformation of the circular grid model with hydrogel and silicone under expansion.

In Figure 4.24, the silicone functions as a circular framework around the hydrogel. This provides minimal constraints to the hydrogel and enables the hydrogel to swell up more freely closer to the centre of the

surface. This results in a smooth dome deformation with a peak in the middle. The silicone ring shows minor deformation and holds the hydrogel intact. The large hydrogel sections exert a substantial force on the silicone outer ring, however the deformation remains gradual and controlled.

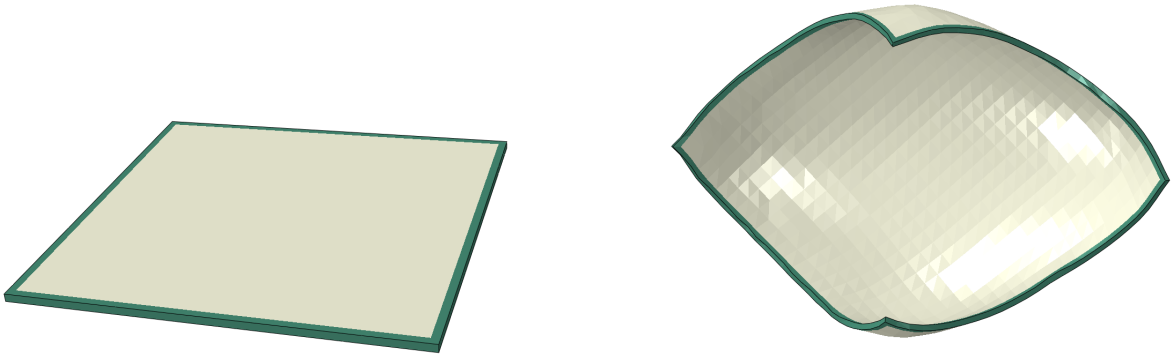

(a) Flat square model in the undeformed state.

(b) Flat square model in the deformed state.

Figure 4.25: Deformation of the flat square model with hydrogel and silicone under expansion.

Figure 4.25 has a similar setup, instead of a circle a square is seen. Its square silicone framework offers moderate constraints, leading to a balance of bending and bulging. Opposite corners are found to be contracting to each other, resulting in the structure bending around its diagonal axis. Localised stresses are redistributed across the silicone, resulting in less angular deformation and uniformity than the circular surface.

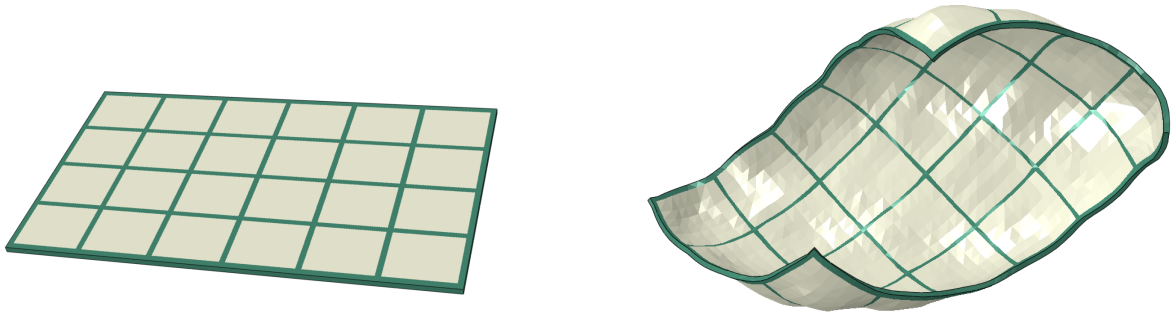

(a) Square grid model in the undeformed state.

(b) Square grid model in the deformed state.

Figure 4.26: Deformation of the square grid model with hydrogel and silicone under expansion.

The model in Figure 4.26 is an alteration of the model in Figure 4.25 by intruding smaller hydrogel sections, thus also increasing the silicone percentage. Additionally, a wider aspect ratio is used making it a rectangle instead of a square. The deformed state shows the same bending towards the diagonal. However, now along the edge, small curves can be found between each silicone bored perpendicular to the edge, since the silicone rigidity is less effective. The grid spacing and size of the hydrogel sections contribute to the observed localised deformation.

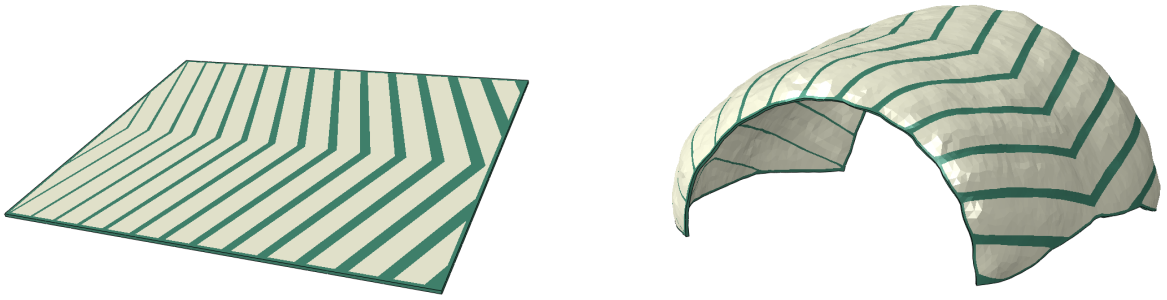

(a) Arrow grid model in the undeformed state.

(b) Arrow grid model in the undeformed state.

Figure 4.27: Deformation of the arrow grid model with hydrogel and silicone under expansion.

In Figure 4.27 sharp angles are included in the surface pattern, leading to an arrow pattern along the surface. The middle of the arrow functions as a constraint and a local minimum in the bending can be found. This grid provides the most rigid design due to its dense silicone framework, which tightly surrounds smaller hydrogel sections. The increase of the thickness of the silicone arrows from left to right of the surface has a negligible influence since the bending along the entire surface seems uniform. However, this design is the first with proper direction bending, since the bending occurs parallel to the edges.

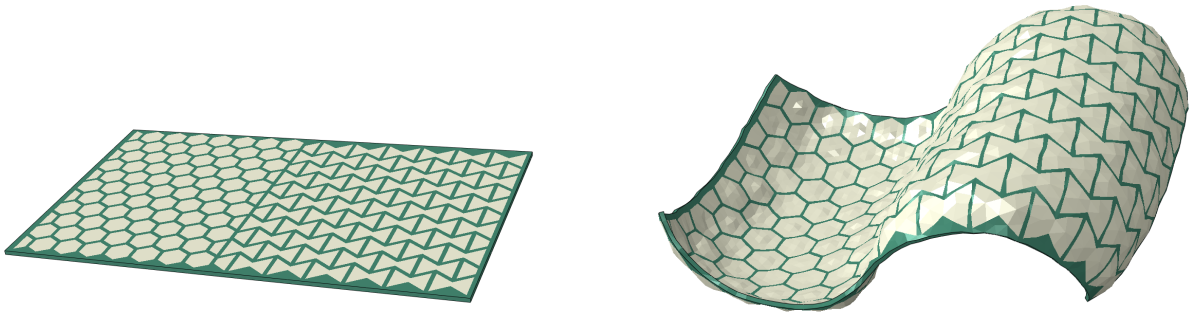

(a) Honeycomb - meta grid model in the undeformed state.

(b) Honeycomb - meta grid model in the deformed state.

Figure 4.28: Deformation of the honeycomb - meta grid model with hydrogel and silicone under expansion.

In Figure 4.28, two surface geometries have been created, combining patterns to form a symmetric honeycomb-like framework of silicone. This configuration induces bending in two directions, mimicking a wave pattern due to the interaction of the combined geometries. The hexagonal grid features continuous silicone borders around each hydrogel section, creating a symmetric framework that ensures even stress distribution and uniform hydrogel swelling. This results in smooth, dome-like bulging without sharp folds or irregularities, making it highly effective for applications requiring uniform deformation. Additionally, the diagonal parts of the meta-structure are pushed outward, causing that part of the surface to bend in the opposite direction

The interaction between hydrogel and silicone plays a key role in the deformation behaviour of these surfaces. Hydrogel swelling drives the deformation, while the silicone framework provides stability and controls its direction and extent. The patterns are largely influenced by the density and distribution of the silicone framework. The geometric design significantly impacts deformation. Symmetrical frameworks, such as hexagonal and circular grids, exhibit smoother and more consistent deformation, while denser frameworks like the triangular grid lead to angular and controlled folding. Sparse designs, such as square grids, result in sharper bends or asymmetrical bulging due to localised stress concentration. Overall, the designs highlight the importance of material placement and geometric arrangement in achieving specific deformation patterns. While the hexagonal and triangular grids show promise for controlled morphing, other designs require optimisation to reduce uncontrolled bending.

4.4. Conclusion

This chapter addressed the subquestion: **How can shape-morphing structures be developed by using smart materials?** Smart hydrogels can achieve shape-morphing by leveraging their stimuli-responsive properties and designing configurations that maximise their deformation capabilities. Various models were developed to simulate hydrogel-based structures, with temperature serving as the input variable to induce swelling. Mechanical properties, such as expansion and bending angles, were analysed to understand how hydrogels can be configured to achieve targeted morphing behaviours.

Morphing structures were designed in various configurations, including ball-to-ball setups, flexible fingers, can structures, and surface grids, each demonstrating unique deformation behaviours. Flexible fingers achieved controlled bending within a stabilising silicone framework, making them ideal for soft robotic gripping. Can structures, such as circular and hexagonal designs, highlighted the influence of geometry, with circular grids prioritising flexibility and hexagonal grids ensuring stability. Surface grids further demonstrated how symmetrical patterns enable smooth deformation, while denser frameworks support controlled folding.

Material orientation played a key role in determining deformation symmetry and direction, while structure length influenced computational complexity without significantly altering morphing behaviour. The bending angle between ball pairs remained consistent across configurations, indicating scalability. Additionally, the maximum observed diameter increase of 7.45 mm at 275 K, corresponding to an expansion factor of 1.37 in diameter and 2.59 in volume, highlights hydrogel's capacity for significant volumetric change, essential for morphing applications.

In summary, smart hydrogels achieve shape-morphing through precise material orientation, integration with supporting frameworks like silicone, and optimised geometric design. These findings emphasise the importance of tailoring configurations, such as combining symmetrical patterns with stable frameworks, to achieve precise and predictable morphing behaviours. Future work should incorporate interactions with external environments to enhance the functional versatility of these designs.

5

Multiple smart materials actuated shape-morphing structures: SMA/SMP

This chapter builds on the demonstrated effectiveness of smart materials in morphing structure design. Based on these findings, efforts were made to integrate multiple smart materials into a morphing structure. Specifically, this chapter explores the integration of Shape Memory Polymers (SMPs) and Shape Memory Alloys (SMAs), focusing on their reversible deformation mechanisms driven by temperature. It introduces constitutive models capturing SMP viscoelasticity and SMA phase transformations, highlighting their unique thermo-mechanical behaviours. This chapter also demonstrates the practical implementation of these models in the Abaqus finite element environment through simulations of SMP deformation and SMA actuation. By integrating theoretical insights with practical examples, the chapter emphasises the potential of SMPs and SMAs in enabling innovative designs.

5.1. SMAs and SMPs in Shape Morphing Actuators

As mentioned before, SMMs are a class of smart materials that are able to recover an earlier form after deformation, when exposed to certain specific external stimuli, such as electricity, heat or stress. This unique ability to 'remember' makes them highly suitable for a wide range of applications, varying robotics, biomedical and aerospace applications. Among SMMs, SMAs and SMPs stand out for their distinct mechanisms and capabilities. SMAs rely on solid-state phase transformations, switching between martensite and austenite phases to achieve shape recovery with high force output and precision. In contrast, SMPs undergo reversible transitions between glassy and rubbery states, enabling significant deformations with lightweight and flexible structures. This section explores the fundamental principles governing the behaviour of SMAs and SMPs, highlighting their unique properties, activation mechanisms, and potential integration into advanced designs. Their complementary characteristics make them essential materials for innovative solutions in responsive and adaptive systems. SMAs and SMPs are both highly regarded for their ability to undergo reversible deformation, making them ideal candidates for shape-morphing actuators. Each material offers distinct advantages that complement the other, resulting in a synergistic combination for achieving controlled, adaptive structures.

SMAs

SMAs are known for their ability to recover their original shape when heated, driven by the SME. They generate substantial forces, making them ideal for deformation-driven applications. Additionally, SMAs exhibit superelasticity, which allows them to resist large strains and recover fully upon unloading. This property is particularly valuable for providing controlled, repeatable actuation. In this research, SMAs were employed to produce the forces required for bending.

SMPs
SMPs can undergo large, reversible deformations when exposed to temperature changes. They are unique in that they can lock into a temporary shape at lower temperatures and recover their original configuration when heated. This ability provides stability and adaptability for shape-morphing designs. Furthermore, SMPs enable energy-efficient shape retention by locking into deformed shapes without requiring continuous energy input. In this research, SMPs served as the flexible medium to accommodate and lock the bending motions generated by the SMAs.

Applicability in Shape Morphing
SMAs and SMPs are uniquely suited for shape-morphing applications because they bring together complementary properties. Both materials are capable of reversible deformation, a critical feature for shape-morphing systems. SMAs generate the high actuation forces necessary for significant deformation, while SMPs offer the flexibility and adaptability needed for diverse morphing behaviours. SMPs also contribute to energy efficiency by locking into deformed shapes without the need for continuous energy input, making them ideal for applications that require a fixed configuration. Both materials respond to thermal stimuli, enabling synchronized actuation and controlled deformation, which enhances their versatility. The combination of SMAs and SMPs allows for precise and adaptable morphing capabilities.

Combination of SMAs and SMPs
The integration of SMAs and SMPs offers significant advantages for shape-morphing actuators. SMAs provide the actuation force required for deformation, while SMPs enable temporary locking and smooth recovery of shapes. The temperature responsiveness of both materials allows for synchronized actuation, facilitating multi-directional morphing. This combination enhances energy efficiency and enables complex, multi-directional morphing in actuator designs. The integration is particularly effective in multi-cylinder setups, where the actuators can achieve multi-directional shape morphing. SMAs and SMPs also demonstrate their potential for advanced applications, including soft robotics and dynamic structural systems, by providing a versatile foundation for the development of actuators capable of addressing complex functional requirements. This synergistic combination leverages the respective strengths of both materials, offering a powerful solution for designing adaptable and energy-efficient shape-morphing actuators.

5.2. Constitutive equations SMP and SMA

5.2.1. SMA model

Due to external stimuli caused by the change of the microscopic phase transformations of the phases austenite and martensite, SMAs have the macroscopic mechanical properties of the SME and SE. The stress-strain constitutive model encompasses both complex mechanical properties and phase transformations [130].

Adjusted Brinson Model

The behaviour of the SMA material relies on variables such as the stress, temperature and the crystal structure, the latter depends on the loading and thermal histories. The constitutive model is based on loading (tensile force) at a low temperature, unloading and then heating [131]. To account for this, in SMAs an internal variable is introduced ξ. This depicts the condition of the materials as a martensite material fraction, with $\xi = 0$ indicating the material is fully in the austenite phase. The created martensite has two results, twinned or detwinned [132]. Twinned indicates multiple martensite variants coexisting, while detwinned suggests a connection with one dominant variant, as expressed in Equation 5.1,

$$\xi = \xi_S + \xi_T \tag{5.1}$$

where the subscript S stands for stress-induced and T for temperature induced. The model is an adjusted model for the situation of a simple one-dimension SMA model proposed by Brinson [133] and is given in Equation 5.2,

$$\sigma - \sigma_0 = E(\xi)\varepsilon - E(\xi_0)\varepsilon_0 + \Omega(\xi)\varepsilon_S - \Omega(\xi_0)\varepsilon_{S0} + \Theta(T - T_0) \tag{5.2}$$

with σ depicting the stress currently resisted in the material, $E(\xi)$ is the elastic modulus depending on the current crystal structure, ε is the strain experienced by the material and Θ is the thermal response shown by the material. All the variables with the 0 subscript indicate the initial state. The phase transformations for the SME for the material are given in Figure 5.1, with subscript s indicating the start and f the final stage.

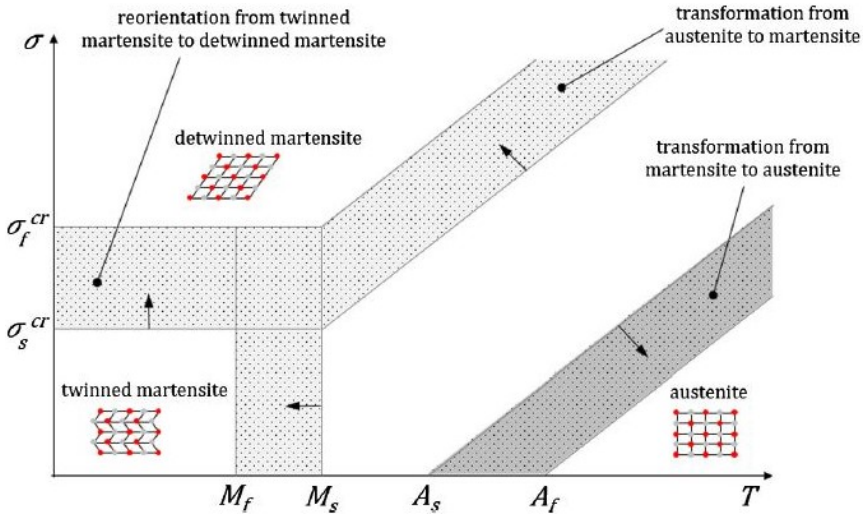

Figure 5.1: The phase diagram of SMAs based on Buljak et al. [131].

Macroscopic Models

The macroscopic models depict the behaviour of SMAs based on phenomenological considerations, simple micromacro thermodynamics or experimental data. The mentioned model in this section is a pioneering model which is used as a foundation for specific applications of models made for SMAs. This model has attributed to major developments in the modelling of SMAs [134].

Boyd and Lagoudas - Phenomenological Model

This model is based on an energy potential which is taken from physical considerations [135]. In this case, the state equation of this model is derived from the following Gibbs free energy potential [136], with ψ_A and ψ_M being the free energies of austenite and martensite. ψ^{mix} indicates the mixing term reflecting on the different interactions between the two phases. This is the first model that takes into consideration the reorientation of martensite by including an inelastic strain tensor,

$$\Psi\left(\boldsymbol{\sigma}, T, \xi, \boldsymbol{\varepsilon}^{\mathrm{tr}}\right) = (1-\xi)\Psi_{\mathrm{A}}(\boldsymbol{\sigma}, T) + \xi\Psi_{\mathrm{M}}(\boldsymbol{\sigma}, T) + \Psi^{\mathrm{mix}}\left(\xi, \boldsymbol{\varepsilon}^{\mathrm{tr}}\right), \tag{5.3}$$

the following stress-strain relation of Equation 5.4 is used in this model,

$$\boldsymbol{\sigma} = \left[\xi \boldsymbol{S}_{\mathrm{M}} + (1-\xi)\boldsymbol{S}_{\mathrm{A}}\right]^{-1} : \left[\boldsymbol{\varepsilon} - \boldsymbol{\varepsilon}^{\mathrm{tr}} - \boldsymbol{\alpha}\left(T - T_0\right)\right]. \tag{5.4}$$

In literature other models can be found, mostly having a different level of detail in describing key aspects of SMA behaviour. Some are alterations or derivations of existing models, like the one above. However, the model above is one of the fundamental ones, therefore it is included in this study for SMA behaviour.

5.2.2. SMP models

To accurately describe the mechanical behaviour of SMPs, a superimposed generalised Maxwell model in conjunction with the Williams-Landel-Ferry (WLF) equation is employed within the Abaqus finite element solver. These constitutive equations account for the time-dependent viscoelastic response of SMPs and enable accurate modelling of their thermo-mechanical behaviour.

The stress evolution over time, $\sigma(t)$, is governed by the generalised Maxwell model:

$$\sigma(t) = \varepsilon_0 E_n + \varepsilon_0 \sum_{i=1}^{n-1} E_i e^{\frac{-t}{\tau_i}} \tag{5.5}$$

where $\sigma(t)$ represents the stress at time t, ε_0 is the initial strain, E_n is the instantaneous modulus, E_i denotes the elastic modulus of each Maxwell element, and τ_i is the relaxation time associated with the Maxwell element i. In the generalised Maxwell model the relaxation modulus $E(t)$ is given by:

$$E(t) = E_n + \sum_{i=1}^{n-1} E_i e^{\frac{-t}{\tau_i}} \tag{5.6}$$

subject to the limiting condition:

$$\lim_{t\to\infty} E(t) = E_n \tag{5.7}$$

To unify relaxation response curves of SMPs across various temperatures, the time-temperature equivalence principle is applied, allowing transformation into a single master curve at a chosen reference temperature. The shift in relaxation time due to temperature variation is modelled using the WLF equation:

$$\log \alpha_T = \log \frac{\tau}{\tau_r} = \frac{-C_1(T - T_r)}{C_2 + (T - T_r)} \tag{5.8}$$

where α_T is the shift factor, C_1 and C_2 are material constants, T is the current temperature, and T_r is the reference temperature. This modelling framework allows for an accurate representation of the viscoelastic and thermomechanical behaviour of SMPs, facilitating the simulation of their deformation and recovery characteristics within finite element analyses. The constitutive equations incorporated into Abaqus provide a comprehensive understanding of SMP behaviour under varying thermal and mechanical conditions.

5.3. Designed structures

In the previous chapter, various hydrogel configurations were designed and tested to explore their deformation and potential applications. Building on those findings, this chapter focuses on the design and development of a structure that integrates SMAs and SMPs to create a composite actuator. This actuator aims to leverage the unique capabilities of both materials: the high actuation force of SMAs and the large deformation recovery of SMPs, offering a versatile solution for adaptive systems. In this study, Polylactic acid (PLA) was chosen as the SMP and the Ni-Ti alloy as the SMA [137].

The insights gained from hydrogel configurations in the previous chapter provide valuable guidance for this design process. Key ideas, such as spatial arrangement, functional layering, and material distribution, can be adapted to combine SMA and SMP components effectively. For instance, concepts related to optimized geometry and responsive design principles from the hydrogel studies can be applied to ensure the efficient integration of SMA and SMP. Additionally, lessons on material behaviour under external stimuli, as observed in hydrogels, can inform the placement and activation strategies for the actuator.

5.3.1. Requirements

The final design of the actuator should be able to fulfil a list of requirements. These can be found below:

- The structure must be able to implement shape morphing in its structure by the use of the properties of the smart material and the structural design choices made in the geometry. Therefore, making it flexible.
- The actuator must not only be rigid but also capable of adjustable deformation, making it adaptable.
- The dimensions must be fit to a size of 250 mm x 250 mm x 250 mm, which enables the option to create a real-life prototype with the tools given by the faculty.

The design process is summarized in figure Figure 5.2.

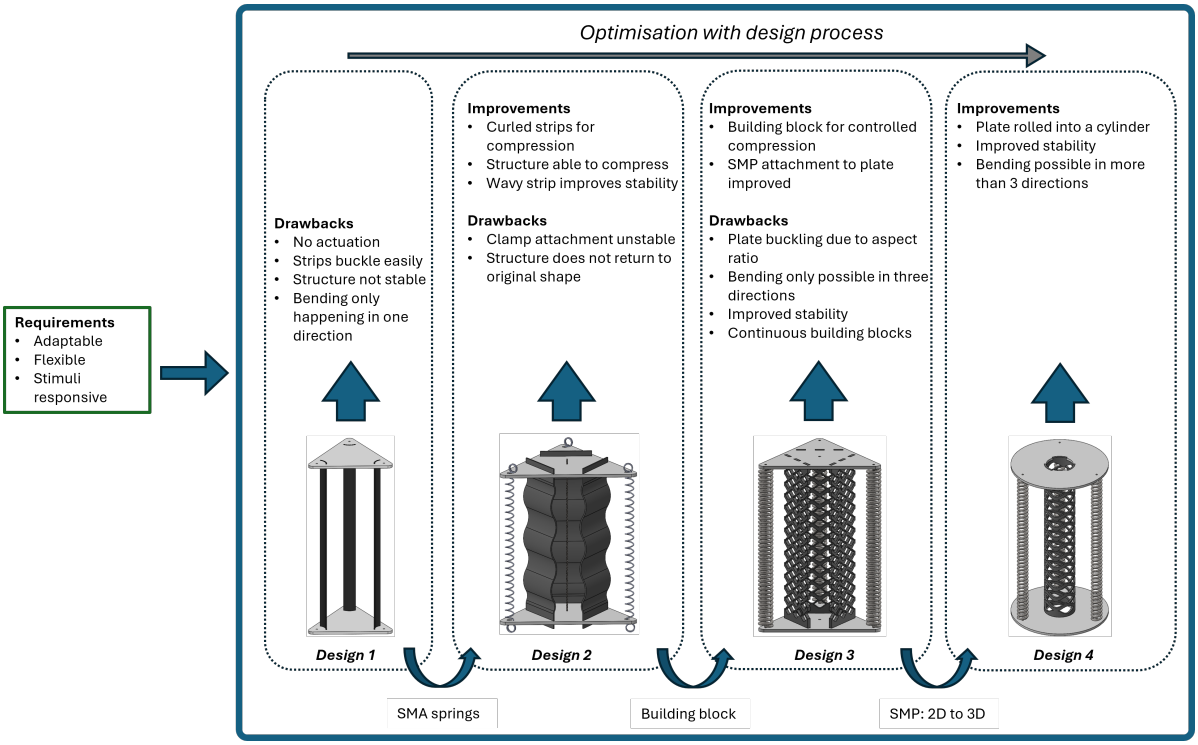

Figure 5.2: The design steps followed during iterations of the SMP designs.

5.3.2. First design

The initial design concept consists of two PMMA plates connected by three SMP strips, enabling deformation in response to thermal stimuli. The primary purpose of the SMP strips is to deform when heated, causing the structure to bend. The PMMA plates are chosen for their thermal stability, ensuring that they remain rigid and do not deform under heat.

In this configuration, the top PMMA plate is fixed, while the bottom plate is allowed to move, facilitating the desired bending motion. The design, as illustrated in Figure 5.3a, is straightforward, consisting of five components, with two unique elements: the PMMA plates and the SMP strips. The PMMA plates are 3 mm thick and feature cutouts designed to accommodate the sliding of the SMP strips, ensuring a secure and functional assembly. The SMP geometry is a curved strip, and curvature was added for stability.

The primary function of the three SMP strips is to facilitate bending or deformation in response to the movement of each PMMA plate. While they also contribute to maintaining the structural connection between the plates, this role is secondary. Challenges with this design include difficulty in bending the plates toward the inner curve side due to their slight curvature, which limits effective deformation to only one of the three strips, with the other two remaining less responsive. Additionally, the bending process requires the application of an external force, posing further limitations on the overall efficiency of the design.

(a) Initial sketch up design **(b)** Initial board design

Figure 5.3: Details of SMP-Actuator 1

5.3.3. Second design - SMA coil implementation

The second design introduces a different SMP geometry. Instead of a curved plate, a wave-patterned plate is utilized to enable bending in both directions perpendicular to the curved surface, a limitation of the previous design. Additionally, the strips are made straight in their thinnest direction, rather than slightly curved, as shown in Figure 5.5.

The biggest difference is the addition of a third component, the SMA coil spring. In this actuator design, SMA coil springs serve as the primary actuation mechanism, driving deformation in the structure. The SMA springs are positioned to exert a compressive force on the PMMA board, as can be seen in Figure 5.4. The board being attached to the SMP, causes directional bending. A coil spring geometry is particularly advantageous for SMAs in this context, as it maximizes the material's ability to deliver force and displacement efficiently.

When heated, the SMA coil spring undergoes a phase transformation that results in contraction along its axis. The coiled configuration enhances the SMA's ability to generate significant force while accommodating substantial deformation, making it ideal for compact actuator designs. This geometry also ensures even stress distribution within the spring, improving durability and performance over repeated actuation cycles [138].

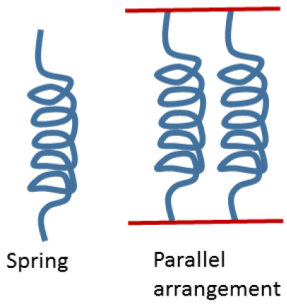

Figure 5.4: SMA coil spring arrangement to apply a force with [139]

The contraction of the SMA coil spring applies a precise compressive force on the SMP geometry, bending it toward the side of the activated spring. By utilizing the SMA coil's high actuation efficiency and controlled thermal response, the actuator achieves reliable, directional deformation with minimal mechanical complexity. This combination of the SMA coil spring's geometry and thermal responsiveness makes it a critical component for creating actuators with precise motion control and adaptability.

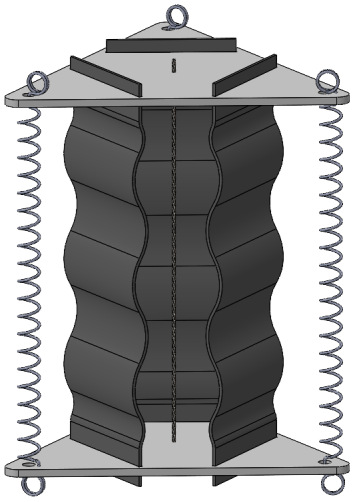

(a) Total assembled visual of the second design in SolidWorks.

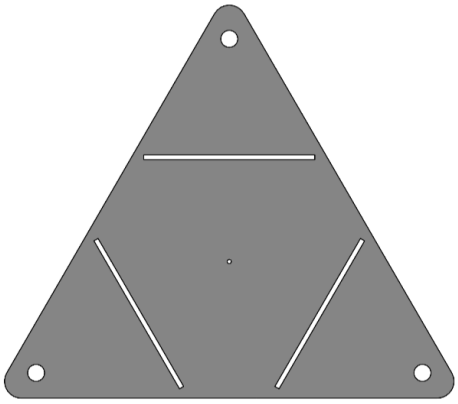

(b) Second PMMA board design with slits for SMP strips and SMA springs.

Figure 5.5: The second actuator design with wave strips, PMMA boards and SMA springs

5.3.4. Third design - Intelligent Building Block

The third design introduces the Intelligent Building Block, a structural element composed of two interconnected segments with distinct properties. As illustrated in Figure 5.6a, the lower segment is thicker and stiffer, serving as the rigid component, while the upper segment is thinner and more flexible. The geometry of these segments is inspired by a sinusoidal wave pattern, with a critical difference in the alignment of their peaks. When the flexible upper segment reaches a maximum, the rigid lower segment aligns with a minimum, creating a gap between the two segments. This gap features a maximum opening at the midline of the structure.

During load-bearing processes, the rigid lower segment remains largely undeformed, providing structural stability. In contrast, the flexible upper segment undergoes buckling and reversible deformation, which can be seen in Figure 5.6b. This design enables the Intelligent Building Block to exhibit reconfigurable deformation and tunable mechanical energy absorption. The structure can transition between multiple stable configurations, effectively absorbing energy and achieving self-expansion through fully reversible deformation mechanisms. This innovative design highlights the potential of SMP metamaterials for applications requiring adaptability, energy absorption, and stability in complex loading conditions [140].

(a) Undeformed state of the structure

(b) Structure with the upper section buckled

Figure 5.6: Intelligent Building Block

The precise geometry of the Intelligent Building Block is governed by sinusoidal waveforms, as shown in Figure 5.7a. The structure consists of four sinusoids, divided into two pairs. Each pair is parallel and connected at the outer ends. The offset between the waveforms is determined by the thickness of the segments. Specifically, the upper segment has a thickness of 1.8 mm, while the lower segment's thickness is calculated as 4.5 mm minus the thickness of the upper segment, resulting in 2.6 mm. Each of the waves follows a simple equation, with a full wave reaching 30 mm. The sole variation in the equation is the sign before the cosine, which determines whether the wave is on the top or lower segment. The equation for sinusoids was employed in the parameters for the equation-driven curve, as shown in Figure 5.7b, with 0 being the beginning and 30 being the endpoint.

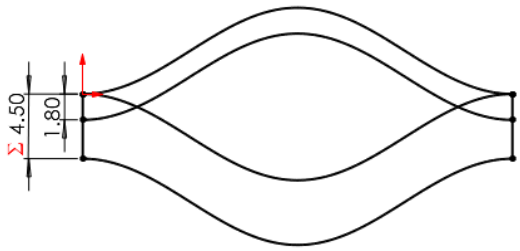

(a) Sketch of the block as used in SolidWorks.

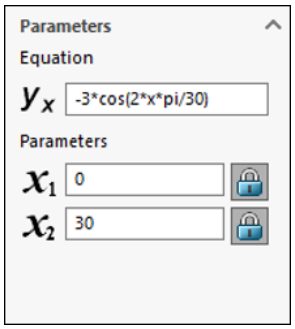

(b) Equation used to sketch the sinusoid curve for the block.

Figure 5.7: Intelligent building block parameters

To implement the block into a plate geometry, an array of these blocks have been placed together horizontally and vertically. A straight part has been added to the end of both sides, with rectangular cutouts to be used as slots for attachment to the PMMA boards. The front view of the geometry can be seen in Figure 5.8.

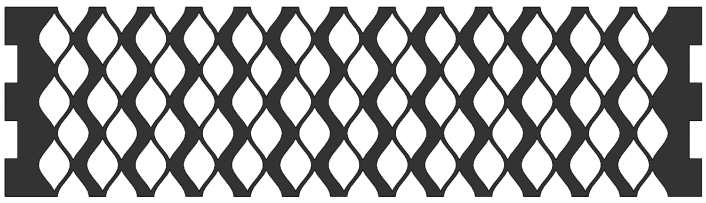

Figure 5.8: SMP strip consisting of building blocks (rotated)

The complete assembly can be found in Figure 5.9a. A cross-section of the design in the middle can be found in Figure 5.9b.

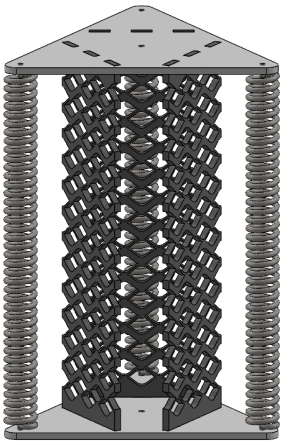

(a) Total assembly of the entire third design including SMA springs, SMP plates and PMMA boards.

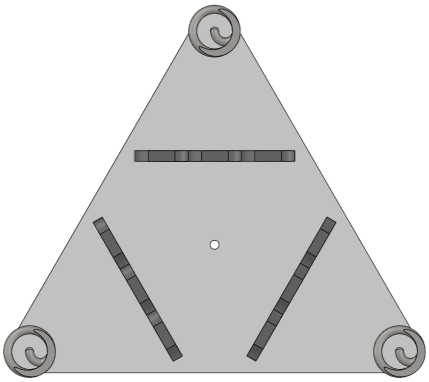

(b) Crossection of the assembly

Figure 5.9: Total assembly design 3

5.3.5. Fourth design - Cylindrical SMP structure

The fourth design introduces a novel geometry for the SMP to enhance structural stability. In this iteration, the SMP plates from the intelligent building block are reshaped into a cylindrical structure. This cylindrical geometry significantly reduces the likelihood of buckling due to its increased geometric stiffness compared to the previous configuration of three independent plates. Furthermore, the continuous geometry of the cylinder, composed of building blocks in all directions, allows bending in multiple directions. Similar to the previous design, circular slots are incorporated to securely attach the cylinder to the boards, ensuring functionality and integration, which clearly can be seen in Figure 5.10b. The entire assembly can be found in Figure 5.10a. The general are chosen, that the structure fits in a box with a size of 250 mm x 250 mm x 250 mm, which enables the option to create a real-life prototype with the tools given by the faculty.

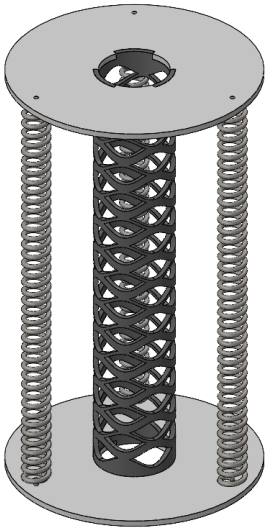

(a) Total assembly of the complete fourth design including SMA springs, SMP cylinder and PMMA boards.

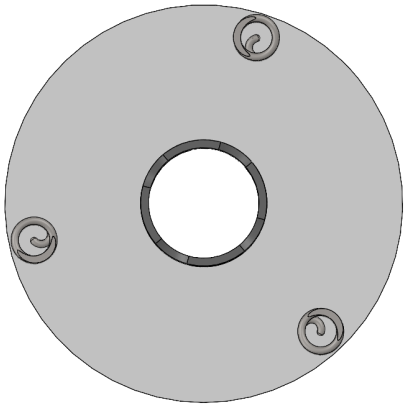

(b) Crossection of the fourth assembly

Figure 5.10: Total assembly design 4

Additional specifications and dimensions of this design can be found in section D.1. The designs have been experimentally tested by printing PLA (SMP) with a 3D printer. Experimental findings found on structures mentioned here can be found in Appendix E.

5.4. Simulation setup

Similar to the hydrogel models, the simulation process will be conducted in multiple stages. Initially, the material properties and geometry will be defined. Subsequently, a mesh sensitivity analysis will be conducted. Following this, environmental dynamics relevant to the model will be incorporated, and finally, appropriate boundary conditions will be applied to complete the setup.

Material

ABAQUS will be precisely used to determine the deformation of the different SMP configurations. The material simulated in this study consists of an SMP as the primary material, an SMA as the secondary material, and PMMA as the support material. PMMA is lightweight and strong. The density is around half of that of glass, making it a good option for weight reduction. Furthermore, the material behaves stable in response to several environmental conditions [141]. The properties of SMPs as well as SMAs are not included in the material library of ABAQUS, therefore these are defined manually by using the consecutive equations mentioned in section 5.2. Again, a hyperelastic input is needed in the material library depending on a few variables. For SMA and SMP the viscoelastic and thermal property parameters are specified as follows [142]:

For SMA the following is used:

- Martensite: M_s = 325 K and M_f = 315 K with Youngs modulus E_m = 28 GPa
- Austenite: A_s = 341 K and A_f = 351 K with Youngs modulus E_a = 75 GPa

For the SMP the following is used:

- T_g = 334 K, E_{SMP} = 400 MPa at T_g
- C_1 = 6.14, and C_2 = 293 K
- T = 298 K, E_s = 1000 MPa

At a temperature of 298 K, the material's elastic modulus was 1000 MPa, but it decreased by 60% upon reaching the transition temperature. For PMMA the standard material properties are used as seen in Table 5.1

Table 5.1: Typical PMMA Material Properties

Property	Value
Density, ρ	1180 kg/m^3
Young's Modulus, E	2.4–3.2 GPa (common: 3.0 GPa)
Poisson's Ratio, ν	0.35
Tensile Strength (at break)	60–70 MPa
Thermal Expansion Coefficient, α	5×10^{-5} K^{-1}

Geometry

The geometry comprises an SMP cylinder, two PMMA plates, and three SMA springs, as described previously. In this chapter, the SMP is represented by black geometry, the SMA by dark grey, and the PMMA by light grey. This colour distinction will be consistently applied across other configurations. Unlike the spherical geometries used in the hydrogel models study, all geometries and components in this study are designed in SolidWorks due to their geometric complexity. The Abaqus parts module is utilized solely for importing the geometries and assemblies from SolidWorks. Consequently, proper alignment and constraints are required to ensure the assembled geometry is correctly positioned in the Abaqus environment. The lower PMMA plate is aligned and assembled at the global origin (0,0,0) of the environment, ensuring that the bending direction aligns with the Z-axis. This setup facilitates easier observation of bending, as the ZY plane is perpendicular to the two-spring actuation method. The remaining components are constrained relative to the bottom plate, and the entire assembly is subsequently merged into a single geometry.

Mesh

For the SMP model, the merged geometries were meshed for the simulation using the C3D10 element type. This mesh type was chosen due to the complex geometry of the SMA springs and the curved edges found in the SMP geometries. In this mesh sensitivity study, the bending angle is again selected as the primary variable to assess the influence of mesh size on the model's performance, which for this model can be found in Figure 5.11.

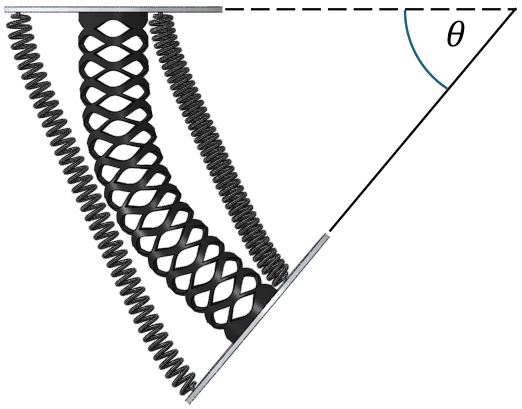

Figure 5.11: The bending angle in the cylinder model.

The default mesh size in Abaqus, set at 10mm, serves as the baseline, with additional analyses conducted for mesh sizes ranging from 30 (coarse) to 1.5 (fine). This corresponds to approximately 15,000 to 440000 elements, as illustrated in Table 5.2. The plot for the relationship between the angle and elements can be found in the Appendix in Figure C.3.

The convergence study systematically refines the mesh to observe variations in the bending angle, with data to be found in Table 5.2. The objective is to determine a mesh size where further refinement results in negligible changes, visually indicated by the curve flattening or nearing an asymptote in Figure 5.12.

Table 5.2: Mesh sizes with a corresponding number of elements and bending angles for SMA-SMP model mesh sensitivity analysis.

Mesh size [mm]	Number of elements [-]	θ [deg]
1.5	$4.35 \cdot 10^5$	50.6
1.75	$2.87 \cdot 10^5$	50.5
2	$2.06 \cdot 10^5$	50.3
2.5	$1.28 \cdot 10^5$	50.0
3.5	$8.82 \cdot 10^4$	49.5
4.5	$6.72 \cdot 10^4$	48.3
5.5	$4.89 \cdot 10^4$	50.2
7.5	$4.27 \cdot 10^4$	47.0
10	$3.87 \cdot 10^4$	45.7
12.5	$3.42 \cdot 10^4$	45.6
15	$2.55 \cdot 10^4$	46.4
20	$1.73 \cdot 10^4$	46.5
30	$1.47 \cdot 10^4$	41.7

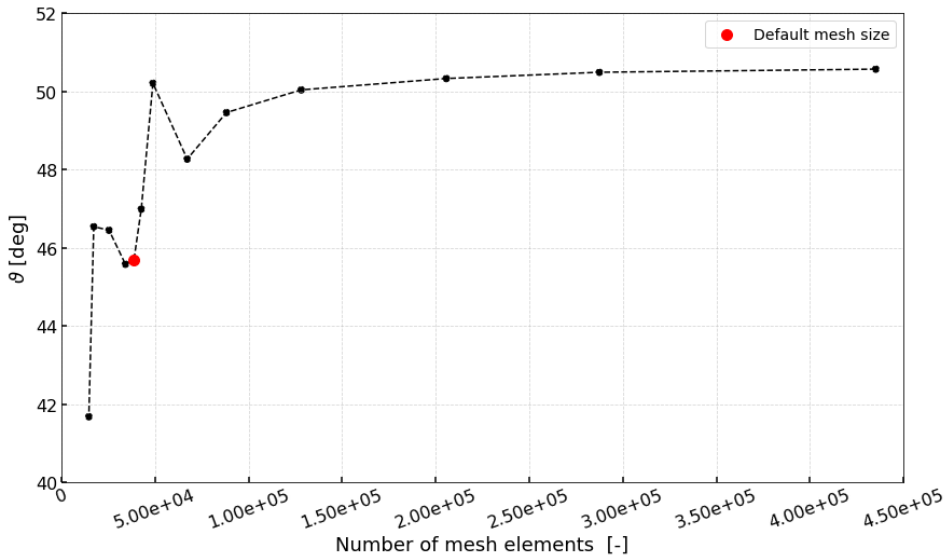

Figure 5.12: The bending angle plotted against the number of mesh elements for SMA-SMP models.

The red dot in Figure 5.12 represents the default mesh size, corresponding to a value of 10 mm. It is evident that this value does not provide a stable choice, as significant variations in the bending angle are observed near this point. Convergence is quantitatively assessed using a threshold, defined as the percentage change in the bending angle between successive refinements. For the SMP models, a threshold of 2% is applied. With this threshold in mind, a convergence study is conducted using Equation 5.9, where θ_n denotes the refined bending angle and θ_{n-1} represents the bending angle from the previous refinement. The output of this study can be found in Figure C.4 in section C.2.

$$\Delta_{c,s} = \left| \frac{\theta_n - \theta_{n-1}}{\theta_{n-1}} \right| \times 100 \tag{5.9}$$

However, in this section the relative bending angle compared to the most accurate result will be discussed. For this Equation 5.10 was used with θ_N being the most accurate bending angle, corresponding with the largest number of mesh elements.

$$\Delta_{f,s} = \left| \frac{\theta_N - \theta_n}{\theta_n} \right| \times 100 \tag{5.10}$$

By looking at these results in Figure 5.13, it is evident that the most accurate results are achieved with the smallest mesh size which comes down to $4.35 \cdot 10^5$ elements. However, $1.28 \cdot 10^5$ elements represent the first instance where the simulated results fall within the defined convergence thresholds, with a delta value of 1.17%, as shown in Table 5.3. Consequently, a corresponding mesh size of 2.5 will be adopted for the simulations in this part of the study, as it provides an optimal balance between computational efficiency and result accuracy.

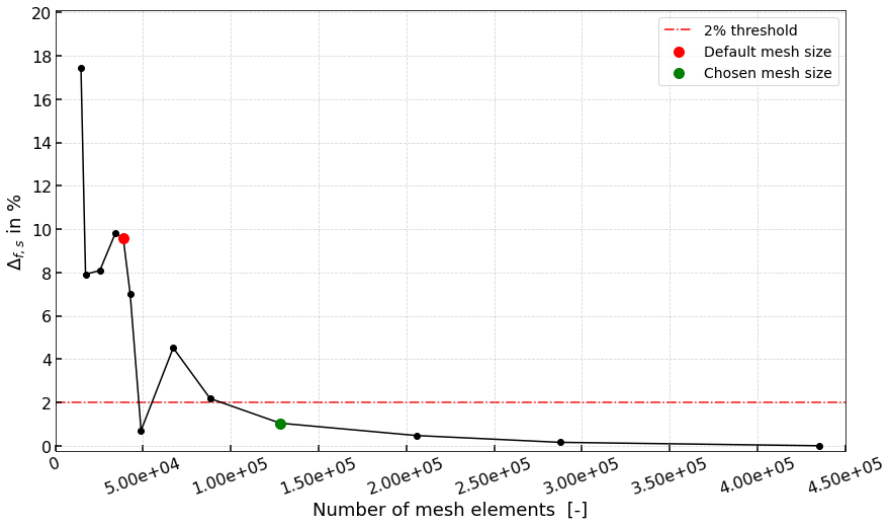

Figure 5.13: Plot showing the percentage difference in bending angle, relative to the final (most accurate) mesh configuration, for varying mesh element counts for SMA-SMP models.

Table 5.3: Percentage difference in bending angle for various mesh element counts, calculated relative to the final (most accurate) mesh configuration of the SMA-SMP models. The chosen number of elements is indicated in bold.

Number of elements [-]	$\Delta_{f,s}$ in%
$4.35 \cdot 10^5$	0.00
$2.87 \cdot 10^5$	0.157
$2.06 \cdot 10^5$	0.471
$1.28 \cdot 10^5$	*1.04*
$8.82 \cdot 10^4$	2.18
$6.72 \cdot 10^4$	4.52
$4.89 \cdot 10^4$	0.707
$4.27 \cdot 10^4$	7.03
$3.87 \cdot 10^4$	9.61
$3.42 \cdot 10^4$	9.80
$2.55 \cdot 10^4$	8.09
$1.73 \cdot 10^4$	7.92
$1.47 \cdot 10^4$	17.5

Timesteps

The simulation employs timesteps to accurately capture the deformation behaviour of the cylinder and springs. A viscoelastic analysis approach is utilized, with each timestep subdivided into increments ranging from 20 to 50, depending on the complexity of the simulation. For each timestep, a predefined field is applied with a specific temperature value, resulting in two distinct steps, each corresponding to a unique temperature level. Each step is set to a duration of 1 second, culminating in a total simulation time of 2 seconds. A full Newton solver technique is implemented, employing a direct solver approach rather than an iterative one.

Boundary conditions

In these simulations, the cylinder is fixed at one end to prevent translation or rotation (U_x = U_y = U_z = 0, R_x = R_y = R_z = 0). The fixed end in this case is the circular surface of the upper PMMA board. Therefore enabling an anchor point of the model, instead of a free-floating geometry, this can be seen in Figure 5.14. The initial conditions assume that the cylinder is undeformed, with no forces applied. A vertical load is applied on each of the springs, to capture the behaviour of a pre-loaded spring. This

has been done on the surface of the outer end of the spring, towards the board. Depending on the actuation, the number of active springs will vary between 1 to 3. Lastly, a predefined field is assigned with different temperatures for each stage. In this study, only the cylinder is subjected to temperature changes. An initial ambient temperature is handled for the first stage with a temperature of 20 degrees Celsius (293.15 K), in the second stage a heated stage is needed with a temperature of 75 degrees Celsius (348.15 K). Contrary to the first study focused on hydrogel, the geometry is heated instead of cooled. Since the objective of this study is to observe geometry deformation resulting from temperature increases, other forces such as gravity or friction were considered irrelevant and were excluded from the scope of the research for this model.

Table 5.4: Parameters used in the simulation setup for the SMP setups.

Parameters	Value/type	Unit
Material 1	SMP	-
Material 2	SMA	-
Material 3	PMMA	-
Geometry height	220	mm
Geometry width	126	mm
Initial temperature	293.15	K
Final temperature	348.15	K
Temperature step	55	K
Duration step	1	s

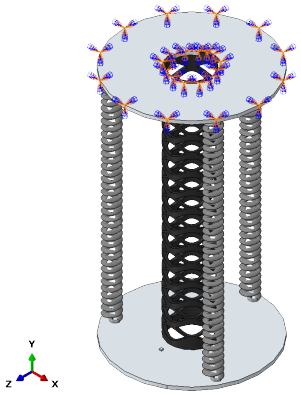

Figure 5.14: Boundary conditions applied on the top plate of the model.

5.5. Geometric parameter tuning

For the final design, a sensitivity analysis is conducted to evaluate the influence of the dimensions of the intelligent building block on bending behaviour. This analysis focuses on four key parameters: the cylinder thickness (C_t), block width (B_w), segment ratio (R_s), and block height (B_h). Adjustments to these parameters were made to evaluate their impact on the design's performance. The parameter values were carefully chosen to ensure that the geometry remains feasible for the patterned structure of the block. This ensures that the fundamental concept and generic shape of the building block, including its buckling mechanism, are preserved.

- $\boldsymbol{B_h}$: The minimum height was chosen to ensure that a gap between the two layers remains present; otherwise, the structure cannot deform properly. The sinusoidal wave influences the height of the block, with its amplitude corresponding to four times the block height. For instance, an amplitude of 2 mm results in a block height of 12.5 mm ($\mathbf{4 \cdot 2 + 4.5}$), where 4.5 mm is the thickness of the block's side. Similarly, an amplitude of 4 mm leads to a block height of 20.5 mm ($\mathbf{4 \cdot 4 + 4.5}$).
- $\boldsymbol{B_w}$: The maximum block width ($\boldsymbol{B_w}$) was limited to 60 mm to ensure that the building blocks were evenly divided into the 120 mm width of the rolled plate, which is used to form the cylinder. For example, $\boldsymbol{B_w = 10}$, **20**, or **30** mm fit 12, 6, and 4 times, respectively, while $\boldsymbol{B_w = 25}$ mm is not permissible as $\mathbf{120/25}$ does not result in an integer. A width of $\boldsymbol{B_w = 120}$ mm is also excluded, as it would leave the structure supported on only one side, reducing stability. Thus, $\boldsymbol{B_w = 60}$ mm is the maximum permissible block width.
- $\boldsymbol{R_s}$: The segment ratio is defined as $\boldsymbol{s_1/s_2}$. The minimum ratio was set to 0.2, resulting in a minimum thickness of 0.9 mm. This ensures sufficient overlap between repeated cell structures. The maximum ratio was set to 1.0, corresponding to $\boldsymbol{s_1 = s_2}$. This configuration makes the top and bottom sides equal, resulting in a symmetrical structure.
- $\boldsymbol{C_t}$: An inner diameter of 35 mm was set as standard, requiring any changes in thickness to be achieved by adjusting the outer diameter.

The mentioned parameters can be found in Figure 5.15 and the specific values used in this analysis are detailed in Table 5.5.

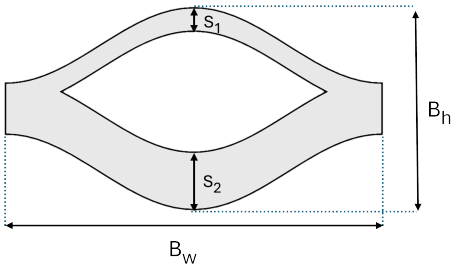

(a) Parameters defined in the geometry of the intelligent building block

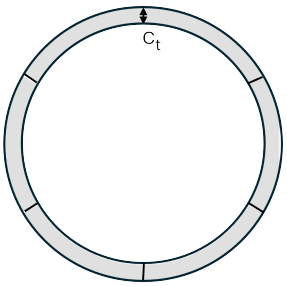

(b) Cylinder thickness indicated in the crossection

Figure 5.15: Parameters found in the geometry of the SMP cylinder

Table 5.5: Parameter tuning design 4, with the values in bold representing the 'base' values.

B_h [mm]	B_w [mm]	R_S [-]	C_t [mm]
12.5	10	0.2	1.5
16.5	20	**0.4**	2.0
20.5	**30**	0.6	**2.5**
24.5	40	0.8	3.0
28.5	60	1.0	3.5

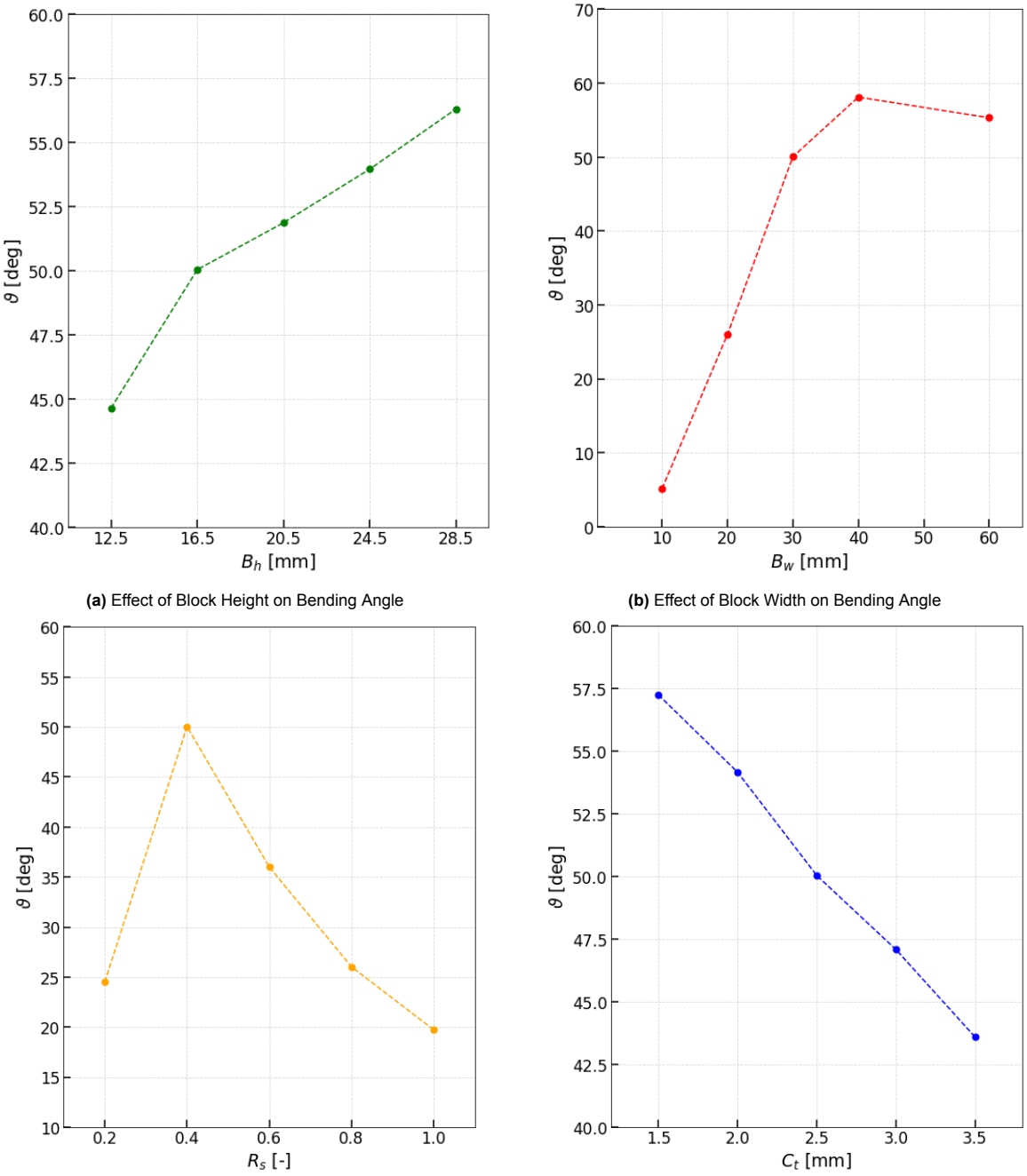

(a) Effect of Block Height on Bending Angle

(b) Effect of Block Width on Bending Angle

(c) Effect of segment ratio on Bending Angle

(d) Effect of Cylinder Thickness on Bending Angle

Figure 5.16: Effect of Geometric Parameters on the Bending Angle of the Cylinder

Table 5.6: Bending angles for five levels of the parameters: B_h, B_w, R_s and C_t

B_h [mm]	θ [deg]	B_w [mm]	θ [deg]	R_s [-]	θ [deg]	C_t [mm]	θ [deg]
12.5	44.6	10	5.14	0.2	24.5	1.5	57.3
16.5	50.0	20	26.0	0.4	50.0	2.0	54.2
20.5	51.9	30	50.0	0.6	36.0	2.5	50.0
24.5	54.0	40	58.1	0.8	26.0	3.0	47.1
28.5	56.3	60	55.3	1.0	19.7	3.5	43.6

Figure 5.16a: The bending angle increases linearly with the block height. Taller blocks enhance the distance between the upper and lower segments of the building block, providing more room for deformation. This increased flexibility allows the structure to achieve larger bending angles, making B_h a key parameter for maximizing the bending performance of the structure.

Figure 5.16b: The bending angle initially increases significantly with the block width, peaking around B_w = 40 mm before slightly decreasing or plateauing. This behaviour indicates an optimal width where the structure achieves maximum bending. Beyond this width, the top part of the structure starts to curl the opposite direction leading to a smaller bending angle with respect to the initial neutral axis of the cylinder.

Figure 5.16c: The segment ratio has a significant impact on the bending angle, which peaks at R_s = 0.4 and decreases as R_s approaches 1. The structure is too flexible and buckles excessively at R_s = 0.2, therefore enabling the structure not to function properly. This leads to a significant offset compared to R_s = 0.4. This suggests that an optimal ratio exists where the upper segment, S_1 is thinner relative to the lower segment (S_2), allowing for efficient buckling and deformation. As R_s approaches 1, the symmetry between the two segments reduces the structural asymmetry needed for effective bending. Adjusting R_s is therefore critical for optimizing the building block's performance.

Figure 5.16d: The bending angle decreases as the cylinder thickness increases. Thicker cylinders exhibit greater stiffness, which limits their ability to deform under applied loads. This result emphasizes the trade-off between structural strength and flexibility, with thinner cylinders being more effective for applications requiring larger bending angles.

The analysis of the building block parameters reveals that the bending angle is highly influenced by the four parameters. Taller blocks B_h consistently enhance bending with an optimal value at 28.5 mm, while B_w exhibits an optimal value at 40 mm, balancing flexibility and structural rigidity. Thinner cylinders C_t allow greater deformation, emphasizing the trade-off between stiffness and flexibility. The segment ratio R_s shows a peak in performance at $R_s = 0.4$, where the asymmetry between the upper and lower segments maximizes bending efficiency. These findings highlight the importance of parameter optimization to achieve superior bending performance in shape-morphing structures.

5.5.1. Design of Experiments

Design of Experiments (DoE) is a systematic approach used to investigate the relationship between the geometric parameters of the block and the resulting bending angle. By analyzing these relationships, DoE identifies which geometric parameters have the most significant influence on the bending angle and determines how variations in these parameters impact the overall deformation [143]. Additionally, DoE provides a structured framework for identifying the optimal geometric parameter values required to achieve a desired bending angle, making it a valuable tool for optimizing the design and performance of shape-morphing structures.

In this research, DoE offers several key benefits. It enables a systematic exploration of how the block's geometric parameters influence the bending angle, identifying critical factors and their interactions. This approach reduces the number of simulations required, saving time and computational resources while providing detailed insights to refine the design. By efficiently optimizing the parameters, DoE ensures that the shape-morphing structure achieves the desired performance with enhanced precision and adaptability.

A factorial approach is chosen due to the number of factors only being 4. The independent variables being B_h, B_w, R_s and C_t. Working with two levels, high and low. This leads to the following options in Table 5.7. The levels here resulted in the highest and lowest bending angle for the specific parameter tested.

For k factors with n levels each, the total number of experiments in a full factorial design is n^k, requiring 16 simulations in this case. However, to gain a deeper understanding of the interaction between two parameters, a different approach is applied. This approach is particularly useful for capturing significant effects on the bending angle. For the first parameter, four options are available, while the second parameter has three options. This results in $4 \times 3 = 12$ possible combinations. However, since the interaction between parameters one and two is the same as that between parameters two and one, only

half of these combinations are needed. This reduces the number to six parameter pairs, each with four simulations. The design matrix for the two-factor combinations can be found in Table 5.8. This results in a total of 24 simulations, with an interaction analysis for each parameter pair presented below.

Table 5.7: Levels used of the parameters: B_h, B_w, R_s and C_t

Factors \ Levels	Low (-1)	High (+1)
B_h	12.5	28.5
B_w	10	40
R_s	0.4	1.0
C_t	1.0	3.5

Table 5.8: The design matrix for two factors with two levels.

Factor 1	Factor 2
-1	-1
-1	1
1	-1
1	-1

Interaction between parameters occurs when the effect of one parameter (factor) on the response (output) depends on the level of another parameter. This means that the combined influence of two or more factors is not simply additive but rather depends on their interplay, leading to a non-linear or unexpected effect on the response. For example, one parameter may increase the bending angle when another parameter is at a low level, but decrease it when the other parameter is at a high level. When there is no interaction, the effect of one parameter remains constant regardless of the level of another parameter. In contrast, when there is an interaction, changing the level of one parameter alters how the other parameter influences the response. This complexity makes interactions a crucial aspect of study in DoE.

Interactions can be visualized through various types of graphs. One common tool is the interaction plot, which displays the response on the y-axis and one factor on the x-axis, with separate lines representing different levels of the second factor. If the lines are parallel, it indicates no interaction, as the effect of one factor is independent of the other. However, if the lines cross or diverge, this shows an interaction, meaning that the effect of one-factor changes depending on the level of the other.

Figure 5.17 illustrates how B_w affects the bending angle with B_h as a secondary factor. Increasing B_w leads to a significant rise in the bending angle for both levels of B_h. However, the increase is similar for both levels of B_w. The lines seem parallel, which indicates no interaction. However, looking at Table 5.9 the increase of the bending angle is slightly higher at a lower level B_h. This means that there is a minor interaction between these factors, and B_w has more effect on a lower B_h than at higher values.

Table 5.9: Design of Experiments of B_w and B_h

B_w [mm]	B_h [mm]	θ [deg]
10	12.5	4.69
10	28.5	10.7
40	12.5	55.9
40	28.5	60.0

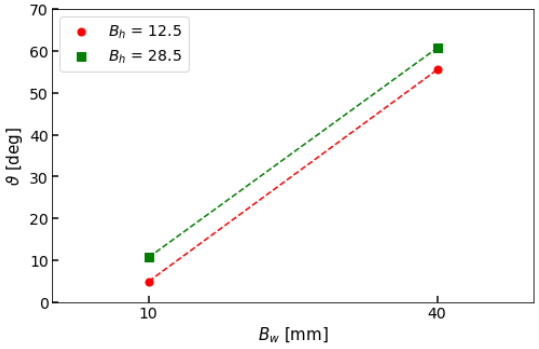

Figure 5.17: Interaction plot showing the effect of the block width B_w on θ, with B_h as the secondary variable

Figure 5.18 shows C_t and R_s affect the bending angle. Similar to Figure 5.17 the plots show two parallel lines. However, looking more closely at data in Table 5.10 a minor difference is found in these lines. At a lower segment ratio ($R_s = 0.4$), increasing C_t from 1.5 mm to 3.5 mm reduces the bending angle from 57.3 to 43.6 degrees, which is a difference of 13.7 degrees. For a higher segment ratio ($R_s = 1.0$), the reduction in bending angle is 14.3 degrees, dropping from 29.2 to 14.9 degrees as C_t increases.

The results indicate an interaction between C_t and R_s, where thicker cylinders amplify the negative effect of higher R_s on bending performance. This suggests that thinner cylinders are better suited for configurations with higher segment ratios to maximise deformation.

Table 5.10: Design of Experiments of C_t and R_s

C_t [mm]	R_s [-]	θ [deg]
1.5	0.4	57.3
1.5	1.0	29.2
3.5	0.4	43.6
3.5	1.0	14.9

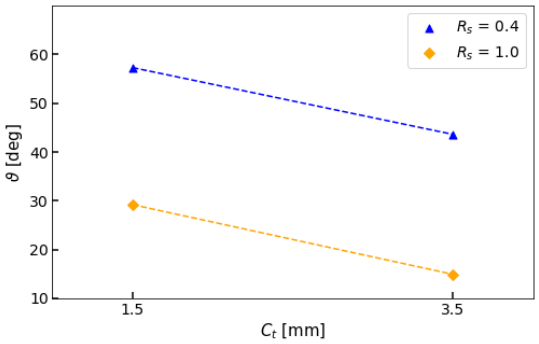

Figure 5.18: Interaction plot showing the effect of C_t on θ), with R_s as the secondary variable

Figure 5.19 explores the relationship between R_s and B_h on the bending angle. The lines are diverging indicating that interaction is present. At a lower block height ($B_h = 12.5$ mm), increasing R_s from 0.4 to 1.0 significantly reduces the bending angle. At a higher block height ($B_h = 28.5$ mm), increasing R_s also reduces the bending angle, but the reduction is less pronounced. These results show a strong interaction between R_s and B_h. Taller blocks mitigate the negative effects of increasing R_s, making them more robust to changes in segment ratio.

Table 5.11: Design of Experiments of R_s and B_h

R_s [-]	B_h [mm]	θ [deg]
0.4	12.5	44.6
0.4	28.5	56.3
1.0	12.5	4.10
1.0	28.5	28.1

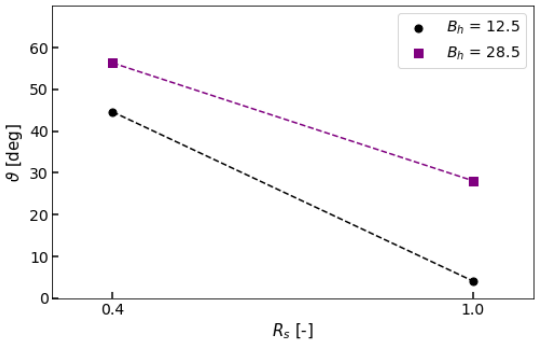

Figure 5.19: Interaction plot showing the effect of R_s on θ, with B_h as the secondary variable

Figure 5.20 shows the effect of R_s on the bending angle at two B_w levels. For $B_w = 40$ mm, the bending angle decreases significantly as R_s increases, whereas for $B_w = 10$ mm, the bending angle remains nearly constant regardless of R_s. The highly non-parallel lines highlight a strong interaction between R_s and B_w. This indicates that wider blocks are far more dependent on changes in segment ratio to achieve deformation, whereas narrower blocks are less affected by R_s. This suggests that B_w plays a dominant role in influencing how R_s affects bending.

Table 5.12: Design of Experiments of R_s and B_w

R_s [-]	B_w [mm]	θ [deg]
0.4	10	5.14
0.4	40	3.75
1.0	10	58.1
1.0	40	17.9

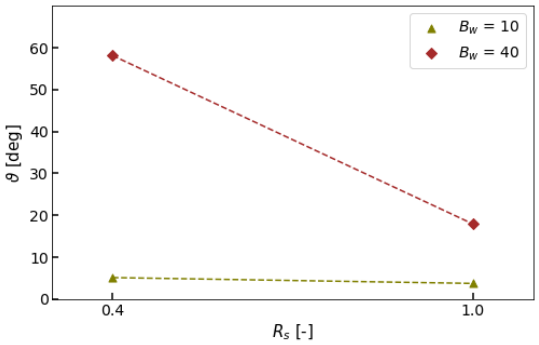

Figure 5.20: Interaction plot showing the effect of R_s on θ, with B_w as the secondary variable

Figure 5.21 shows the effect of C_t on the bending angle at two B_h levels. The interaction plot shows that for $B_h = 12.5$ mm, increasing C_t reduces the bending angle significantly from 53.7 degrees to 37.2 degrees. Conversely, for $B_h = 28.5$ mm, increasing C_t increases the bending angle slightly, from 43.3 degrees to 47.8 degrees. This behaviour indicates that the effect of C_t on the bending angle is highly dependent on the value of B_h. For smaller block heights ($B_h = 12.5$ mm), increasing C_t adds stiffness, reducing the bending angle. For larger block heights ($B_h = 28.5$ mm), the increase in C_t leads to improved structural integrity, resulting in a slight increase in the bending angle. The crossing lines in the interaction plot suggest a strong interaction between C_t and B_h.

Table 5.13: Design of Experiments of C_t and B_h

C_t [-]	B_h [mm]	θ [deg]
1.5	12.5	53.7
1.5	28.5	43.3
3.5	12.5	37.2
3.5	28.5	47.8

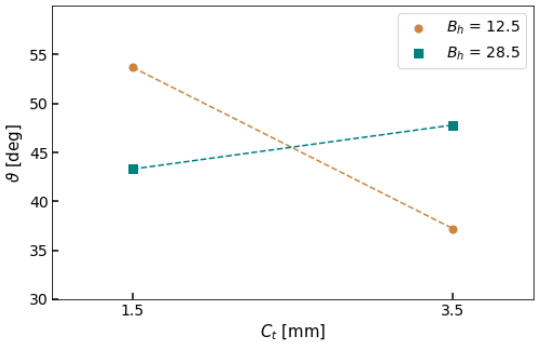

Figure 5.21: Interaction plot showing the effect of C_t on the bending angle θ, with B_h as the secondary variable

Figure 5.22 reveals that for $C_t = 1.5$ mm, increasing B_w significantly increases the bending angle from 13.8 degrees to 57.9 degrees. For $C_t = 3.5$ mm, a similar trend is observed, with the bending angle increasing from 4.76 degrees to 56.2 degrees. However, the increase is less at a higher C_t. This trend indicates that increasing B_w consistently improves the bending angle for both values of C_t, as wider blocks provide better flexibility and bending potential. However, the rate of increase is lower for $C_t = 3.5$ mm, suggesting that higher cylinder thickness reduces the sensitivity of the bending angle to changes in block width. The crossing lines in the interaction plot indicate a weak interaction between B_w and C_t, as the effect of B_w on the bending angle increased with a higher C_t value.

Table 5.14: Design of Experiments of B_w and C_t

B_w [-]	C_t [mm]	θ [deg]
10	1.5	13.8
10	3.5	4.76
40	1.5	57.9
40	3.5	56.2

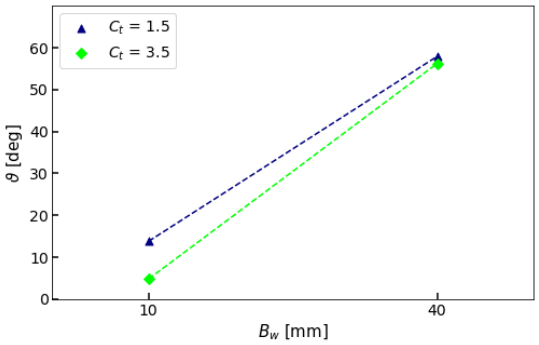

Figure 5.22: Interaction plot showing the effect of B_w on θ, with C_t as the secondary variable

The analysis reveals key trends and interactions between the parameters affecting bending performance. B_w and B_h positively influence θ, with wider and taller blocks producing greater deformations. However, B_w becomes less effective at higher B_h, indicating a non-linear interaction. R_s inversely affects θ, with higher R_s reducing bending performance, a trend amplified by C_t and B_w. Thicker cylinders and wider blocks increase the negative effects of R_s, emphasising the importance of parameter interactions in optimising shape-morphing designs. The interaction between C_t and B_h highlights the importance of considering both parameters together, as their combined effect on the bending angle is non-linear and interdependent. In contrast, for B_w and C_t, the bending angle is primarily influenced by B_w, with C_t acting as a secondary factor that moderates the rate of change. A maximum bending angle of 60.0 degrees was found with a cylinder with B_w = 40 mm and B_h = 28.mm.

5.5.2. Orientation angle cylinder

The cylinder is constructed from multiple building blocks, stacked both vertically and horizontally. The central region of each building block is most prone to buckling, as the distance between the lower and upper segments is greatest at this point. Consequently, if bending occurs precisely at the centre of a building block, the maximum bending angle can be achieved. However, if the central axis of a building block is not perfectly aligned with the bending direction, the impact on the bending angle needs to be assessed.

To investigate this, a new parameter, the orientation angle (ψ), is introduced. This angle is defined as the offset between the centerline of the two actuated SMA springs and the midpoint of the building block. The concept is illustrated in Figure 5.23. Given that the geometry of the building block significantly influences the bending performance, it is critical to test the orientation angle on a configuration that maximizes the effect of this parameter. The block width (B_w) plays a key role here, as a larger B_w provides greater structural stability and amplifies the impact of misalignment on the bending angle.

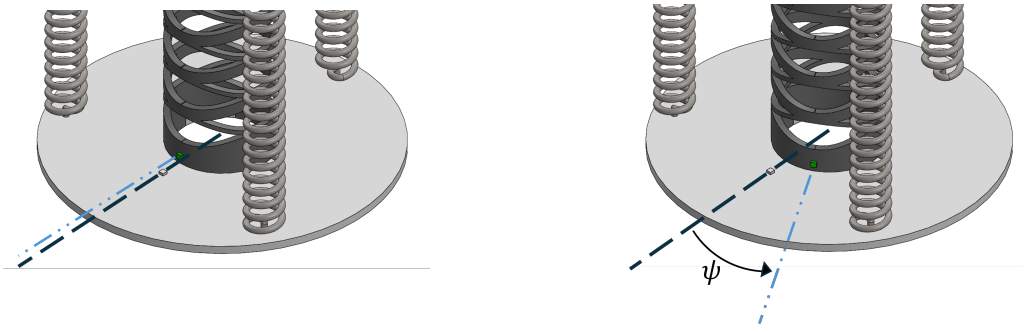

(a) Model with $\psi = 0$ deg.

(b) Model with $\psi = 45$ deg.

Figure 5.23: Indication of the orientation angle of the SMP model.

In this study, the maximum value tested for B_w is 60 mm. Therefore, the cylinder with B_w = 60 mm is

selected for the orientation angle analysis. The range of orientation angles to be explored varies from 0 to 180 degrees, as the geometry is symmetrical after 180 degrees. Key angles for evaluation include 0 degrees (the initial state), 45 degrees, 90 degrees (where the centreline falls between two building blocks), 135 degrees, and 180 degrees. This approach ensures that critical orientations are analysed, providing a comprehensive understanding of how alignment affects the bending angle.

The orientation of the cylinder relative to the bending direction has a minor influence on the bending angle, as shown in Figure 5.24a. As anticipated, the curve exhibits a “V” shape due to the symmetry of the cylinder. The minimum bending angle occurs when the cylinder is rotated by 90 degrees, which aligns with the orientation perpendicular to the bending direction. The difference between the bending angle of the beginning and the bending angle for each orientation angle has been plotted as a percentage in Figure 5.24b. The maximum deviation can be found in the middle at the orientation angle of 90 degrees, with a 0.24% difference compared to the initial orientation. Therefore, it can be stated that the orientation angle has a negligible influence on the bending angle.

Table 5.15: Bending angles and relative angle changes expressed in percentages at different orientation angles.

ψ [deg]	θ [deg]	Δ% [-]
0	55.44	0.00
45	55.39	0.08
90	55.31	0.24
135	55.37	0.13
180	55.41	0.06

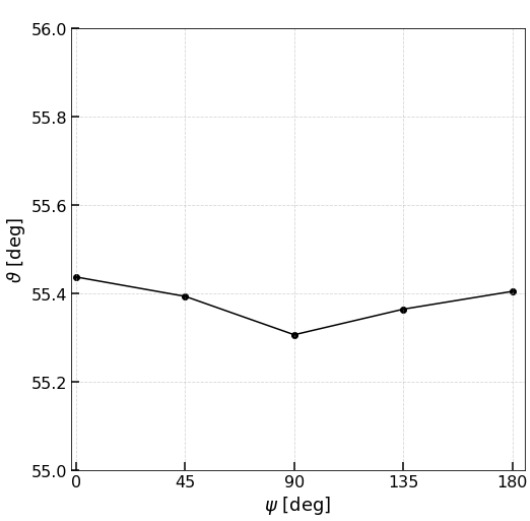

(a) Bending angle plotted for orientation angles: 0, 45, 90, 135 and 180 degrees.

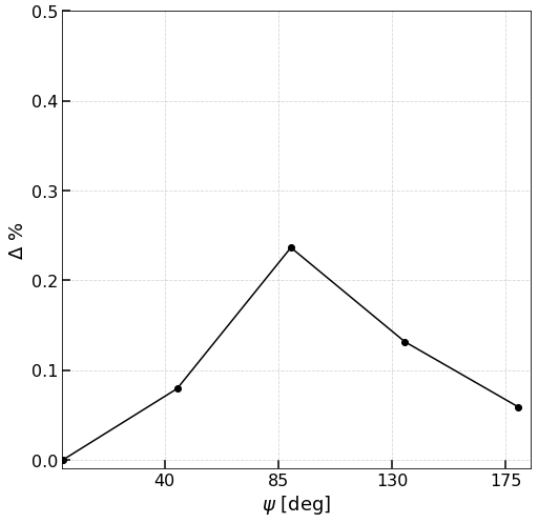

(b) Relative bending angle difference compared to initial orientation expressed as percentage.

Figure 5.24: Effect of orientation angle on bending angle simulated with the $B_w = 60$ mm geometry.

The difference between the bending angle of the beginning and the bending angle for each orientation angle has been plotted as a percentage in Figure 5.24b. The maximum deviation can be found in the middle at the orientation angle of 90 degrees, with a 0.24% difference compared to the initial orientation. Therefore, it can be stated that the orientation angle has a negligible influence on the bending angle. The negligible impact of the orientation angle on the bending angle, even at the maximum deviation of 0.24%, suggests that slight misalignments in cylinder orientation are acceptable. For instance, when actuating in different directions, if the cylinder is slightly tilted and not perfectly aligned, the resulting decrease in bending angle is small enough to be considered negligible. This provides greater flexibility in practical applications, where perfect alignment may not always be achievable.

5.6. Other Geometry

To explore the impact of geometry on bending performance, alternative configurations to the building block within the cylinder are tested. Basic geometric shapes, including hexagons, circles, ellipses, and squares, are evaluated as potential replacements for the building block, each of these can be found in Figure C.5. Each geometry is incorporated into the cylinder structure, and its bending behaviour is analysed under identical temperature and boundary conditions. The resulting bending angles are compared to determine how the shape and inherent structural properties of these basic geometries influence the overall performance. It is important to mention that the general width and height are kept the same as the building block to make it easier to compare, with the exception of the circle and square pattern, these have the same height as the building block. This comparative analysis aims to identify geometries that optimize bending efficiency while maintaining structural integrity and simplicity. The resulting bending angles of these different unit geometries can be found in Table 5.16 and Figure 5.25.

Table 5.16: Bending angles for different repeated structures ranked from lowest to highest.

Geometry	θ [deg]
Regular	0.97
Square	4.46
Circle	17.2
Hex	17.9
Building block	50.0
Diamond	52.6
Ellipse	52.7

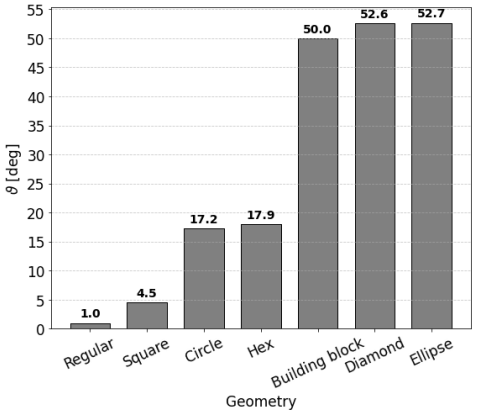

Figure 5.25: Bending angles plotted for different repeated structures ranked from lowest to highest.

In addition to the bending angles, the displacements in the Y and Z directions have been plotted for each geometry in Figure 5.26. It can be seen that there is a linear relationship between these two displacements, indicating that the bending is pure in the plane (ZY) and that the vertical displacement goes hand in hand with the horizontal displacement for each of the geometry.

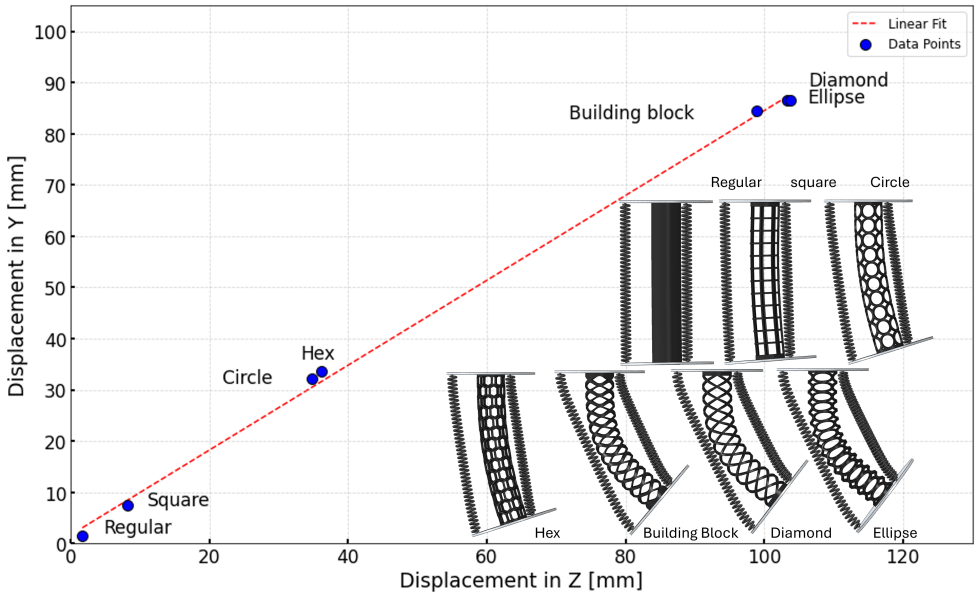

Figure 5.26: The Z displacement plotted against the Y displacement for the different geometries

For visual comparison, the standard building block structure has been added in Figure 5.26. Enlarged figures can be found in the appendix in section C.3.

A cylinder with no internal geometry deforms uniformly but lacks the ability to focus bending at specific points. The absence of internal patterns results in less precise control over deformation and reduces overall bending efficiency. Without internal structures, the design does not capitalize on the targeted buckling features seen in the building block. This makes it less effective in applications requiring controlled and efficient shape-morphing.

The square geometry shown generates stress concentrations at the corners during deformation, resulting in sharp bending at these points. Compared to the building block, which ensures smooth and controlled deformation through sinusoidal wave patterns, the square geometry is less adaptable and versatile, even with a wider aspect ratio. Additionally, the vertical bars act as stiffeners, making the structure harder to deform, while the horizontal grid structure holds the vertical bars in place, further restricting the structure's ability to bend.

The circular geometry deforms uniformly with evenly distributed stress, preventing localized fatigue. However, this reduces localized buckling capabilities, leading to smaller bending angles or less targeted deformation. The aspect ratio of the geometry also plays a role, wider circular patterns bend more due to increased flexibility, as seen with the ellipse geometry. Unlike the building block, the circular geometry lacks the asymmetry needed for precise morphing, making it more suitable for isotropic deformation applications.

The hexagonal geometry is characterized by its geometric stiffness and efficient load distribution, making it highly resistant to buckling. Deformation in this design is minimal, as the hexagonal cells inherently resist bending due to their stable geometry. While this structure is excellent for maintaining structural integrity, it compromises on flexibility and deformation efficiency. In contrast, the building block design prioritizes flexibility and controlled buckling, making it better suited for applications requiring significant shape changes.

The diamond geometry introduces anisotropy, creating stress concentrations along the sharp edges and vertices during deformation. This design facilitates bending but increases the risk of localized fatigue or material failure over repeated cycles. A wider aspect ratio within the diamond geometry enhances its ability to bend as the increased width provides more flexibility and reduces overall stiffness. Compared to the building block, which leverages asymmetry for controlled deformation, the diamond geometry is less durable and less adaptable for multi-directional bending.

The elliptical geometry provides directional flexibility, with deformation favouring the longer axis of the ellipses. A wider geometry further enhances its bending performance, as the increased aspect ratio allows for greater deformation along the longer axis. However, this directional flexibility sacrifices adaptability in other orientations. While this makes the elliptical geometry useful for focused directional motion, it limits its versatility. Compared to the building block, which supports multi-directional deformation, the elliptical geometry is less effective in scenarios requiring adaptability across multiple axes.

Overall, the building block design remains the most effective for achieving controlled and efficient deformation, since the maximum bending angle found was determined to be 60.0 degrees in the DoE section. Its engineered asymmetry and sinusoidal patterns enable localized buckling and smooth shape changes, making it highly versatile for shape-morphing applications. The aspect ratio of the geometries plays a significant role across all designs: wider geometries are more inclined to bend due to reduced stiffness and increased flexibility. Similarly, elliptical and diamond geometries show directional flexibility that improves with width but remains less adaptable for multi-directional deformation. The absence of internal geometries reduces deformation control, while square geometries exhibit abrupt bending with limited stress distribution, even when wider. Each configuration offers unique advantages and limitations, but the building block's balance of flexibility, stability, and control makes it the most optimal design for applications requiring complex shape morphing.

5.7. Potential applications

The potential applications of these cylinder structures extend far beyond single-direction bending. By combining multiple cylinders in series, it is possible to create highly adaptable actuation systems capable of multi-directional bending. Each cylinder within the system contributes to bending along a distinct axis. For instance, one cylinder may enable bending in the vertical plane, while another allows bending in the horizontal plane. This modular approach enables precise and programmable motion profiles, making it ideal for applications in (soft) robotics and adaptive mechanisms. By implementing cylinders with varying geometries or integrating actuated SMA springs, such structures can achieve both controlled and versatile deformation behaviours.

The dual-cylinder configuration in Figure 5.27 provides bending in two distinct directions, making it ideal for applications that require planar or bi-directional motion. By orienting the cylinders at specific angles, the setup can achieve controlled deformation in orthogonal directions. This design is particularly suited for simpler tasks, such as gripping or flexing, where adaptability along two axes is sufficient. The displacement path is marked by black dots, with a 1:1 scale on the Y and Z axes in Figure 5.27b. Several aspects can be examined, including the maximum displacement achieved, the curvature of the structure, and the relative motion of different segments.

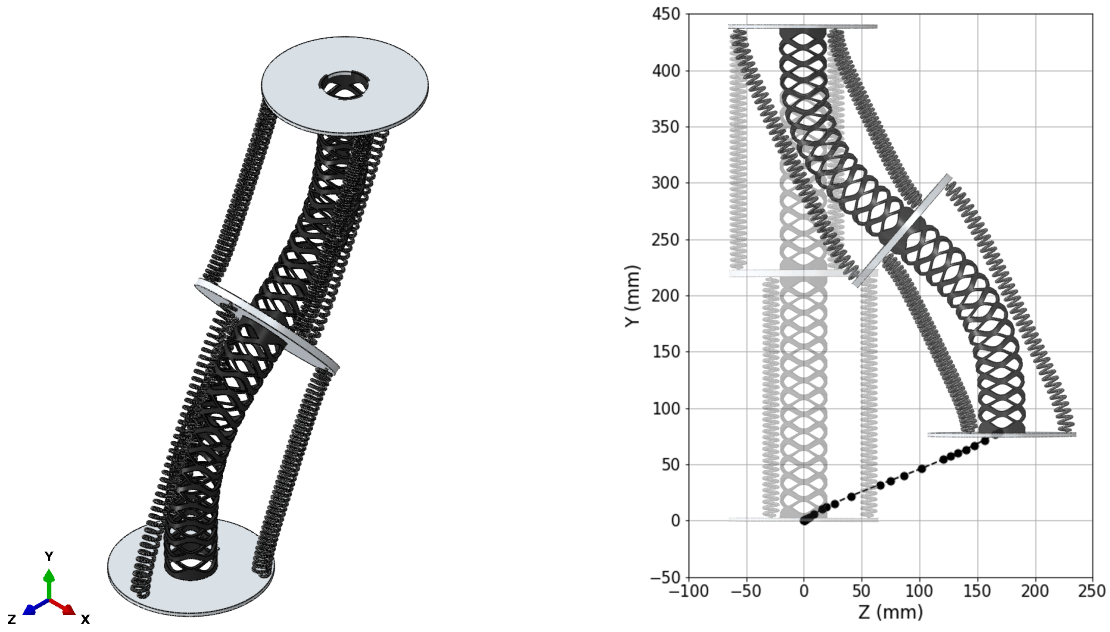

(a) Isometric view of the deformed state of the configuration.

(b) Deformed state of the dual structure overlaid with the displacement path (black dots) in the YZ plane and initial state (transparent).

Figure 5.27: The double cylinder configuration with opposite bending behaviour.

Incorporating a second cylinder that bends out of the plane, perpendicular to the initial cylinder significantly enhances the overall functionality and versatility of the system. This configuration introduces a new degree of freedom, enabling 3D shape-morphing capabilities and multi-axial deformation. By aligning the second cylinder to bend along an axis orthogonal to the first, the structure can achieve complex, multi-directional motion patterns that are not possible with a single-plane design as can be seen in Figure 5.28.

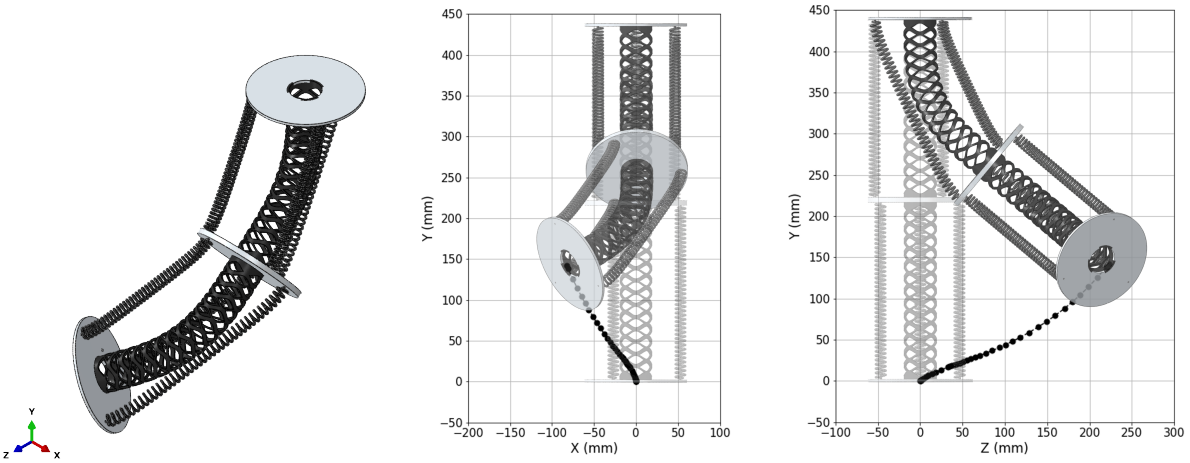

(a) Isometric view of the deformed state of the configuration with lower bending in the minus x direction.

(b) Deformed state of the structure overlaid with the displacement path in the YX plane and initial state (transparent).

(c) Deformed state of the structure overlaid with the displacement path in the YZ plane and initial state (transparent).

Figure 5.28: The double cylinder configuration with perpendicular bending behaviour.

Moreover, stacking cylinders in series provides a way to expand bending capabilities and create complex multi-dimensional motion. The modular nature of these designs allows for customization based on specific application needs, such as adaptive robotic arms or biomedical devices requiring intricate movements. This concept is more realistic, looking at the triple-cylinder in Figure 5.29.

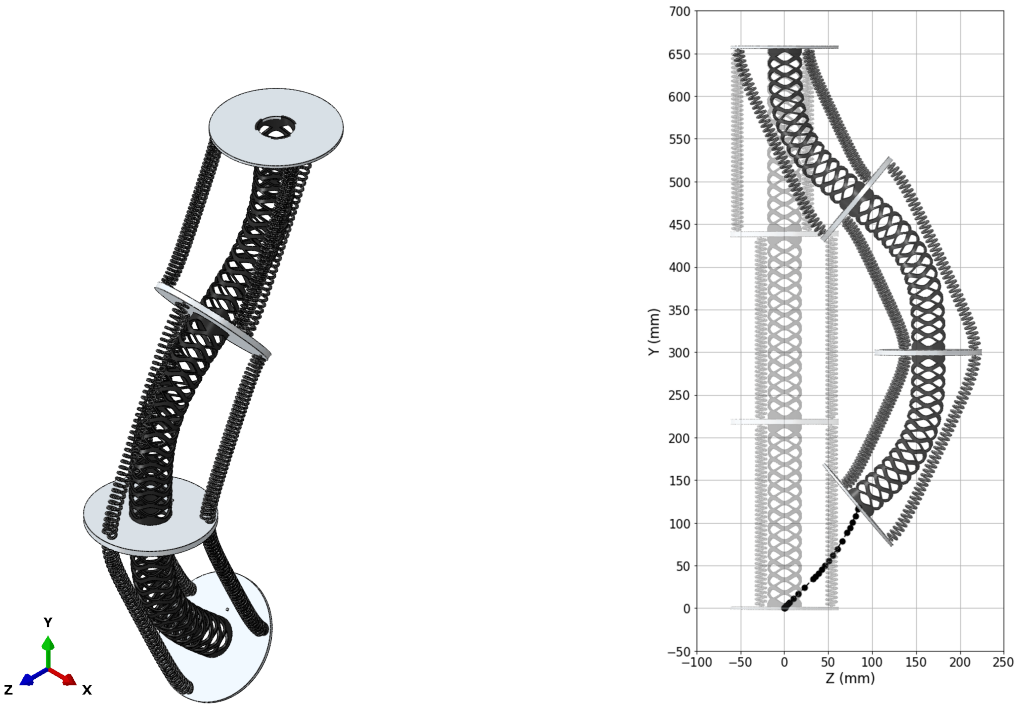

(a) Isometric view of the deformed state of the configuration with double bending found.

(b) Deformed state of the triple structure overlaid with the displacement path (black dots) in the YZ plane and initial state (transparent).

Figure 5.29: The triple-cylinder configuration with bending in two directions.

5.8. Conclusion

This chapter explored the development of shape-morphing structures using SMPs and SMAs, with a focus on understanding their material characteristics. Addressing the subquestion, "**How can multiple smart materials be integrated into the shape-morphing structure with multiple functionalities?**", several designs were proposed to enable efficient shape-morphing, culminating in the application of the intelligent building block within a cylinder geometry for the SMP. Material properties were analysed to identify key parameters for the constitutive equations, which were then formulated and implemented in Abaqus to model the thermo-mechanical behaviour of both materials. These simulations provided insights into their response under various loading and thermal conditions, enabling the evaluation of designs to maximise bending performance.

Key geometric parameters, such as B_w, B_h, R_s, and C_t, were systematically tuned to optimise structural performance. Taller and wider blocks were shown to increase the bending angle, while higher segment ratios and thicker cylinders reduced it. Using a DoE and a fractional factorial design, it was confirmed that interaction exists between these parameters. Additionally, the orientation of the cylinder relative to the actuation direction was studied, revealing that misalignment has only a minor impact on bending efficiency. Basic geometries, including square, circular, elliptical, and hexagonal shapes, were also tested as potential alternatives to the building block. However, the building block design remained the most effective for achieving controlled and efficient deformation, with a maximum θ of 60.0 degrees. Multi-cylinder setups were further explored, demonstrating how combined actuation can enable complex, multi-directional morphing.

The integration of SMPs and SMAs, along with an in-depth understanding of their material properties and optimised geometries, highlights the versatility of these systems for precise and adaptable shape morphing. With this, the study is concluded, and recommendations will be presented in the next chapter.

6

Conclusion and recommendations

6.1. Conclusion

This study set out to design shape-morphing structures using smart materials such as hydrogels, SMPS and SMAs to develop mechanically intelligent systems with potential applications in soft robotics. This objective was embodied by the research question "***How can smart materials be used to develop a shape-morphing structure applied into soft actuators?***" This question is answered by means of the following sub-questions.

What types of smart materials are appropriate to use for a shape-morphing actuator?

Chapter 2 explored various smart materials for shape-morphing actuators, focusing on hydrogels, SMPs, and SMAs. These materials enable controlled and reversible deformations in response to stimuli such as temperature, moisture, light, or electric and magnetic fields. Hydrogels excel in volumetric expansion and compliance, making them ideal for soft actuators requiring hydration or thermal-driven shape changes. SMPs provide tunable stiffness and shape retention, holding deformed shapes until triggered to return to their original form. SMAs offer high force output and precise actuation through phase transitions, making them suitable for compact and powerful shape transformations. The selection of these materials depends on factors such as energy efficiency and mechanical properties, while their combination with tailored morphology enhances actuator performance in applications like soft robotics and adaptive structures.

How can a model-based design framework be implemented to model and predict the behaviour of structures with integrating smart materials?

This subquestion was answered in Chapter 2 and Chapter 3. FEA has been established as a reliable tool for modelling and predicting the behaviour of hydrogels, SMPs, and SMAs in shape-morphing actuators. By incorporating material properties, geometric configurations, boundary conditions, and constitutive equations, FEA enables accurate simulations of deformation behaviours and actuation performance. For hydrogels, FEA models volumetric expansion and compliance in response to temperature changes, aiding in actuator design. In SMPs, it simulates shape retention and recovery using viscoelastic and hyperelastic constitutive models, while for SMAs, it predicts phase transitions and force output through phase transformation equations. Implemented in Abaqus, these simulations integrate thermal cycling effects and boundary conditions to ensure realistic predictions. By optimizing parameters through DoE and analyzing configurations FEA has demonstrated how material placement and geometry influence morphing behaviour.

How can shape-morphing structures be developed by using smart materials?

This question was answered in Chapter 4 by developing a reference case using hydrogel and silicone spheres, where hydrogel expanded with decreasing temperature and silicone provided structural support, enabling controlled bending. This initial setup was further refined into more complex structures that facilitated bending in multiple orientations, ultimately leading to the design of a hydrogel-silicone

gripper suitable for actuator applications. Additionally, various morphing structures—such as flexible fingers, can structures, and surface grids—were explored, each exhibiting unique deformation characteristics. Flexible fingers proved effective for soft robotic gripping, while can structures highlighted the role of geometry in uniform deformation and stability. Key findings confirmed the scalability of hydrogel morphing, as consistent bending angles were maintained across configurations. The maximum expansion factor of 1.37 in diameter and 2.59 in volume at 275 K underscores the hydrogel's potential for large-scale deformation.

How can multiple smart materials be integrated into the shape-morphing structure with multiple functionalities?

This question was addressed in Chapter 5, where a cylinder design was developed for the SMP utilizing an intelligent building block that enables controlled deformation of the structure. The cylinder functions as the support which can deform at high temperatures while locking its geometry in a deformed state when cooling down. This design facilitates compression and bending of the structure through actuation exerted by SMA springs. The springs provide the force needed for the deformation and can vary from one to three spring actuation, depending on the desired output. The geometric parameters of this cylinder structure were analysed, and a Design of Experiments approach was used to explore the interactions between these parameters. Potential applications include assembling multiple cylinders in series to create an arm capable of functioning as an actuator.

The implications of these findings are significant for advancing the development of soft robotics, as they provide a foundation for creating systems that mimic natural movements and respond dynamically to external stimuli. This research culminated in a simulation that provides a novel actuator design as a basis for the working principle of soft grippers actuated with thermoresponsive spheres. Additionally, this study bridges the gap between theoretical principles and the practical application of shape-morphing materials in soft robotics. This resulted in a multi-cylinder structure which could be used as an arm in an actuator design. This study provides a comprehensive understanding of integrating SMPs, SMAs, and hydrogels into adaptive structures, ranging from material properties to actuation mechanisms.

6.2. Recommendations

This study has provided valuable insights into the development of shape-morphing structures using hydrogels, SMPs and SMAs. Building on these findings, several recommendations can be made to enhance the understanding and practical implementation of these materials.

- **Exploring Alternative Material Types:** Investigating different smart materials could expand the range of achievable deformations and responses. While this research primarily focused on PNIPAM hydrogels, exploring alternative hydrogels with improved thermal responsiveness, expansion rates, or bending capabilities could yield better performance. Additionally, integrating multiple hydrogel types within a single configuration could enable varied bending behaviours without altering the number of particles. Similarly, identifying SMPs with greater stiffness reduction at high temperatures could result in more significant deformations and larger bending angles.
- **Enhancing Actuation Mechanisms:** Future designs should investigate improved actuation setups to achieve more controlled deformation. For example, an actuation system that dynamically regulates temperature across different materials could allow for independent and coordinated deformations within hybrid structures.
- **Expansion simulation:** The existing constitutive models for SMPs and SMAs offer a strong basis for predicting mechanical behaviour, further refinements are necessary to enhance accuracy, particularly in capturing time-dependent effects such as relaxation and creep. Incorporating environmental factors like humidity and strain rate dependency would improve their real-world applicability. Integrating external forces into simulations would further enhance the understanding of their influence on deformation performance, ensuring a more comprehensive and realistic assessment of actuator behaviour.

6.3. Future Work

In addition to the recommendations above, several areas warrant further investigation to expand the versatility and practical applications of shape-morphing structures.

- **Investigating Twisting Deformation:** Future research could explore the potential for torsional deformation by tilting the folding block at varying angles, as shown in Figure 6.2. While this study primarily focused on compression and bending, incorporating a three-spring actuation system instead of the current two-spring setup could allow for controlled twisting deformation, broadening the range of achievable morphing behaviours.
- **Integration of Hybrid Smart Material Systems:** Combining SMAs, SMPs, and hydrogels within a single actuator could lead to multi-functional, shape-morphing structures, as illustrated in Figure 6.1. Composite systems that leverage the force generation of SMAs, the adaptability of SMPs, and the swelling behaviour of hydrogels could enable large-scale deformations and precise control over transitions between configurations. However, addressing the conflicting thermal activation requirements—where PNIPAM hydrogels expand when cooled, while SMAs and SMPs require heating to actuate—remains a key challenge.
- **Experimental Validation:** While this study relied on simulations, experimental validation of the proposed designs remains a crucial step. Future work should focus on fabricating and testing prototypes to compare computational predictions with real-world behaviour. Further research should focus on physical prototyping and testing to compare experimental results with simulation predictions.

In summary, advancing shape-morphing structures requires further exploration of alternative materials, hybrid configurations, enhanced actuation strategies, and additional deformation modes such as twisting. These developments will support the integration of these systems into advanced technologies and practical applications.

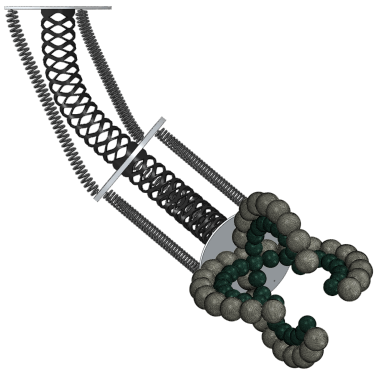

Figure 6.1: A potential integration of the two shape-morphing applications discussed in this study.

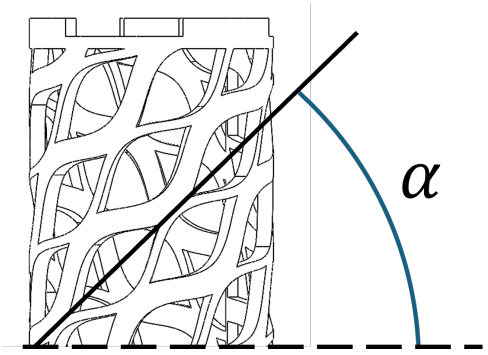

Figure 6.2: Inclination angle of the folding block indicated on the top part of the SMP cylinder.

References

[1] Hod Lipson. “Challenges and opportunities for design, simulation, and fabrication of soft robots”. In: *Soft Robotics* 1.1 (2014), pp. 21–27.

[2] Jianshu Zhou, Shu Chen, and Zheng Wang. “A Soft-Robotic Gripper With Enhanced Object Adaptation and Grasping Reliability”. In: *IEEE Robotics and Automation Letters* 2.4 (2017), pp. 2287–2293. DOI: 10.1109/LRA.2017.2716445.

[3] Burebi Yiming et al. “Mechanics-guided design of shape-morphing composite sheets with hard and soft materials”. In: *Extreme Mechanics Letters* 35 (2020), p. 100643.

[4] Jeff Jones. “Towards programmable smart materials: Dynamical reconfiguration of emergent transport networks”. In: *International Journal of Unconventional Computing* 7 (2011).

[5] Shashi Bahl et al. “Smart materials types, properties and applications: A review”. In: *Materials Today: Proceedings* 28 (2020). International Conference on Aspects of Materials Science and Engineering, pp. 1302–1306. ISSN: 2214-7853. DOI: https://doi.org/10.1016/j.matpr.2020.04.505.

[6] Kazuhiro Otsuka and Clarence Marvin Wayman. *Shape memory materials*. Cambridge university press, 1999.

[7] Junseong Ahn et al. “A Review of Recent Advances in Electrically Driven Polymer-Based Flexible Actuators: Smart Materials, Structures, and Their Applications”. In: *Advanced Materials Technologies* 7.11 (2022), p. 2200041. DOI: https://doi.org/10.1002/admt.202200041.

[8] Hussein M El-Husseiny et al. “Smart/stimuli-responsive hydrogels: Cutting-edge platforms for tissue engineering and other biomedical applications”. In: *Materials Today Bio* 13 (2022), p. 100186.

[9] Al Arsh Basheer. “Advances in the smart materials applications in the aerospace industries”. In: *Aircraft Engineering and Aerospace Technology* 92.7 (2020), pp. 1027–1035.

[10] Kenneth AW Hoffmann et al. “Bird-inspired robotics principles as a framework for developing smart aerospace materials”. In: *Journal of Composite Materials* (2023), p. 00219983231152663.

[11] Mohd Ammar et al. “Significant applications of smart materials and Internet of Things (IoT) in the automotive industry”. In: *Materials Today: Proceedings* 68 (2022), pp. 1542–1549.

[12] Abhilash Mukherjee, Prateek Srivastava, Jasminder Kaur Sandhu, et al. “Application of smart materials in civil engineering: a review”. In: *Materials Today: Proceedings* (2021).

[13] AYN Sofla et al. “Shape morphing of aircraft wing: Status and challenges”. In: *Materials & Design* 31.3 (2010), pp. 1284–1292.

[14] Yadong Yin and John A Rogers. *Introduction: smart materials*. 2022.

[15] Qianyi Chen, Tarish Kalpoe, and Jovana Jovanova. “Design of mechanically intelligent structures: Review of modeling stimuli-responsive materials for adaptive structures”. In: *Heliyon* (2024).

[16] Bohua Sun. “Smart materials and structures”. In: *South Africa: Cape Town: Cape Peninsula University of Technology Lecture at Swiss Federal Institute of Technology Zurich (ETH)* (2015).

[17] Nidhi Jain et al. “Smart materials–A state-of-the-art-review”. In: *Materials Today: Proceedings* (2023).

[18] İbrahim Nazem Qader et al. “A review of smart materials: researches and applications”. In: *El-Cezeri* 6.3 (2019), pp. 755–788.

[19] Peng Yang et al. “Stimuli-responsive polydopamine-based smart materials”. In: *Chemical Society Reviews* 50.14 (2021), pp. 8319–8343.

[20] Susmita Kamila. “Introduction, Classification and Applications of Smart Materials: An Overview”. In: *American Journal of Applied Sciences* 10 (July 2013), pp. 876–880. DOI: 10.3844/ajassp.2013.876.880. URL: https://thescipub.com/abstract/ajassp.2013.876.880.

[21] Ajit Behera and Ajit Behera. “Piezoelectric materials”. In: *Advanced Materials: An Introduction to Modern Materials Science* (2022), pp. 43–76.

[22] Yanfang Meng, Genqiang Chen, and Maoyong Huang. “Piezoelectric materials: Properties, advancements, and design strategies for high-temperature applications”. In: *Nanomaterials* 12.7 (2022), p. 1171.

[23] Christiaan Boerkamp, Tiago L Costa, and Jovana Jovanova. “Design of a Flexible Transducer Array and Characterisation of Piezoelectric Sensors for Curvature Compensation”. In: *Smart Materials, Adaptive Structures and Intelligent Systems*. Vol. 86274. American Society of Mechanical Engineers. 2022, V001T08A002.

[24] Hrishikesh Kulkarni et al. “Application of piezoelectric technology in automotive systems”. In: *Materials Today: Proceedings* 5.10 (2018), pp. 21299–21304.

[25] Huiru Shih et al. “Photostriction and its use in actuation of flexible structures”. In: *Journal of Engineering Technology* 25.1 (2008), p. 20.

[26] B Kundys. “Photostrictive materials”. In: *Applied Physics Reviews* 2.1 (2015).

[27] Mosfequr Rahman et al. “Experimental investigation of photostrictive materials for MEMS application”. In: *Open Access Library Journal* 4.11 (2017), p. 1.

[28] Shaoyu Zhao et al. “Opto-electro-thermo-mechanical behaviours of perovskite plates”. In: *International Journal of Mechanical Sciences* 267 (2024), p. 109016.

[29] Mohsen Shahinpoor. “Review of Electrostrictive Materials”. In: *Fundamentals of Smart Materials*. The Royal Society of Chemistry, Apr. 2020, pp. 36–45. ISBN: 978-1-78262-645-9. DOI: 10.1039/BK9781782626459-00036. URL: https://doi.org/10.1039/BK9781782626459-00036.

[30] Gabriele Bocchetta et al. “Performance of Smart Materials-Based Instrumentation for Force Measurements in Biomedical Applications: A Methodological Review”. In: *Actuators*. Vol. 12. Multidisciplinary Digital Publishing Institute. 2023, p. 261.

[31] Abdul-Ghani Olabi and Artur Grunwald. “Design and application of magnetostrictive materials”. In: *Materials & Design* 29.2 (2008), pp. 469–483.

[32] Zidong Liu et al. “High-Precision Position Tracking Control of Giant Magnetostrictive Actuators Using Fractional-Order Sliding Mode Control with Inverse Prandtl-Ishlinskii Compensator”. In: *International Journal of Precision Engineering and Manufacturing* 24.3 (2023), pp. 379–393.

[33] Ajit Behera and Ajit Behera. “Magnetostrictive materials”. In: *Advanced Materials: An Introduction to Modern Materials Science* (2022), pp. 127–156.

[34] Lidong Chen, Ruiheng Liu, and Xui Shi. *Thermoelectric materials and devices*. Elsevier, 2020.

[35] Madhubanti Mukherjee, Ashutosh Srivastava, and Abhishek K Singh. “Recent advances in designing thermoelectric materials”. In: *Journal of Materials Chemistry C* 10.35 (2022), pp. 12524–12555.

[36] Lei Yang et al. “High performance thermoelectric materials: progress and their applications”. In: *Advanced Energy Materials* 8.6 (2018), p. 1701797.

[37] Ahmed Esmail Shalan et al. “Advances in thermochromic and thermoelectric materials”. In: *Advanced Lightweight Multifunctional Materials*. Elsevier, 2021, pp. 153–186.

[38] Chang Gu et al. “Emerging electrochromic materials and devices for future displays”. In: *Chemical Reviews* 122.18 (2022), pp. 14679–14721.

[39] Junlong Niu et al. “Infrared electrochromic materials, devices and applications”. In: *Applied Materials Today* 24 (2021), p. 101073.

[40] He Tian and Junji Zhang. *Photochromic materials: preparation, properties and applications*. John Wiley & Sons, 2016.

[41] Masahiro Irie, Takahiro Seki, and Yasushi Yokoyama. *New frontiers in photochromism*. Springer, 2013.

[42] Thomas C Halsey. “Electrorheological fluids”. In: *Science* 258.5083 (1992), pp. 761–766.

[43] Vinod Chauhan, Ashwani Kumar, and Radhey Sham. “Magnetorheological fluids: A comprehensive review”. In: *Manufacturing Review* 11 (2024), p. 6.

[44] Qi Lu, Wen Jiao Han, and Hyoung Jin Choi. “Smart and functional conducting polymers: application to electrorheological fluids”. In: *Molecules* 23.11 (2018), p. 2854.

[45] Manjesh Kumar et al. “A review on rheological properties of magnetorheological fluid for engineering components polishing”. In: *Materials Today: Proceedings* 56 (2022), A6–A12.

[46] Baohua Zhang et al. “State-of-the-art robotic grippers, grasping and control strategies, as well as their applications in agricultural robots: A review”. In: *Computers and Electronics in Agriculture* 177 (2020), p. 105694. ISSN: 0168-1699. DOI: https://doi.org/10.1016/j.compag.2020.105694.

[47] Candy Löwenberg et al. “Shape-memory hydrogels: evolution of structural principles to enable shape switching of hydrophilic polymer networks”. In: *Accounts of chemical research* 50.4 (2017), pp. 723–732.

[48] Lei Li, Johannes M Scheiger, and Pavel A Levkin. “Design and applications of photoresponsive hydrogels”. In: *Advanced Materials* 31.26 (2019), p. 1807333.

[49] Taposhree Dutta et al. “Smart materials for flexible electronics and devices: hydrogel”. In: *RSC advances* 14.19 (2024), pp. 12984–13004.

[50] JL Zhang et al. “Thermo-/chemo-responsive shape memory/change effect in a hydrogel and its composites”. In: *Materials & Design* 53 (2014), pp. 1077–1088.

[51] Bin Xue et al. “Hydrogel tapes for fault-tolerant strong wet adhesion”. In: *Nature Communications* 12.1 (2021), p. 7156.

[52] Prabhpreet Kaur et al. “Hydrogels in agriculture: prospects and challenges”. In: *Journal of Polymers and the Environment* 31.9 (2023), pp. 3701–3718.

[53] Partha Sikdar et al. “Recent advances in the synthesis of smart hydrogels”. In: *Materials Advances* 2.14 (2021), pp. 4532–4573.

[54] Kazuhiro Ishida et al. “Synthesis and property of temperature-responsive hydrogel with movable cross-linking points”. In: *Macromolecules* 45.15 (2012), pp. 6136–6142.

[55] Shengqiang Cai and Zhigang Suo. “Mechanics and chemical thermodynamics of phase transition in temperature-sensitive hydrogels”. In: *Journal of the Mechanics and Physics of Solids* 59.11 (2011), pp. 2259–2278. ISSN: 0022-5096. DOI: https://doi.org/10.1016/j.jmps.2011.08.008.

[56] Bingren Tian and Jiayue Liu. “Smart stimuli-responsive chitosan hydrogel for drug delivery: A review”. In: *International Journal of Biological Macromolecules* 235 (2023), p. 123902.

[57] Yongping Liang, Jiahui He, and Baolin Guo. “Functional hydrogels as wound dressing to enhance wound healing”. In: *ACS nano* 15.8 (2021), pp. 12687–12722.

[58] Yunrui Chen et al. “Bioinspired hydrogel actuator for soft robotics: Opportunity and challenges”. In: *Nano Today* 49 (2023), p. 101764.

[59] Qianyi Chen, Dingena Schott, and Jovana Jovanova. “Model-based design of variable stiffness soft gripper actuated by smart hydrogels”. In: *Soft Robotics* (2024). DOI: https://doi.org/10.1089/soro.2023.0185.

[60] Muhammad Abdul Haq, Yunlan Su, and Dujin Wang. “Mechanical properties of PNIPAM based hydrogels: A review”. In: *Materials Science and Engineering: C* 70 (2017), pp. 842–855.

[61] Lin Tang et al. “Poly (N-isopropylacrylamide)-based smart hydrogels: Design, properties and applications”. In: *Progress in Materials Science* 115 (2021), p. 100702.

[62] Ahmad Majid Qazi et al. “The impact of smart materials, digital twins (DTs) and Internet of things (IoT) in an industry 4.0 integrated automation industry”. In: *Materials Today: Proceedings* 62 (2022). International Conference on Advances in Materials and Mechanical Engineering, pp. 18–25. ISSN: 2214-7853. DOI: https://doi.org/10.1016/j.matpr.2022.01.387.

[63] Iman Abavisani, Omid Rezaifar, and Ali Kheyroddin. “Multifunctional properties of shape memory materials in civil engineering applications: A state-of-the-art review”. In: *Journal of Building Engineering* 44 (2021), p. 102657.

[64] Jaronie Mohd Jani et al. “A review of shape memory alloy research, applications and opportunities”. In: *Materials & Design (1980-2015)* 56 (2014), pp. 1078–1113.

[65] Syed Abbas Raza et al. “Effect of Nano-Silica Volume Reinforcement on the Microstructure, Mechanical, Phase Distribution and Electrochemical Behavior of Pre-Alloyed Titanium-Nickel (Ti-Ni) Powder”. In: *Key Engineering Materials* 875 (2021), pp. 60–69.

[66] Aniello Riccio et al. “Shape memory alloys (SMA) for automotive applications and challenges”. In: *Shape Memory Alloy Engineering* (2021), pp. 785–808.

[67] Jung Woo Sohn et al. “Application of shape memory alloy actuators to vibration and motion control of structural systems: a review”. In: *Applied Sciences* 13.2 (2023), p. 995.

[68] Leszek Matuszewski. “Application of shape memory alloys in pipeline couplings for shipbuilding”. In: *Polish Maritime Research* 27.3 (2020), pp. 82–88.

[69] Andrea Spaggiari et al. “Smart materials: Properties, design and mechatronic applications”. In: *Proceedings of the institution of mechanical engineers, part l: journal of materials: design and applications* 233.4 (2019), pp. 734–762.

[70] CM Wayman. “Shape memory alloys”. In: *MRS bulletin* 18.4 (1993), pp. 49–56.

[71] Gautam Singh Rajput et al. “Areas of recent developments for shape memory alloy: A review”. In: *Materials Today: Proceedings* 62 (2022), pp. 7194–7198.

[72] M Balasubramanian et al. “Application of shape memory alloys in engineering–A review”. In: *Journal of Physics: Conference Series*. Vol. 2054. IOP Publishing. 2021, p. 012078.

[73] Liangliang Cao et al. “Surface structures, particles, and fibers of shape-memory polymers at micro-/nanoscale”. In: *Advances in Polymer Technology* 2020 (2020).

[74] Tarek Dayyoub et al. “Shape memory polymers as smart materials: A review”. In: *Polymers* 14.17 (2022), p. 3511.

[75] Yanju Liu et al. “Shape memory polymers and their composites in aerospace applications: a review”. In: *Smart materials and structures* 23.2 (2014), p. 023001.

[76] Hui Gao et al. “The research status and challenges of shape memory polymer-based flexible electronics”. In: *Materials Horizons* 6.5 (2019), pp. 931–944.

[77] Davood Rahmatabadi et al. “Shape memory performance assessment of FDM 3D printed PLA-TPU composites by Box-Behnken response surface methodology”. In: *The International Journal of Advanced Manufacturing Technology* 127.1 (2023), pp. 935–950.

[78] Yuliang Xia et al. “A review of shape memory polymers and composites: mechanisms, materials, and applications”. In: *Advanced materials* 33.6 (2021), p. 2000713.

[79] Gayla J Berg et al. “New directions in the chemistry of shape memory polymers”. In: *Polymer* 55.23 (2014), pp. 5849–5872.

[80] Tong Mu et al. “Shape memory polymers for composites”. In: *Composites Science and Technology* 160 (2018), pp. 169–198.

[81] Mohamed Ali Kouka et al. “4D printing of shape memory polymers, blends, and composites and their advanced applications: a comprehensive literature review”. In: *Advanced Engineering Materials* 25.4 (2023), p. 2200650.

[82] Farhang Momeni, Xun Liu, Jun Ni, et al. “A review of 4D printing”. In: *Materials & design* 122 (2017), pp. 42–79.

[83] Mohammad Aberoumand et al. “4D printing of polyvinyl chloride (PVC): a detailed analysis of microstructure, programming, and shape memory performance”. In: *Macromolecular Materials and Engineering* 308.7 (2023), p. 2200677.

[84] Reza Noroozi et al. “4D-printed shape memory polymer: Modeling and fabrication”. In: *Smart Materials in Additive Manufacturing, Volume 2: 4D Printing Mechanics, Modeling, and Advanced Engineering Applications*. Elsevier, 2022, pp. 195–228.

[85] Antreas Kantaros, Theodore Ganetsos, and Dimitrios Piromalis. “4D Printing: Technology Overview and Smart Materials Utilized”. In: *Kantaros, A., Ganetsos, T. & Piromalis, D.(2023). 4D Printing: Technology Overview and Smart Materials Utilized. Journal of Mechatronics and Robotics* 7.1 (2023), pp. 1–14.

[86] Christoph A Spiegel et al. “4D printing of shape memory polymers: from macro to micro”. In: *Advanced Functional Materials* 32.51 (2022), p. 2110580.

[87] Ayyaz Mahmood et al. “Revolutionizing manufacturing: A review of 4D printing materials, stimuli, and cutting-edge applications”. In: *Composites Part B: Engineering* (2023), p. 110952.

[88] Alan Lai et al. “Shape memory and superelastic ceramics at small scales”. In: *Science* 341.6153 (2013), pp. 1505–1508.

[89] Ehsan Moshkelgosha and Mahmood Mamivand. “Three-dimensional phase field modeling of fracture in shape memory ceramics”. In: *International Journal of Mechanical Sciences* 204 (2021), p. 106550.

[90] Mohsen Asle Zaeem, Ning Zhang, and Mahmood Mamivand. “A review of computational modeling techniques in study and design of shape memory ceramics”. In: *Computational Materials Science* 160 (2019), pp. 120–136.

[91] Flávia P Morais and Joana MR Curto. “Challenges in computational materials modelling and simulation: A case-study to predict tissue paper properties”. In: *Heliyon* 8.5 (2022).

[92] José Merodio and Ray W Ogden. *Constitutive modelling of solid continua*. Springer, 2020.

[93] Qian Guo et al. “Constitutive models for the structural analysis of composite materials for the finite element analysis: A review of recent practices”. In: *Composite Structures* 260 (2021), p. 113267.

[94] Frank L Matthews et al. *Finite element modelling of composite materials and structures*. Elsevier, 2000.

[95] William BJ Zimmerman. *Multiphysics modeling with finite element methods*. Vol. 18. World Scientific Publishing Company, 2006.

[96] Lovely Sabat and Chinmay Kumar Kundu. “History of finite element method: a review”. In: *Recent Developments in Sustainable Infrastructure: Select Proceedings of ICRDSI 2019* (2020), pp. 395–404.

[97] Johannes Reiner and Reza Vaziri. “8.4 Structural Analysis of Composites With Finite Element Codes: An Overview of Commonly Used Computational Methods”. In: *Comprehensive Composite Materials II*. Ed. by Peter W.R. Beaumont and Carl H. Zweben. Oxford: Elsevier, 2018, pp. 61–84. ISBN: 978-0-08-100534-7. DOI: https://doi.org/10.1016/B978-0-12-803581-8.10050-5. URL: https://www.sciencedirect.com/science/article/pii/B9780128035818100505.

[98] Paul M Kurowski. *Finite element analysis for design engineers*. SAE International, 2022.

[99] Z Gronostajski. “The constitutive equations for FEM analysis”. In: *Journal of Materials Processing Technology* 106.1-3 (2000), pp. 40–44.

[100] Andrea Saltelli et al. “Sensitivity analysis: A discipline coming of age”. In: *Environmental Modelling & Software* 146 (2021), p. 105226.

[101] Sergey Karabasov et al. “Multiscale modelling: approaches and challenges”. In: *Philosophical Transactions of the Royal Society A: Mathematical, Physical and Engineering Sciences* 372.2021 (2014), p. 20130390.

[102] Damien Tourret, Hong Liu, and Javier LLorca. “Phase-field modeling of microstructure evolution: Recent applications, perspectives and challenges”. In: *Progress in Materials Science* 123 (2022), p. 100810.

[103] Fan Xu and Hesheng Wang. “Soft robotics: Morphology and morphology-inspired motion strategy”. In: *IEEE/CAA Journal of Automatica Sinica* 8.9 (2021), pp. 1500–1522.

[104] Luquan Ren et al. “Biology and bioinspiration of soft robotics: Actuation, sensing, and system integration”. In: *Iscience* 24.9 (2021).

[105] Qianyi Chen, Dingena Schott, and Jovana Jovanova. “Model-based design of a mechanically intelligent shape-morphing structure”. In: *Scientific Reports* 14.1 (2024), p. 26148.

[106] Dohgyu Hwang et al. “Shape morphing mechanical metamaterials through reversible plasticity”. In: *Science robotics* 7.63 (2022), eabg2171.

[107] Nabila Tanjeem et al. “Shape-Changing Particles: From Materials Design and Mechanisms to Implementation”. In: *Advanced Materials* 34.3 (2022), p. 2105758.

[108] Francesco Fiorito et al. “Shape morphing solar shadings: A review”. In: *Renewable and Sustainable Energy Reviews* 55 (2016), pp. 863–884.

[109] Yanbin Li et al. “Shape-morphing materials and structures for energy-efficient building envelopes”. In: *Materials Today Energy* 22 (2021), p. 100874.

[110] Silvestro Barbarino et al. “A review of morphing aircraft”. In: *Journal of intelligent material systems and structures* 22.9 (2011), pp. 823–877.

[111] Hareesh Godaba et al. “A two-fingered robot gripper with variable stiffness flexure hinges based on shape morphing”. In: *2020 IEEE/RSJ International Conference on Intelligent Robots and Systems (IROS)*. IEEE. 2020, pp. 8716–8721.

[112] Dickson R Yao et al. “Multimodal Soft Robotic Actuation and Locomotion”. In: *Adv. Mater* 2308829 (2024).

[113] Qianyi Chen, Tarish Kalpoe, and Jovana Jovanova. “Modelling Programmable Deformation of Particle-Based Structure with Smart Hydrogels”. In: *2024 6th International Conference on Reconfigurable Mechanisms and Robots (ReMAR)*. IEEE. 2024, pp. 633–639.

[114] Maren Freutel et al. “Finite element modeling of soft tissues: material models, tissue interaction and challenges”. In: *Clinical Biomechanics* 29.4 (2014), pp. 363–372.

[115] Beomkeun Kim et al. “A comparison among Neo-Hookean model, Mooney-Rivlin model, and Ogden model for chloroprene rubber”. In: *International Journal of Precision Engineering and Manufacturing* 13 (2012), pp. 759–764.

[116] NA Neuburger and BE Eichinger. “Critical experimental test of the Flory-Rehner theory of swelling”. In: *Macromolecules* 21.10 (1988), pp. 3060–3070.

[117] Wei Hong, Zishun Liu, and Zhigang Suo. “Inhomogeneous swelling of a gel in equilibrium with a solvent and mechanical load”. In: *International Journal of Solids and Structures* 46.17 (2009), pp. 3282–3289.

[118] Zhiwei Ding et al. “A simplified coupled thermo-mechanical model for the transient analysis of temperature-sensitive hydrogels”. In: *Mechanics of Materials* 97 (2016), pp. 212–227.

[119] Daniela Rus and Michael T Tolley. “Design, fabrication and control of soft robots”. In: *Nature* 521.7553 (2015), pp. 467–475.

[120] Zisheng Liao et al. “On the stress recovery behaviour of Ecoflex silicone rubbers”. In: *International Journal of Mechanical Sciences* 206 (2021), p. 106624.

[121] Daniel Steck et al. “Mechanical responses of Ecoflex silicone rubber: Compressible and incompressible behaviors”. In: *Journal of Applied Polymer Science* 136.5 (2019), p. 47025.

[122] Siti Noor Azizzati Mohd Noor and Jamaluddin Mahmud. “Modelling and computation of silicone rubber deformation adapting neo-hookean constitutive equation”. In: *2015 Fifth International Conference on Communication Systems and Network Technologies*. IEEE. 2015, pp. 1323–1326.

[123] Florence G Downs et al. “Multi-responsive hydrogel structures from patterned droplet networks”. In: *Nature chemistry* 12.4 (2020), pp. 363–371.

[124] Wei Guo, Meie Li, and Jinxiong Zhou. “Modeling programmable deformation of self-folding all-polymer structures with temperature-sensitive hydrogels”. In: *Smart Materials and Structures* 22.11 (2013), p. 115028.

[125] AMT Composites. *Ecoflex 00-10*. Mar. 2006. URL: `https://www.amtcomposites.co.za/product/ecoflex-00-10-0-9kg/`.

[126] Luc Marechal et al. “Toward a common framework and database of materials for soft robotics”. In: *Soft robotics* 8.3 (2021), pp. 284–297.

[127] ABAQUS, Inc. *Element library: overview*. Mar. 2006. URL: https://classes.engineering.wustl.edu/2009/spring/mase5513/abaqus/docs/v6.6/books/usb/default.htm?startat=pt06ch21s01abo21.html.

[128] Dassault Systèmes. *Hybrid elements*. Feb. 2012. URL: http://130.149.89.49:2080/v6.12/books/gsk/default.htm?startat=ch04s01.html.

[129] Jixiang Qi et al. “Recent progress in active mechanical metamaterials and construction principles”. In: *Advanced Science* 9.1 (2022), p. 2102662.

[130] LC Brinson and MS Huang. “Simplifications and comparisons of shape memory alloy constitutive models”. In: *Journal of intelligent material systems and structures* 7.1 (1996), pp. 108–114.

[131] Vladimir Buljak and Gianluca Ranzi. *Constitutive Modeling of Engineering Materials: Theory, Computer Implementation, and Parameter Identification*. Academic Press, 2021.

[132] Numan Şarlı et al. “Magnetic properties of the martensitic transformations with twinned and detwinned”. In: *Physica B: Condensed Matter* 553 (2019), pp. 161–168.

[133] L Catherine Brinson. “One-dimensional constitutive behavior of shape memory alloys: thermomechanical derivation with non-constant material functions and redefined martensite internal variable”. In: *Journal of intelligent material systems and structures* 4.2 (1993), pp. 229–242.

[134] Cheikh Cisse, Wael Zaki, and Tarak Ben Zineb. “A review of constitutive models and modeling techniques for shape memory alloys”. In: *International Journal of Plasticity* 76 (2016), pp. 244–284.

[135] James G Boyd and Dimitris C Lagoudas. “A thermodynamical constitutive model for shape memory materials. Part I. The monolithic shape memory alloy”. In: *International journal of plasticity* 12.6 (1996), pp. 805–842.

[136] Norman Zalmon Shapiro and Lloyd S Shapley. “Mass action laws and the Gibbs free energy function”. In: *Journal of the Society for Industrial and Applied Mathematics* 13.2 (1965), pp. 353–375.

[137] Janice J Song, Huntley H Chang, and Hani E Naguib. “Design and characterization of biocompatible shape memory polymer (SMP) blend foams with a dynamic porous structure”. In: *Polymer* 56 (2015), pp. 82–92.

[138] AYN Sofla, DM Elzey, and HNG Wadley. “Two-way antagonistic shape actuation based on the one-way shape memory effect”. In: *Journal of Intelligent Material Systems and Structures* 19.9 (2008), pp. 1017–1027.

[139] Pinar Boyraz, Gundula Runge, and Annika Raatz. “An overview of novel actuators for soft robotics”. In: *Actuators*. Vol. 7. 3. MDPI. 2018, p. 48.

[140] Ran Tao et al. “4D printed multi-stable metamaterials with mechanically tunable performance”. In: *Composite Structures* 252 (2020), p. 112663.

[141] Eshwar Pawar. “A review article on acrylic PMMA”. In: *IOSR J. Mech. Civ. Eng* 13.2 (2016), pp. 1–4.

[142] Amir Hosein Sakhaei, Saeed Akbar, and Qi Ge. “Finite element simulation of 3d-printed sma-smp composite actuators”. In: *14th WCCM-ECCOMAS Congress 2020*. Vol. 1000. scipedia. 2021.

[143] Jiju Antony. *Design of experiments for engineers and scientists*. Elsevier, 2023.

A

Scientific paper

This appendix consists of the Scientific Research Paper, starting on the next page.

Smart Morphing Structure based on SMA and SMP for Soft Robotics

Abstract

Soft actuators utilizing shape memory materials have garnered significant attention for their adaptability and tunable properties, with compliant morphing structures playing a key role in enabling these actuators to achieve mechanical intelligence for soft robotics. However , structures made from a single shape memory material (SMM) struggle to achieve more complex deformation effects, particularly when load requirements are involved. Additionally, these structures tend to lack effective control strategies. This study introduces a novel actuator of SMA-SMP morphing structure with temperature control strategy. In the structure design, the SMA serves as the self-actuation driver, while the SMP cylinder functions as a switch, enabling the morphing structure to either maintain its current shape or continue deforming. The results indicate, experimental data verified with simulation results approve the feasibility of this approach, demonstrating fast, stable, and highly reproducible performance in temperature regulation, bending deformation, and stiffness modulation. The morphing structure can achieve a maximum bending angle of 65° with double-spring actuation and 42° with single-spring actuation within one cycle, with the ability to brake at any point. In addition, the stiffness can have a maximum 4.5 times increasement. Structure design is executed by performing a Design of Experiments.

Keywords-soft robotic, morphing structure, shape memory materials, thermal integration system, adaptive control

1 Introduction

Soft robots offer significant advantages over traditional rigid robots, excelling in flexibility, adaptability, and interaction with dynamic environments [1, 2]. Central to these capabilities are morphing structures, defined as systems that can change shape, stiffness, or geometry in response to environmental stimuli or through active control [3]. These structures are crucial for developing mechanically intelligent systems that enable self-actuation, a key feature for advanced soft robotic applications [4, 5]. Smart materials play a vital role in constructing morphing structures due to their responsiveness to stimuli such as temperature, magnetic fields, and pressure [6-8]. Realizing the full potential of these materials in morphing structures requires their integration with precise control systems, ensuring adaptive behavior. This synergy between mechanically intelligent morphing structures and effective control makes them a powerful solution for applications such as precision manufacturing [9], underwater exploration [10], and specialized gripping [11].

Shape memory materials are notable for their ability to remember and return to a pre-defined shape after undergoing significant deformation [12], when exposed to specific external stimuli. This unique property, observed in materials such as NiTi alloys and polylactic acid (PLA), has broad applications in industries including aerospace, automotive, and precision manufacturing [13]. Mechanistically, shape memory materials are categorized into two primary types: Shape Memory Alloys (SMAs) and Shape Memory Polymers (SMPs) [14]. SMAs are commonly used as soft actuators due to their relatively simple implementation, such as a bionic jellyfish robot is developed to produce contraction-recovery motion utilized SMA [15]. In addition, Kakubari et al. utilized strip-shaped SMA to control two silicone pillows,

developing an artificial sphincter based on this setup [16]. Yang and Wang introduced a flexible gripper design with multiple finger units powered by SMA wires and a shorter rod [17]. Borboni and Faglia created an SMA actuator using a slider and slot mechanism, where the SMA was directly heated via the Joule effect to perform its actions [18]. Although the kinematics and mechanical properties of SMA actuators can be measured and modeled during their transition to memory shapes, a major challenge remains: the limited number of stable states restricts their effectiveness as robotic actuators. SMPs have become widely used due to their low density and high biocompatibility. Lan et al. created a thermoset styrene-based SMP composite to construct a hinge mechanism for deploying a solar panel [19]. Son et al. designed an adhesive gripper with a bonding strength greater than two atmospheric pressures, using the reversible dry adhesion of an SMP-based actuator [20]. Liu et al. introduced a micro soft robot with four limbs, showing promise for medical applications, which was made with multiple layers of SMPs [21]. However, SMP actuators can only undergo passive shape changes without active self-actuation, which limits their use as primary actuators in adaptive soft robotic systems. SMPs and SMAs are meticulously modelled with advanced software tools suited for numerical simulations, facilitating the utilization of constitutive equation-based models [22]. Depending on the complexity of the model and various other considerations, such as the material's mechanical properties, these models are tailored to accurately describe nonlinear behaviours of smart materials with the help of FEA [23].

Shape morphing enables structures to adapt and respond to external stimuli, facilitating functions such as gripping, locomotion, and shape adaptation [24, 25]. These systems integrate materials, geometry, and actuation mechanisms to achieve controlled deformations, eliminating the need for mechanical joints and reducing friction, wear, and maintenance [26]. Unlike rigid systems with discrete movements, morphing structures deform continuously, enhancing energy efficiency and versatility [27]. Morphology defines form, spatial arrangement, and deformation pathways, crucial for performance. Smart materials enable self-actuating structures that respond autonomously to stimuli, eliminating external actuation. By combining geometric and microstructural properties, morphology enables reversible transformations, bridging form and function [28, 29]. Shape-morphing solar shading systems use SMAs, SMPs, and hybrids to dynamically adjust to solar radiation and temperature, enhancing energy efficiency while reducing reliance on artificial lighting and cooling. Inspired by plant movements, they optimise light and heat control with minimal energy input, offering a sustainable, low-maintenance alternative to mechanical shading [30]. Robotic grippers benefit from shape morphing by using flexure hinges with morphable flaps to dynamically adjust stiffness. Inspired by origami, pneumatically actuated pouches control finger flexibility, allowing secure grasps of varied objects without complex control systems [31]. Another application would be the use of soft materials to form a gripper consisting of hydrogel and SMPs, therefore enabling the self-actuation and stiffness control [27].

This study presents an integrated system of a morphing structure based on SMP meta-structure and SMA springs, enabling comparative work of multiple smart materials for mechanical intelligence. The main contributions can be summarized as follows. First, a morphing structure incorporating multiple types of shape memory materials is proposed, which allows customizable deformations. This structure is proposed by the use of a model-based design for morphing structures. Secondly, a Design of Experiments is conducted to investigate the interactions between design parameters. Lastly, future applications are given by combining multiple structures.

2 Design of the morphing structure

To enable adaptable deformation for soft robotics, the intelligent building block characterized by SMA springs and SMP meta-structure is proposed into a single structure connected by two polymethyl

methacrylate (PMMA) plates. As shown in Figure 1(a), the design features an SMP structure with three SMA springs around it. The SMA springs provide movement force, while the SMP core acts as a switch, controlling the actuator's shape-locking ability through stiffness adjustment. Using a two-way shape memory effect, the SMA springs shift between high-temperature and low-temperature shapes [32]. Once the desired movement is achieved, the SMP core transitions from flexible to rigid, locking the structure's shape through precise temperature control [33]. Furthermore, the SMP structure is designed in a cylindrical shape to allow for movement in multiple directions. The working process is illustrated in Figure 1(b). Initially, the entire structure remains straight at room temperature (298 K). To begin the process, the SMP structure is heated to reduce its stiffness, allowing it to change shape. Next, by selectively heating three SMP springs, the structure bends in specific directions and angles as needed. Finally, the SMP structure is cooled to restore stiffness, which locks it into the new shape, which's bending performance is evaluated by bending angle (φ). Additionally, when the SMA springs return to room temperature, simply reheating the SMP structure enables it to revert to its original shape. Furthermore, the building block can transition from its initial state or between working configurations through a stepping process. As illustrated in Figure 1(b), once the building block reaches Working Configuration 1, it can lock into that shape. Then, by independently controlling the SMA springs, another SMA spring can be activated to transition to Working Configuration 2. This stepping mechanism enables the building block to switch between different configurations, supporting a wide range of shape transformations.

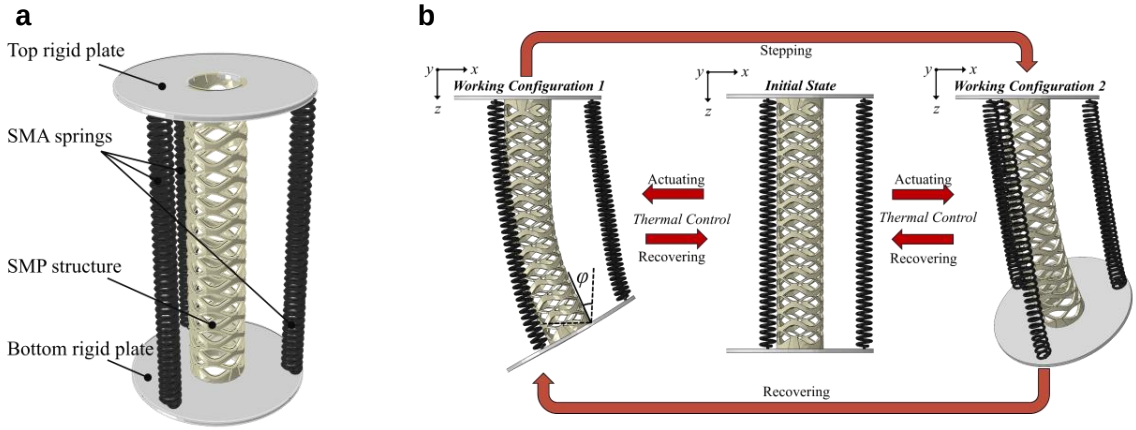

Figure 1. The proposed building block structure and working principle *(a) Demonstration the structure (b) Working process of the building block*

The detailed geometric parameters are presented in Figure 2. The cylinder has a length L of 200 mm, an inner diameter d_c of 35 mm, and a wall thickness t_p of 2.5 mm. The connection boards on both ends have a thickness t_c of 3 mm, with a total diameter D of 106 mm. The deployment holes for the SMP springs are uniformly distributed along a circle with a radius r_h of 45 mm. The SMP meta-structure is defined by a waved lattice unit. Each lattice unit has a total length l_m of 30 mm, with a middle gap length l_h of 21.35 mm. The upper layer of the lattice has a thickness t_u of 1.8 mm, while the lower layer has a thickness t_d of 4 mm.

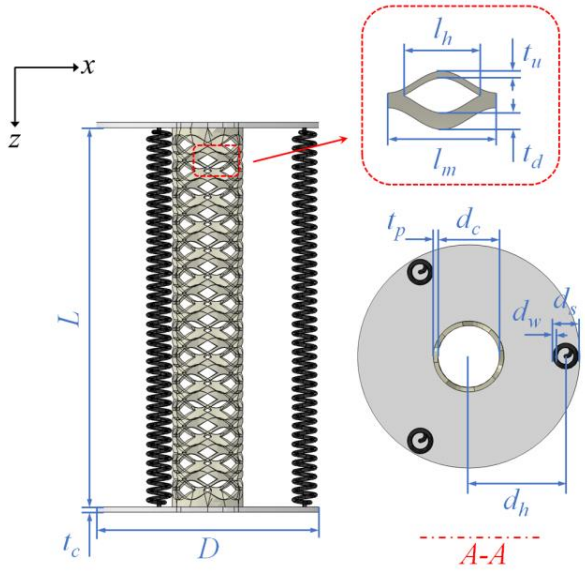

Figure 2. Geometric parameters

3 Methodology

Numerical modelling

The finite element method (FEM) is used in this study to model smart materials and analyze the performance of proposed morphing structure [60]. To simulate SMA behavior, an isotropic thermo-mechanical constitutive model was implemented as an ABAQUS user-defined material (UMAT) [61, 62]. The Helmholtz free energy per unit reference volume is calculated as:

$$\psi = \psi^e + \psi^\xi + \psi^\tau \tag{1}$$

$$\psi^e = \widehat{\psi^e}(\boldsymbol{E}^e, \tau) = \frac{1}{2}\boldsymbol{E}^e.\boldsymbol{C}[\boldsymbol{E}^e] - \boldsymbol{A}(\tau - \tau_0).\boldsymbol{C}[\boldsymbol{E}^e] \tag{2}$$

$$\psi^\xi = \widehat{\psi^\xi}(\tau, \xi) = \frac{\lambda_T}{\tau_T}(\tau - \tau_0)\xi \tag{3}$$

$$\psi^\tau = \widehat{\psi^\tau}(\tau) \tag{4}$$

In these expressions, ψ^e represents the thermos-elastic free energy density, $\boldsymbol{E}^e = \frac{1}{2}(\mathbf{C}^e - \mathbf{I})$ is the elastic strain, and $\mathbf{C}^e = \mathbf{F}^{eT}\mathbf{F}^e$ where is the elastic distortion. $\mathbb{C} = 2\mu\mathbb{I} + \left(\kappa - \frac{2\mu}{3}\right)\mathbf{I}\otimes\mathbf{I}$ is the fourth-order elastic moduli tensor where μ is the shear modulus and κ is the bulk modulus. $\boldsymbol{A} = \alpha\mathbf{I}$ is the second order thermal expansion tensor where α being the thermal expansion coefficient. τ is the current temperature, and τ_0 represents the reference temperature.ψ^ξ represents the phase transformation free energy density, $\Delta H_T$is the constant latent heat of phase transformation, $\xi \in [0, 1]$ is the martensitic volume fraction and $\tau_T = (M_s + A_s)/2$ is the transformation temperature where M_s is the martensite start temperature and A_s is the austenite start temperature. ψ^τ represents the pure thermal free energy density.

According to the Helmholtz free energy, the stress tensor can be expressed as:

$$\boldsymbol{T} = \frac{\partial\psi}{\partial\boldsymbol{E}^e} = \mathbb{C}[\boldsymbol{E}^e - \boldsymbol{A}(\tau - \tau_0)] \tag{5}$$

And the elastic distortion can be considered as part of the total deformation gradient $\mathbf{F} = \mathbf{F}^{e}\mathbf{F}^{inel}$ where $\mathbf{F}^{inel}$ is the inelastic transformation distortion being found from:

$$\dot{\boldsymbol{F}}^{inel} = \left\{\sqrt{1.5}\bar{\varepsilon_t}\dot{\xi}\boldsymbol{S}\right\}\boldsymbol{F}^{inel} \tag{6}$$

where $\boldsymbol{S} = \frac{sym(C^{e}T)_{dev}}{|sym(C^{e}T)_{dev}|}$ is the inelastic flow direction and $\bar{\varepsilon}_{\mathrm{t}}$ is the maximum transformation strain.

In this study, the SMA (Ni-Ti alloy) wires are with martensite start temperature $M_s = 325$ K, martensite finish temperature $M_f = 315$ K , austenite start temperature $A_s = 341$ K , and austenite finish temperature$A_f = 351$ K. Furthermore, Young's modulus of the alloy in martensite phase and in austenite phase are 28 GPa and 75 GPa, respectively.

To elucidate the mechanical behavior of SMP, the superimposed generalized Maxwell model and Williams-Landel-Ferry (WLF) equation within Abaqus finite element solver are utilized. The utilized constitutive equations for the multi-branch viscos-elasticity are as follows [34],

$$\sigma(t) = \varepsilon_0 E_n + \varepsilon_0 \sum_{i=1}^{n-1} E_i e^{\frac{-t}{\tau_i}} \tag{7}$$

where $\sigma(t)$ represents stress at time *t*, ε_0 is the strain at the initial time,E_n is the instantaneous modulus, E_i is the elastic modulus and τ_i is the relaxation time of the Maxwell element *i*. The relation of relaxation modulus *E* in the generalized Maxwell equation with time *t* is expressed as:

$$E(t) = E_n + \sum_{i=1}^{n-1} E_i e^{\frac{-t}{\tau_i}} \tag{8}$$

satisfying the limit condition:

$$\lim_{t\to\infty} E(t) = E_n \tag{9}$$

Performing relaxation experiments at different temperatures and using the time–temperature equivalence principle is crucial. This approach enables the transformation of the relaxation response curves of SMP from various temperatures into a unified relaxation response curve at a chosen reference temperature. According to the WLF equation [34], the connection between the relaxation time at the present temperature *T* and the relaxation time at the reference temperature of T_r is given by:

$$\lg\alpha_T = \lg\frac{\tau}{\tau_r} = \frac{-C_1(T - T_r)}{C_2 + (T - T_r)} \tag{10}$$

where α_T represents shift factor, C_1 and C_2 are material constant. It is assumed that the glass transition temperature $T_g$is equivalent to the T_r. Furthermore, Polylactic acid (PLA) was chosen as the SMP in this study [35]. The viscoelastic and thermal property parameters are specified as follows, $T_g = 334$ K, $C_1 = 6.14$, and $C_2 = 293$ K [36]. At a temperature of 298 K, the material's elastic modulus was 1000 MPa, but it decreased by 60% when reaching the transition temperature.

Experimental Setup

The SMP cylinder was produced using a Builder EXTREME 1500 PRO 3D printer with PLA filament. The SMA springs were made from a Ni-Ti alloy with a wire diameter of 2.3 mm, which has minimal decomposition tendencies, and were trained using the TWSME process [37]. The springs are designed to

contract to 100 mm when heated and extend to 200 mm upon cooling. The upper and lower circular connectors, which secure the actuators, were laser cut from 3 mm thick PMMA plates. The cooling fan used is a Delta AFB0912HH, capable of a maximum airflow of approximately 58 CFM. As for the control part, the MLX90640 infrared thermal imaging sensor array is utilized, which provides a 32x24 temperature matrix and adjusts its measurements based on ambient temperature [38].

The connection of each component is shown in Figure 4(a), The SMA springs are directly powered and heated via Joule heating, and no additional cooling equipment is needed due to the relatively low cooling demands of the springs. Since SMP has poor electrical and thermal conductivity, an external heating element is required. Polyimide film heating pads (PI heaters), fabricated to match the inner surface of the SMP cylinder, were used. These heaters have very low stiffness, excellent insulation, and high thermal conductivity, and utilize thin etched stainless steel alloy sheets as heating elements. This design ensures the heaters have negligible impact on the structure's bending motion while preventing the SMP from exposure to any external electrical stimuli that could introduce errors. To accelerate cooling, a small fan is placed at the top of the cylinder, utilizing the air duct formed by the PI heaters. This setup also minimizes any cooling interference between the SMP and SMA. The sensor should be positioned at a distance of 50–100 mm from the cylinder, avoiding placement near the upper and lower ends. Additionally, the control circuit design is shown in Figure 4(b). To preserve the deformed shape and prevent any loss of shape memory, the SMP structure requires precise temperature regulation. For this purpose, a Pulse Width Modulation (PWM) circuit is utilized to maintain accurate temperature control. On the other hand, SMA springs do not require such strict temperature control. However, to achieve specific bending behaviors, SMA springs must undergo deformation through multiple steps. To facilitate this controlled deformation, a MOSFET-based switching circuit operating in a stepwise mode is employed. This setup allows the SMA springs to deform progressively, ensuring tailored bending responses without needing the precise temperature adjustments necessary for the SMP structure.

a

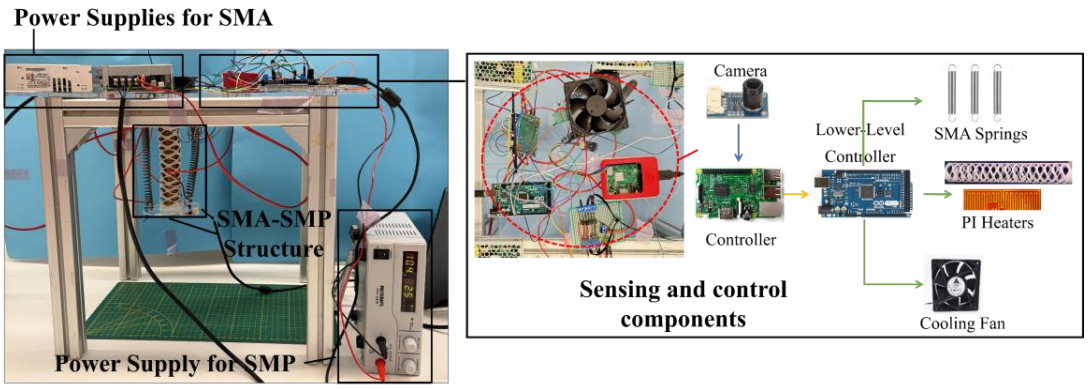

b

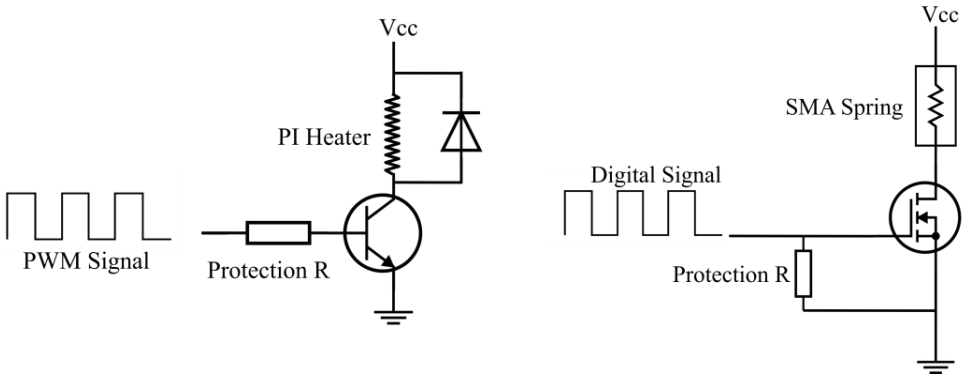

Figure 3. The experimental setup *(a) Setup of different components (b) Control circuit design*

4 Results and Discussion

Validation of the numerical modellings

The bending performance is then evaluated by comparing simulation results with experimental data to confirm the feasibility of the building blocks. For this analysis, the maximum contraction of a single activated Shape Memory Alloy (SMA) spring is defined as the "fully loaded" state. The loading process is represented on a scale from 0 to 100, indicating the percentage of the loading state relative to the current contraction level of the actuating SMA springs. Figure 7 presents a comparison of bending performance, illustrating the single-spring actuation mode in Figure 7(a) and the double-spring actuation mode in Figure 7(b). As shown in Figure 7(a), both the experimental and simulation results for the building block driven by a single spring exhibit similar trends, reaching a maximum bending angle of approximately 42° under full loading process. In particular, the numerical data show a linear increase as the loading progresses, whereas the experimental data initially rise more slowly, likely due to environmental factors. Additionally, the numerical results are generally slightly higher than the experimental ones. This discrepancy can be attributed to the rigid connections between parts in the experiment, which limit the bending performance to some extent. However, as the loading process approaches to 100%, the spring provides sufficient force, minimizing the impact of these connections on the experimental outcomes.

As illustrated in Figure 7(b), the distribution of double-spring actuation follows a similar trend, achieving a maximum bending angle of around 65°, indicating that the double-spring actuation mode allows for a greater range of motion. However, unlike the single-spring actuation mode, where the bending angle increases steadily throughout the loading process from 0 to 70% then get slowing. Up to 70%, the SMP structure approaches its stretching limit, which results in a slower increase in bending angle between 70% and 100% loading process. In addition, the experiment shows a difference in bending performance of 5° less than the simulation result, which is because the experimental conditions were less controlled than in simulations, resulting in a greater tendency for the SMP structure to fatigue.

a **b**

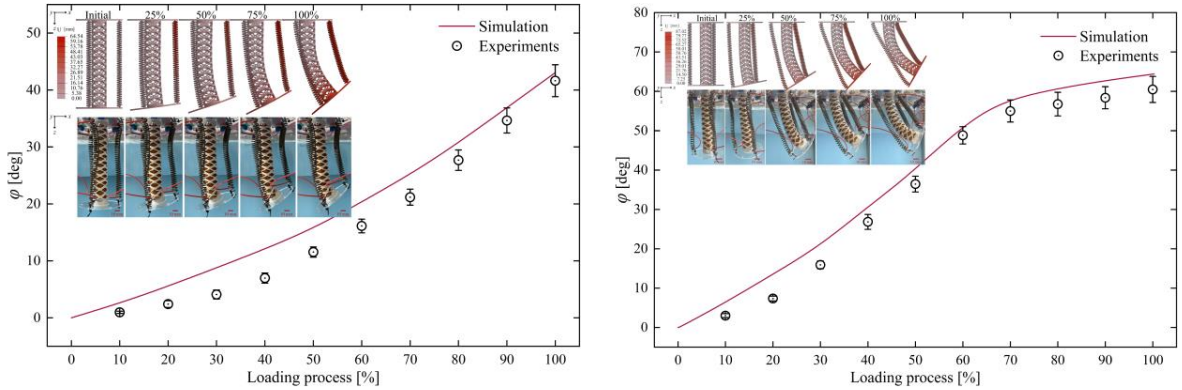

Figure 4. Validation of the bending performance *(a) Bending performances of the single-spring actuation (b) Bending performances of the double-spring actuation*

Sensitivity Analysis of Different Structure Designs

For the final design, a sensitivity analysis is conducted to evaluate the influence of the dimensions of the intelligent building block on bending behaviour. This analysis focuses on four key parameters: $t_{p,}$ l_m, segment ratio (r_s) which equals $t_{u/}$ t_d, and unit height (u_h). Adjustments to these parameters were made to evaluate their impact on the design's performance. The parameter values were carefully chosen to ensure that the geometry remains feasible for the patterned structure of the unit. This ensures that the fundamental concept and generic shape of the lattice unit, including its buckling mechanism, are preserved.

Table 1. Results of the sensitivity analysis

u_h [mm]	φ [deg]	l_m [mm]	φ [deg]	r_s [-]	φ [deg]	t_p [mm]	φ [deg]
12.5	44.6	10	5.14	0.2	24.5	1.5	57.3
16.5	50.0	20	26.0	0.4	50.0	2.0	54.2
20.5	51.9	30	50.0	0.6	36.0	2.5	50.0
24.5	54.0	40	58.1	0.8	26.0	3.0	47.1
28.5	56.3	60	55.3	1.0	19.7	3.5	43.6

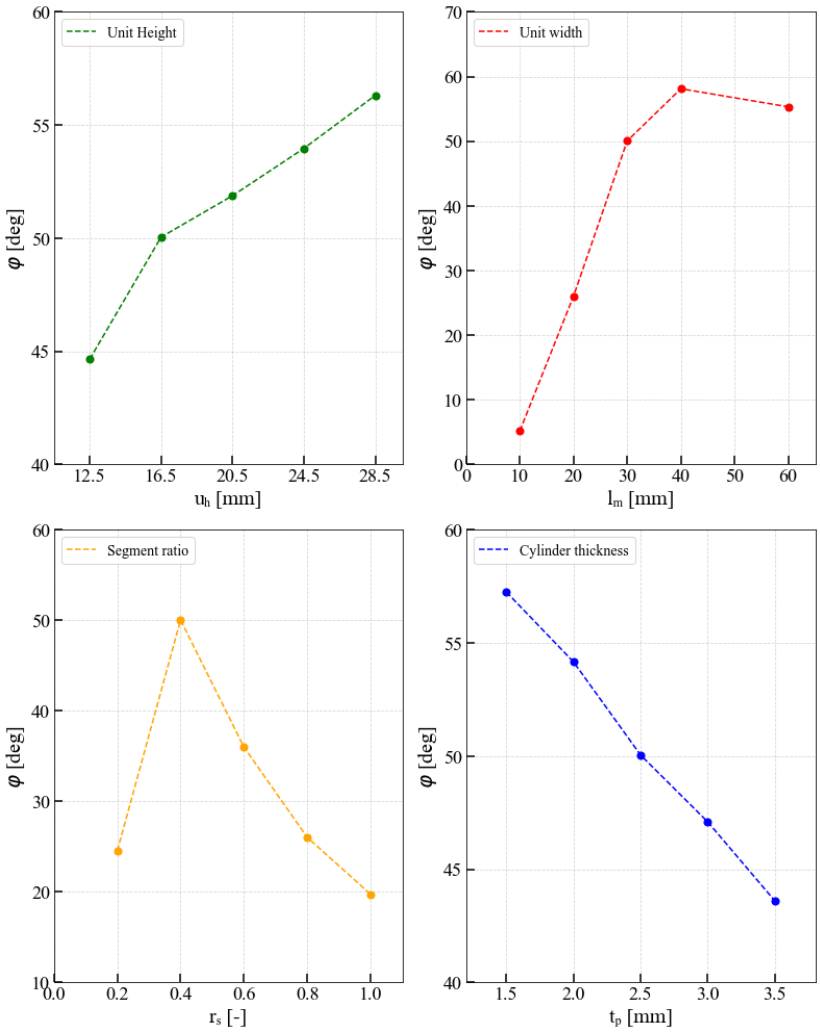

Figure 5. Bending angle plotted against four parameters. *(a) Unit height (b) Unit width (c) Segment ratio (d) Cylinder thickness*

Figure 5a shows an increase in bending angle with increasing u_h. Taller units increase the distance between the upper and lower segments, providing more space for deformation, leading to more bending. A peak in φ is found at u_h = 28.5 mm. Figure 5b shows initial increase in bending angle with a peak reached at l_m = 40 mm. This indicates an optimal width for maximum bending. Beyond this width, the top part of the structure begins to curl in the opposite direction, reducing the net bending angle. Figure 5c shows a big peak at r_s = 0.4, anything beyond this point results in a decrease in bending. At r_s = 0.2, the structure becomes overly flexible and buckles excessively, impairing functionality. This highlights the importance of achieving an optimal ratio where $t_u < t_d$. Figure 5d shows a linear decrease of bending angle with thicker cylinders. This underscores the trade-off between structural strength and flexibility, with thinner cylinders being preferable for applications requiring larger bending angles.

The analysis reveals that the bending angle is strongly influenced by these four parameters. findings underscore the importance of parameter optimisation for superior shape-morphing performance.

2 DoE (optimization process)

Design of Experiments (DoE) systematically examines the relationship between unit geometry and bending angle, identifying key parameters and their impact on deformation . It optimizes geometric variables to achieve desired bending performance, making it crucial for shape-morphing structures. In this study, DoE efficiently analyses the influence of unit geometry while reducing simulation requirements and computational effort. A factorial approach is used with four factors (u_h, l_m, r_s, and t_p) at two levels (high and low) found in Table 2, requiring 16 simulations (2^4). For deeper interaction analysis, 12 two-factor combinations are reduced to six unique pairs with four simulations each, resulting in 24 total simulations. The design matrix used is shown in Table 3.

Table 2. Levels used of the four parameters.

	Low (-1)	High (+1)
u_h	12.5	28.5
l_m	10	40
r_s	0.4	1.0
t_p	1.5	3.5

Table 3. Design matrix of a two-factor factorial design

Factor 1	Factor 2
-1	-1
-1	1
1	-1
1	1

Interactions occur when one factor's effect on bending depends on another's level, often producing nonlinear outcomes. For example, a factor may increase bending at one level but decrease it at another when combined with a second factor. If no interaction exists, a parameter's effect remains constant. Interaction plots help visualise these effects, with parallel lines indicating no interaction and crossing or diverging lines signifying interaction.

Figures 6a and 6b show no to minimal interaction since the lines follow a parallel path, meaning that each of these parameters can be increased with no extra effect on the bending angle by the second parameter. Figures 6c and 6d do show convergence of the lines, indicating the presence of interaction. Figure 6c suggests that taller units mitigate the negative impact of increasing r_s, enhancing robustness to segment ratio changes, while Figure 6d suggests that wider units consistently improve bending, but the effect diminishes at lower t_p. Figures 6e and 6f show major interaction, with great convergence and crossing of lines. Figure 6e shows strong interaction which suggests that wider units are more sensitive to r_s variations, whereas narrower units are less affected. Figure 6f indicates that at lower u_h, increased thickness adds stiffness and reduces bending, whereas at higher u_h, structural integrity is enhanced, slightly improving bending.

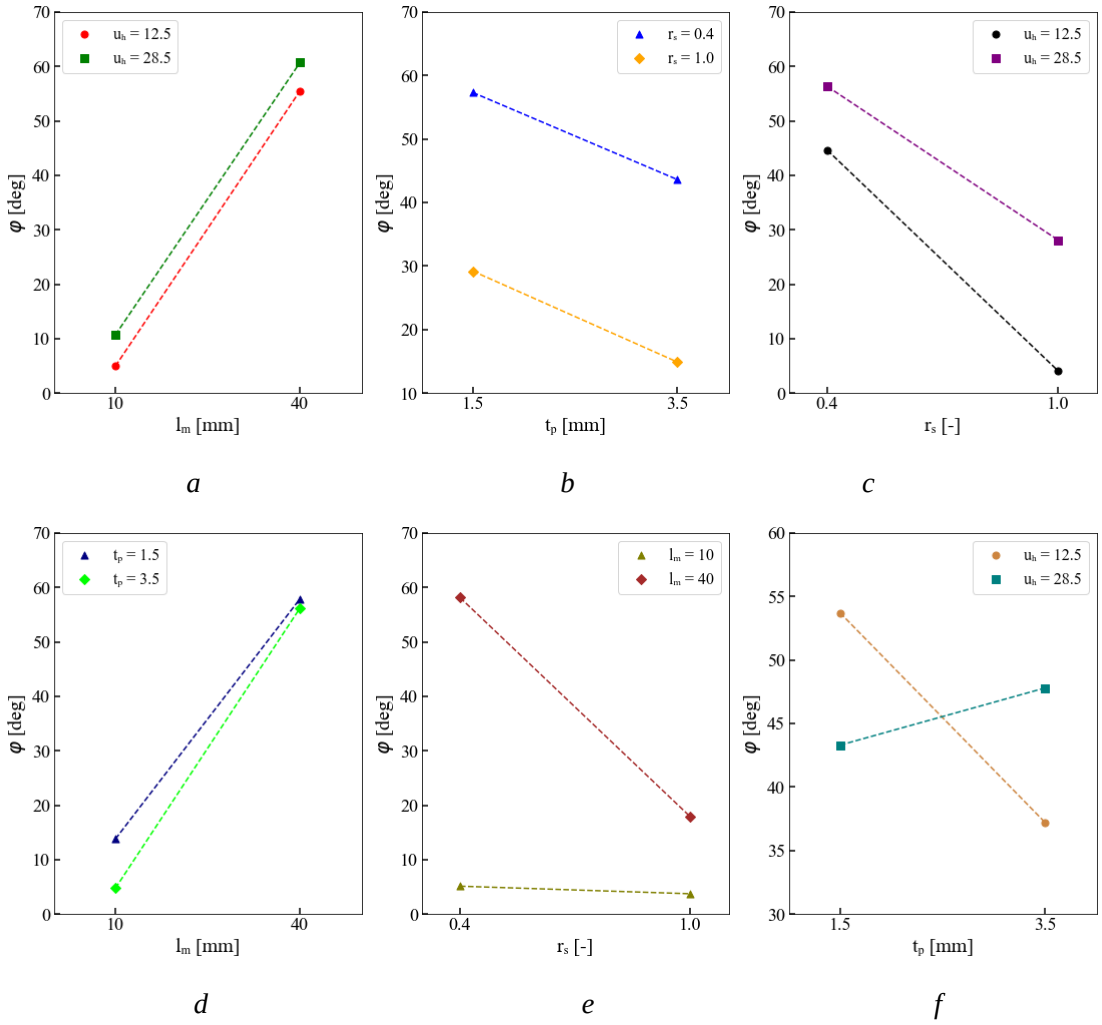

Figure 6. Interaction plots of DoE. *(a) Unit width and unit height (b) Cylinder thickness and segment ratio (c) Segment ratio and unit height (d) Unit width and cylinder thickness (e) Segment ratio and unit width (f) Cylinder thickness and unit height*

Potential applications performance

The potential applications of these cylinder structures extend far beyond single-direction bending. By combining multiple cylinders in series, it is possible to create highly adaptable actuation systems capable of multi-directional bending. Each cylinder within the system contributes to bending along a distinct axis. For instance, one cylinder may enable bending in the vertical plane, while another allows bending in the horizontal plane. This modular approach enables precise and programmable motion profiles, making it ideal for applications in (soft) robotics and adaptive mechanisms. By implementing cylinders with varying geometries or integrating actuated SMA springs, such structures can achieve both controlled and versatile deformation behaviours.

The dual-cylinder configuration Figure 7 enables bi-directional bending, making it suitable for planar motion applications such as gripping or flexing. By orienting the cylinders at specific angles, controlled deformation in orthogonal directions is achieved. The displacement path, shown in Figure 7b , highlights key aspects like maximum displacement, curvature, and segment motion.

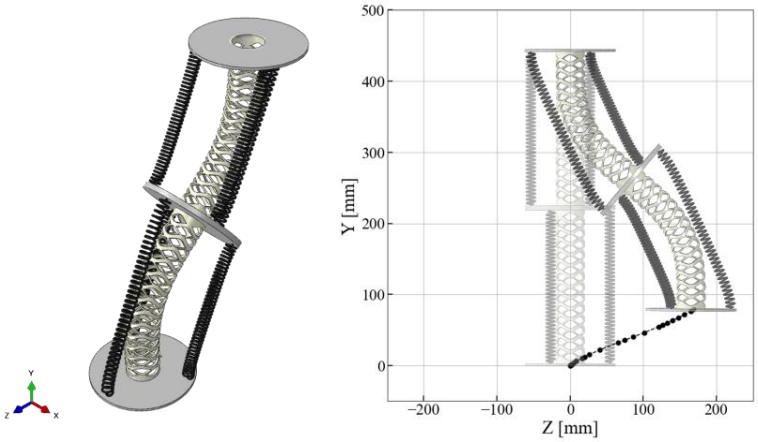

Figure 7. Double cylinder configuration. *(a) Isometric view of the deformed state (b) Displacement path of the deformed structure in the YZ plane.*

Introducing a second cylinder perpendicular to the first, as in Figure 8 enhances functionality by enabling 3D shape morphing and multi-axial deformation. This configuration expands motion capabilities beyond a single plane, allowing for complex movement patterns.

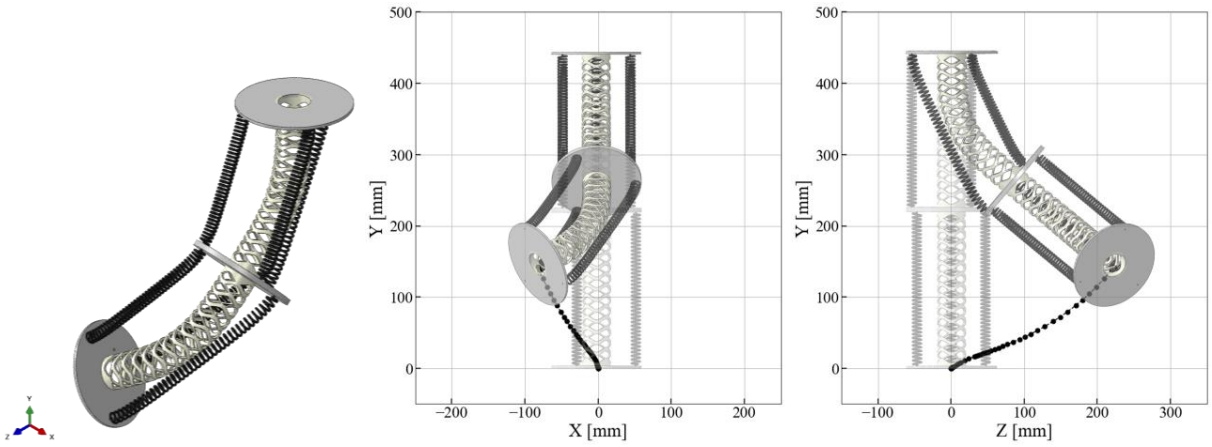

Figure 8. Double cylinder with perpendicular orientation. *(a) Isometric view of the deformed state (b) Displacement path of the deformed structure in the YX plane. (c) Displacement path of the deformed structure in the YZ plane.*

Stacking multiple cylinders further increases bending flexibility, facilitating intricate multi-dimensional motion. The modular nature of this approach supports customisation for applications such as adaptive robotic arms and biomedical devices. A practical example of this concept is demonstrated in the triple-cylinder setup Figure 9.

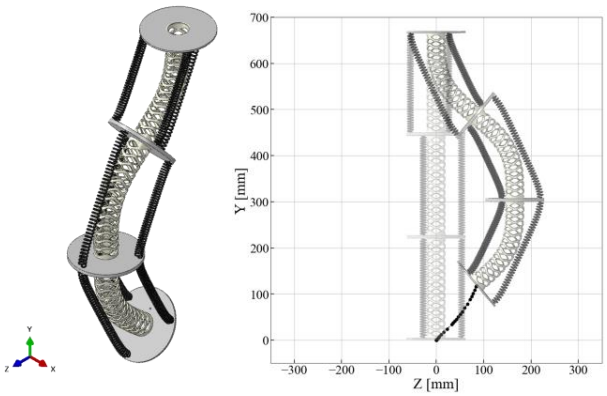

Figure 9. Triple cylinder configuration. *(a) Isometric view of the deformed state (b) Displacement path of the deformed structure in the YZ plane.*

5 Conclusion

In this study, we developed a building block designed as a morphing structure using shape memory materials. This morphing structure is capable of achieving tailored deformation behaviors through an integrated system, making it suitable for use as mechanical intelligence in soft robotics applications. The system is composed of a structural unit featuring three SMA springs arranged around an SMP-based meta-structure. The SMA springs provide the actuation force necessary to drive the movement of the structure, while the SMP core enables adjustable stiffness to lock the structure into its desired shape. Furthermore, the integrated thermal control system facilitates self-actuation, enabling the structure to perform controlled and precise motions.

A numerical model integrating SMA springs with SMP structure was successfully developed. The simulation results closely matched the experimental data, verifying the feasibility of proposed morphing structure. Specifically, the structure achieved a maximum bending angle of 65° with double-spring actuation and 42° with single-spring actuation. This method demonstrated its ability to swiftly stabilize the temperature within the desired range, achieving this in as little as 20 seconds. The rapid and consistent performance highlights the potential of the MTTS approach in applications requiring accurate thermal regulation. By incorporating the MMTS method with a PID control algorithm, a comprehensive integration system was developed, capable of supporting multiple working modes to achieve diverse functionalities. In stepping mode, the system enabled precise step-by-step actuation, completing full loading within 30 seconds within four stepping steps of 6 seconds each and three pulsing steps of 2 seconds each. The use of stepping mode enables the morphing structure to effectively transition between shapes by self-actuation, whether starting from its initial state or an existing configuration. The forming and recovery modes facilitated shape locking and recovery, with braking times of 50 and 40 seconds, respectively. In the locked state, the bending stiffness increased by up to 4.5 times. In addition, the recovery process exhibited a slight hysteresis, requiring approximately 15 seconds longer than the stiffness adjustment to fully restore the initial posture. The integration system improves the robustness and versatility of the morphing structure, providing valuable insights for developing mechanical intelligence with efficient self-actuation and reliable control.

However, the current control system cannot fully compensate for the target deformation. Our next step involves incorporating posture detection to achieve precise shaping of the morphing structure's deformation. Additionally, the current cooling actuators are inefficient, resulting in excessive braking time. Future work will focus on optimizing the morphing structure's design and integrating actuators with significantly improved cooling performance.

Acknowledgements

Competing interests

The author(s) declare no competing interests.

Data availability statement

The datasets generated during and/or analysed during the current study are available from the corresponding author on reasonable request.

References

[1] M. Calisti, G. Picardi, and C. Laschi, "Fundamentals of soft robot locomotion," *Journal of The Royal Society Interface,* vol. 14, no. 130, pp. 20170101, 2017.

[2] M. T. Tolley, R. F. Shepherd, B. Mosadegh, K. C. Galloway, M. Wehner, M. Karpelson, R. J. Wood, and G. M. Whitesides, "A resilient, untethered soft robot," *Soft robotics,* vol. 1, no. 3, pp. 213-223, 2014.

[3] S.-H. Ahn, K.-T. Lee, H.-J. Kim, R. Wu, J.-S. Kim, and S.-H. Song, "Smart soft composite: An integrated 3D soft morphing structure using bend-twist coupling of anisotropic materials," *International Journal of Precision Engineering and Manufacturing,* vol. 13, pp. 631-634, 2012.

[4] C. Majidi, "Soft robotics: a perspective—current trends and prospects for the future," *Soft robotics,* vol. 1, no. 1, pp. 5-11, 2014.

[5] D. Rus, and M. T. Tolley, "Design, fabrication and control of soft robots," *Nature,* vol. 521, no. 7553, pp. 467-475, 2015.

[6] H. Tari, S. S. Santapuri, and M. J. Dapino, "Efficient and robust nonlinear model for smart materials with application to composite magnetostrictive plates," *Smart Materials and Structures,* vol. 26, no. 4, pp. 045010, 2017.

[7] T. Manouras, and M. Vamvakaki, "Field responsive materials: photo-, electro-, magnetic-and ultrasound-sensitive polymers," *Polymer Chemistry,* vol. 8, no. 1, pp. 74-96, 2017.

[8] K. Song, S. H. Kim, S. Jin, S. Kim, S. Lee, J.-S. Kim, J.-M. Park, and Y. Cha, "Pneumatic actuator and flexible piezoelectric sensor for soft virtual reality glove system," *Scientific reports,* vol. 9, no. 1, pp. 8988, 2019.

[9] G. Stano, and G. Percoco, "Additive manufacturing aimed to soft robots fabrication: A review," *Extreme Mechanics Letters,* vol. 42, pp. 101079, 2021.

[10] S. Aracri, F. Giorgio-Serchi, G. Suaria, M. E. Sayed, M. P. Nemitz, S. Mahon, and A. A. Stokes, "Soft robots for ocean exploration and offshore operations: A perspective," *Soft Robotics,* vol. 8, no. 6, pp. 625-639, 2021.

[11] J. Shintake, V. Cacucciolo, D. Floreano, and H. Shea, "Soft robotic grippers," *Advanced materials,* vol. 30, no. 29, pp. 1707035, 2018.

[12] R. Casati, F. Passaretti, and A. Tuissi, "Effect of electrical heating conditions on functional fatigue of thin NiTi wire for shape memory actuators," *Procedia Engineering,* vol. 10, pp. 3423-3428, 2011.

[13] R. Bogue, "Shape‐memory materials: a review of technology and applications," *Assembly Automation,* vol. 29, no. 3, pp. 214-219, 2009.

[14] M. Bashir, C. F. Lee, and P. Rajendran, “Shape memory materials and their applications in aircraft morphing: an introspective study,” *ARPN J. Eng. Appl. Sci,* vol. 12, no. 19, pp. 5434-5446, 2017.
[15] A. Villanueva, C. Smith, and S. Priya, “A biomimetic robotic jellyfish (Robojelly) actuated by shape memory alloy composite actuators,” *Bioinspiration & biomimetics,* vol. 6, no. 3, pp. 036004, 2011.
[16] Y. Kakubari, F. Sato, H. Matsuki, T. Sato, Y. Luo, T. Takagi, T. Yambe, and S.-i. Nitta, “Temperature control of SMA artificial anal sphincter,” *IEEE transactions on magnetics,* vol. 39, no. 5, pp. 3384-3386, 2003.
[17] K. Yang, and Y. Wang, “Design, drive and control of a novel SMA-actuated humanoid flexible gripper,” *Journal of mechanical science and technology,* vol. 22, pp. 895-904, 2008.
[18] A. Borboni, and R. Faglia, “Characterization of a new SMA actuator,” *Procedia Engineering,* vol. 87, pp. 1378-1381, 2014.
[19] X. Lan, Y. Liu, H. Lv, X. Wang, J. Leng, and S. Du, “Fiber reinforced shape-memory polymer composite and its application in a deployable hinge,” *Smart Materials and Structures,* vol. 18, no. 2, pp. 024002, 2009.
[20] C. Son, S. Jeong, S. Lee, P. M. Ferreira, and S. Kim, “Tunable adhesion of shape memory polymer dry adhesive soft robotic gripper via stiffness control,” *Robotics,* vol. 12, no. 2, pp. 59, 2023.
[21] Z. Liu, J. Liu, H. Wang, X. Yu, K. Yang, W. Liu, S. Nie, W. Sun, Z. Xie, and B. Chen, “A 1 mm-thick miniatured mobile soft robot with mechanosensation and multimodal locomotion,” *IEEE Robotics and Automation Letters,* vol. 5, no. 2, pp. 3291-3298, 2020.
[22] Q. Chen, T. Kalpoe, and J. Jovanova, “Design of mechanically intelligent structures: Review of modeling stimuli-responsive materials for adaptive structures,” *Heliyon,* 2024.
[23] Q. Guo, W. Yao, W. Li, and N. Gupta, “Constitutive models for the structural analysis of composite materials for the finite element analysis: A review of recent practices,” *Composite Structures,* vol. 260, pp. 113267, 2021.
[24] F. Xu, and H. Wang, “Soft robotics: Morphology and morphology-inspired motion strategy,” *IEEE/CAA Journal of Automatica Sinica,* vol. 8, no. 9, pp. 1500-1522, 2021.
[25] Q. Chen, D. Schott, and J. Jovanova, “Model-Based Design of Variable Stiffness Soft Gripper Actuated by Smart Hydrogels,” *Soft Robotics,* 2024.
[26] L. Ren, B. Li, G. Wei, K. Wang, Z. Song, Y. Wei, L. Ren, and Q. Liu, “Biology and bioinspiration of soft robotics: Actuation, sensing, and system integration,” *Iscience,* vol. 24, no. 9, 2021.
[27] Q. Chen, D. Schott, and J. Jovanova, “Model-based design of a mechanically intelligent shape-morphing structure,” *Scientific Reports,* vol. 14, no. 1, pp. 26148, 2024.
[28] D. Hwang, E. J. Barron III, A. T. Haque, and M. D. Bartlett, “Shape morphing mechanical metamaterials through reversible plasticity,” *Science robotics,* vol. 7, no. 63, pp. eabg2171, 2022.
[29] N. Tanjeem, M. B. Minnis, R. C. Hayward, and C. W. Shields IV, “Shape‐Changing Particles: From Materials Design and Mechanisms to Implementation,” *Advanced Materials,* vol. 34, no. 3, pp. 2105758, 2022.
[30] Y. Li, Y. Zhao, Y. Chi, Y. Hong, and J. Yin, “Shape-morphing materials and structures for energy-efficient building envelopes,” *Materials Today Energy,* vol. 22, pp. 100874, 2021.
[31] H. Godaba, A. Sajad, N. Patel, K. Althoefer, and K. Zhang, "A two-fingered robot gripper with variable stiffness flexure hinges based on shape morphing." pp. 8716-8721.
[32] Z. Wang, X. Zu, X. Feng, S. Zhu, J. Bao, and L. Wang, “Characteristics of two-way shape memory TiNi springs driven by electrical current,” *Materials & design,* vol. 25, no. 8, pp. 699-703, 2004.
[33] M. Behl, M. Y. Razzaq, and A. Lendlein, “Multifunctional shape‐memory polymers,” *Advanced materials,* vol. 22, no. 31, pp. 3388-3410, 2010.
[34] I. M. Ward, and J. Sweeney, *Mechanical properties of solid polymers*: John Wiley & Sons, 2012.
[35] M. Y. Khalid, Z. U. Arif, R. Noroozi, M. Hossain, S. Ramakrishna, and R. Umer, “3D/4D printing of cellulose nanocrystals-based biomaterials: Additives for sustainable applications,” *International Journal of Biological Macromolecules,* pp. 126287, 2023.

[36] J. Wang, R. Kean, J. Randall, and D. Giles, “The effect of crystallinity on the rheological behavior of poly (lactide),” *International Journal of Polymer Analysis and Characterization,* vol. 4, no. 5, pp. 393-405, 1998.

[37] W. Huang, and W. Toh, “Training two-way shape memory alloy by reheat treatment,” *Journal of materials science letters,* vol. 19, no. 17, pp. 1549-1550, 2000.

[38] E. M. Gorostiza, J. L. Lázaro Galilea, F. J. Meca Meca, D. Salido Monzú, F. Espinosa Zapata, and L. Pallarés Puerto, “Infrared sensor system for mobile-robot positioning in intelligent spaces,” *Sensors,* vol. 11, no. 5, pp. 5416-5438, 2011.

B

Modelling in Abaqus

In this appendix the relevant Abaqus inputs will be displayed. Starting with an elaboration on the simulation setups in Abaqus in section B.1. Secondly, the subroutine used for the modelling of hydrogel is given in section B.2. Python codes for the calculation of the bending angles can be found for Hydrogel models in section B.3 and for SMP models in section B.4.

B.1. Abaqus input modules

The simulations in Abaqus are set up in multiple stages. Each module fulfils a separate function regarding one specific aspect of the simulation. In this section, an overview is given of each of these modules, with all the relevant settings or adjustments made. For cases, that are not explicitly addressed a default option is assumed. The different modules listed are part, property, assembly, step, interaction, load, mesh, optimization, job, visualization and sketch. It is worth noting that the 'optimization' and 'sketch' modules are not used in the scope of this research.

Part

The Part module is the starting point of the Abaqus workflow, where the geometries for simulations are defined. New parts can be created in 2D using simple sketches and then extruded to form 3D objects. Users can choose between deformable, rigid, or discrete parts depending on the simulation requirements.

Several base features are available for geometry creation, including extrusion, revolving, and sweeping. Existing geometry can also be edited using sketch tools to modify elements such as lines, circles, splines, or arcs. Additional tools enable users to split, merge, or refine geometries by adding features like fillets or chamfers. Complex objects can be partitioned into smaller sections to simplify the meshing process. This is often achieved by using reference planes as splitting tools, which help in creating a structured mesh later.

An essential feature of the Part module is the ability to import geometries from external CAD software. Abaqus provides only basic geometry creation capabilities, and its interface can be limiting for complex models. Consequently, it is often more efficient to design parts or assemblies in dedicated CAD programs such as SolidWorks and then import them into Abaqus. For this research, most geometries were created in SolidWorks and imported into Abaqus. This was done by saving the SolidWorks parts as Parasolids, with the extensions (X_T, X_B). The exception is the spherical particles used in the particle-to-particle setups, which were created directly in Abaqus for models involving hydrogel and silicone.

The Property module

This module is used to assign physical attributes to the parts created in the previous step. Materials are defined by specifying their mechanical, thermal, viscoelastic, or electromagnetic properties.

- Mechanical Properties: These include parameters such as density, Young's modulus, plasticity, creep, and hyperelasticity.
- Thermal Properties: Examples include thermal conductivity, heat capacity, and thermal expansion coefficients.

In this research, the materials utilized are SMA, SMP, hydrogels, PMMA, steel, and silicone. The material behaviour for most of these is based on constitutive equations, which form the foundation for defining their response to various stimuli.

Lastly, each material is assigned to a section, and with this a geometry can be selected. This geometry will have the properties of the material, regardless if the geometry is merged later in a structure.

The Assembly Module

The Assembly module in Abaqus is used to combine and position parts created or imported in earlier steps to form a complete model. This is achieved using constraints to align, position, or connect the parts. The constraints available in Abaqus are similar to those in CAD programs and include options such as coincident points, parallel edges, coaxial objects, and face-to-face alignment.

One of the first steps is to ensure the initial part or geometry is properly aligned within the Abaqus interface. This can be done by constraining a feature of the geometry, such as an edge, face, or node, to align with a reference direction, plane, or the global origin (0,0,0). Proper alignment simplifies subsequent steps, particularly when measuring translations or deformations, as all displacements are referenced from the origin. An example of this is shown in Figure B.1, where the centre of the board is aligned with the origin (yellow triad). Additionally, a small reference cube was created on the board to align with the Z-axis. This alignment facilitates the comparison of bending results across different simulations by focusing on the ZY plane.

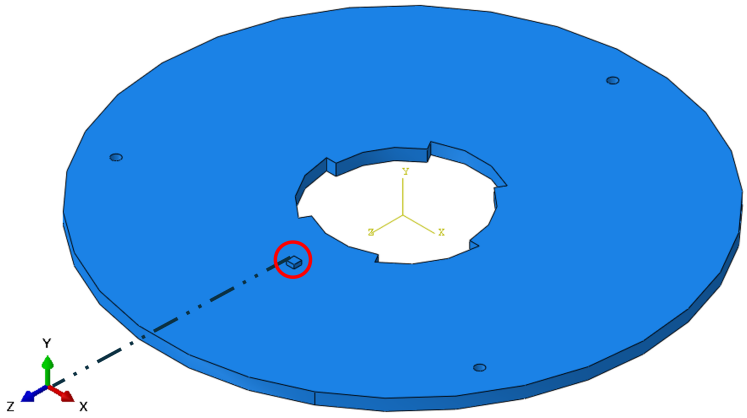

Figure B.1: Example of the centre of the board for the SMP configurations being constrained to the origin.

Once the initial part is aligned, additional components can be constrained relative to it. Constraints are applied to edges, surfaces, or nodes to assemble the parts into a cohesive model. The result is an assembly of parts with defined spatial relationships.

At the final stage, the entire assembly can be merged into a single geometry. This process maintains the individual material properties of each part while creating a unified structure. Merging is beneficial for ensuring realistic interactions between components and simplifies the meshing process.

Additionally, the Assembly module allows for the creation of sets, which are collections of elements, surfaces, or nodes. Sets are particularly useful when specific parts of the merged structure need to be subjected to unique loading or boundary conditions, such as thermal or mechanical loads.

The Step module

The Step module defines the sequence of analysis steps and the associated solution controls. Various step types are available in Abaqus, but the most relevant for this research are Static General and

Viscoelastic:

- Static General: Used for time-independent problems.
- Viscoelastic: Used for rate-dependent problems involving viscoelastic materials.

Simulations in this research are composed of multiple steps, each designed to model a specific part of the process. For instance, heating the smart material occurs in one step, cooling in another, and applying a force might be performed in a separate step. Each step uses one of the selected step types. While it is common for simulations to use a single step type throughout, multiple types can be combined if necessary.

Increment Settings:

- The initial increment size is set to 0.01.
- The minimum increment size is 10^{-8}
- The maximum increment size is 1.
- The total number of increments per step is capped at 5000.

Geometric effects are considered in all steps, while adiabatic heating effects are disregarded. Nonlinear effects are not ignored, ensuring accuracy in the simulation of complex behaviours.

Field Output Requests: Default pre-selected variables, such as displacements, stresses, and strains, are retained. Additionally, thermal outputs are explicitly included to capture temperature-related data.

Interaction

The Interaction module in Abaqus is integral to defining how different components of a model interact with each other and their environment. It is critical for accurate and realistic modelling in multi-part systems. There are several types of interactions available in Abaqus, with the most common being mechanical interactions. These govern how surfaces come into contact and interact during deformation. Mechanical interactions include surface-to-surface contact for modelling the behaviour between two surfaces, and self-contact for scenarios where a part may deform and come into contact with itself.

SMP and SMA

Interaction constraints, such as coupling, were utilized in the models to distribute forces or displacements applied at a reference point across a surface. For example, in preloaded spring simulations, coupling constraints ensured that forces applied to a reference point were evenly distributed on the spring's attachment surface. Cohesion constraints were also employed, particularly in scenarios involving preloading springs. To ensure that the spring remained attached to the structure, an interaction property was defined.

This interaction property incorporated both normal and tangential behaviour. For the normal behaviour, a "hard contact" pressure-overclosure model was used with a penalty enforcement method. The contact stiffness was defined as linear and scaled by a factor of 1. To maintain attachment, the option to allow separation after contact was disabled, ensuring the free end of the spring remained connected to the structure. For the tangential behaviour, a penalty friction formulation was applied, with a coefficient of friction set at 0.3.

Load Module

The load module applies external influences on the model. These external influences can either be loads or boundary conditions. Load can be divided into three categories: mechanical, thermal and predefined fields. In this study, mechanical loads and predefined fields are applicable.

Loads, such as forces, moments, or body loads, can be applied to nodes, surfaces, or entire bodies. They may be ramped up gradually or applied instantaneously, depending on the simulation requirements. The direction of the load can also be explicitly defined. Additionally, loads can be activated, deactivated, or modified during different time steps. For concentrated loads, a coupling constant can be used to distribute the load evenly over an entire surface. This approach was employed in simulations involving a preloaded spring. In these models, the force was applied to a reference point that was coupled to the surface of the spring's attachment point.

Predefined fields are used to assign initial conditions such as temperature, displacement, or velocity to specific regions of the model. In this study, predefined fields are primarily used to represent the different thermal stages experienced by the smart materials. For example, in simulations involving hydrogel, a predefined field is used to set the initial temperature of the material. As the simulation progresses, the temperature is incrementally modified at each time step with 5 K until the final target temperature is reached. In simulations involving SMPs, a predefined field is used to set the heating temperature to deform the structure and lower the temperature to lock in the deformation. Predefined fields are applied to specific areas or geometries. In this case, only the material directly influenced by the temperature changes is selected to ensure accurate representation of thermal effects.

Boundary conditions are used to define displacement and rotation constraints, which restrict the six degrees of freedom of an object. For simulations involving deformable objects, at least one point in the model must be fixed to provide a stable reference frame and clearly observe the deformation. In cases involving expanding hydrogel particles, the entire structure exhibited unintended motion, appearing to "float" in the simulation space. To address this issue, an anchor point or fixed constraint was introduced to stabilize the model and ensure an accurate simulation of the expansion behaviour.

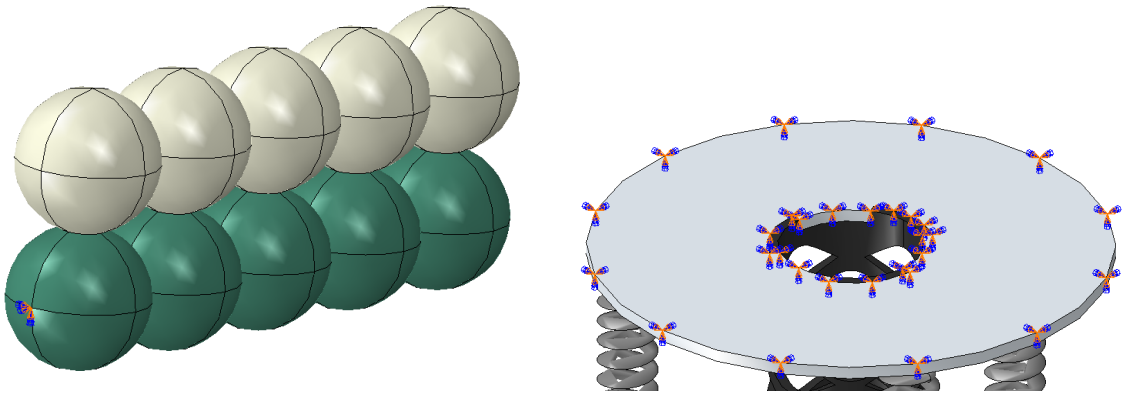

(a) Fix constraint applied at the left side of the hydrogel-silicone models.

(b) Fix constraint applied at the top PMMA board in the SMP-SMA models.

Figure B.2: Examples of 'fixed' constraints applied in models used during this research

The Mesh Module

The Mesh Module discretizes the geometry into finite elements. In this module, a linear or quadratic element can be chosen based on three options; solid, shell or beam. Most of the geometries in this research are meshed with the following element types:

- C3D8H: An 8-node linear brick, hybrid, constant pressure
- C3D4H: A 4-node linear tetrahedron, hybrid, linear pressure.
- C3D10: A 10-node quadratic tetrahedron.

Each character in the element name conveys specific information about its configuration [127]. Specifically, 'C' indicates a continuum element, suitable for this case as the particles are not hollow. The '3D' denotes a three-dimensional solid element, while the second number indicates the number of nodes in the configuration. Finally, 'H' specifies that the element is hybrid with constant pressure. The hybrid formulation is selected due to the Hydrogel's incompressible behaviour, as incompressible materials cannot be accurately modelled using standard elements because the pressure stress in such elements becomes indeterminate [128].

Additionally, the choice can be made between using either Hexahedral 'Hex' or Tetrahedral 'Tet' mesh. Tet is comprised of four triangular faces forming a pyramid-like shape, it is simpler and more suited for meshing complex geometries. On the other hand, Hex is comprised of six quadrilateral faces forming a cuboid-like shape. It is suited for regular and structured geometries. Choosing the right mesh type depends on the problem's geometry, accuracy requirements, and available resources. Other differences between these two options are summarized in Table B.1

Table B.1: Comparison of Tetrahedral and Hexahedral meshes across key criteria

Aspect	Tetrahedral Mesh (Tet)	Hexahedral Mesh (Hex)
Ease of Meshing	Easier, automated	Time-consuming, manual
Geometry Suitability	Complex, irregular	Regular, structured
Accuracy per Element	Lower	Higher
Element Count	Higher for same volume	Lower for same volume
Computation Cost	Higher	Lower
Use Cases	Organic, complex shapes	High-accuracy problems
Example elements	C3D4,C3D10	C3D8,C3D20

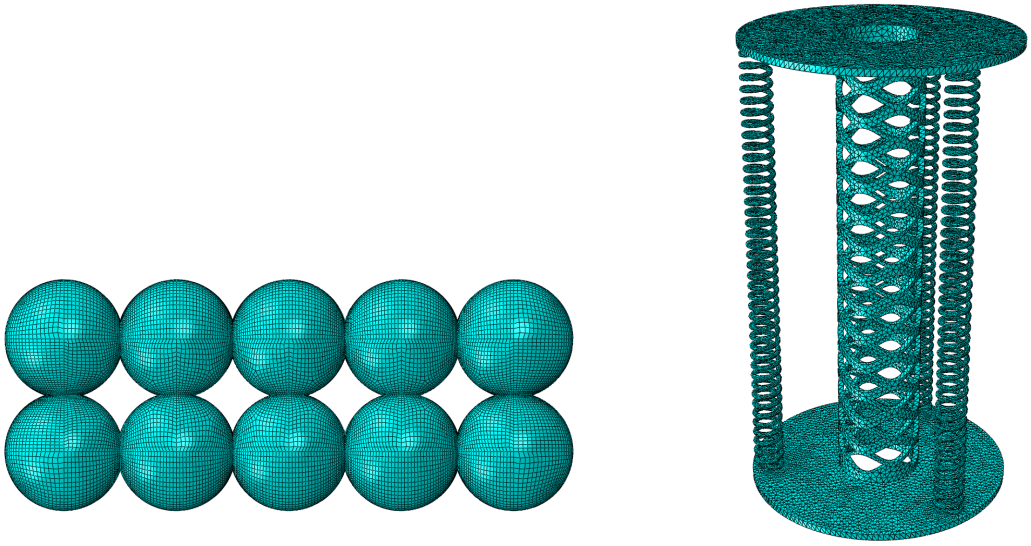

(a) Hydrogel-silicone model meshed with the C3D8H meshtype. **(b)** SMA-SMP model meshed with the C3D10 meshtype.

Figure B.3: Examples of meshed models used during this research.

In addition to this, a convergence refinement study is needed for the use of a proper meshsize. Additional figures and tables on the convergence mesh studies can be found in section C.1.

The Job Module

This module in Abaqus is used to prepare the simulation for submission to the solver. This module allows for the creation and management of analysis jobs, linking the simulation model with the computational engine. Several key functions are performed in this module:

Job Creation: A simulation job is created by selecting a model and providing relevant details, such as a descriptive name and optional metadata. If a subroutine file is required for advanced calculations (e.g., for hydrogel material modeling), it can be specified during this step.
Solver Configuration: The solver settings can be customized to use either single-precision or double-precision solvers, depending on the desired accuracy and computational resources. Additionally, parallelization options can be configured to optimize performance on multi-core systems.
Monitoring: The Job module includes a monitoring tool to track the status of the simulation. This tool provides real-time updates on job creation, submission, and completion. It also flags any issues, such as aborted or terminated jobs, caused by errors or convergence problems. Detailed logs are available to identify warnings or errors, offering insights that can be used to refine or adjust the simulation setup.

The Visualization Module

The Visualization module is the final stage in the Abaqus workflow, where simulation results can be analysed and interpreted. This module provides tools to examine the outputs at each time step of the simulation.

- *Field Outputs*: Key result fields such as stresses, strains, displacements, and temperatures (if applicable) can be viewed. These results are critical for assessing the behaviour of the model under applied conditions.
- *Contour Plots*: Contour plots are used to visually represent result fields on the simulated geometry. These plots provide an intuitive way to identify areas of high stress, deformation, or other key parameters across the model.
- *Numerical Data Extraction*: Numerical results can be extracted for further analysis. Data can be presented in formats such as graphs or tables, allowing detailed evaluation of variables like force-displacement relationships or time-dependent behaviour.
- *Animations*: The module also allows for the creation of animations that depict the evolution of results over time. These animations can be exported as videos or image sequences, providing a dynamic view of the simulation's progression.

B.2. Subroutine Hydrogel

The following subroutine is used in the Abaqus simulations for the expansion calculation of the hydrogel. The subroutine is written in Fortran programming language and compiled with Visual Studio before linking it to Abaqus.

```
1   ------------------------------------------------------
2
3                 SUBROUTINE UHYPER(BI1,BI2,AJ,U,UI1,UI2,UI3,TEMP,NOEL,
4        1 CMNAME,INCMPFLAG,NUMSTATEV,STATEV,NUMFIELDV,FIELDV,
5        2 FIELDVINC,NUMPROPS,PROPS)
6   C=================================================================
7   C     User defined hyperelastic material subroutine
8   C       for gel with Flory-Rehner free-energy function
9   C       to be used in Abaqus Standard
10  C     Fomulated and written by Wei Hong, April 20, 2008
11  C-----------------------------------------------------------------
12  C     Material properties to be passed to the subroutine:
13  C       PROPS(1) - Nv
14  C       PROPS(2) - mu/kT
15  C       PROPS(3) - lambda_0   initial swelling
16  C     State variable:
17  C       TEMP     - wendu
18  C       The initial value of chemical potential should agree
19  C           with the initial swelling, given as follows:
20  C       mu_0/kT = Nv*(1/lambda_0-1/detF0) + ln(1-1/detF0)
21  C                     + 1/detF0+ chi0/detF0^2+2*chi1/detF0^3
22  C       where detF0 = lambda_0^3
23  C     Output
24  C       Free-energy function U(I, J) and its derivatives
25  C       All free-energy density and stress given by the
26  C           calculation are normalized by kT/v
27  C         chi=A0+B0*wendu+(A1+B1*wendu)/AJ/detF0
28  C=================================================================
29  C
30        INCLUDE 'ABA_PARAM.INC'
31  C
32        CHARACTER*80 CMNAME
33        DIMENSION U(2),UI1(3),UI2(6),UI3(6),STATEV(*),FIELDV(*),
34       1 FIELDVINC(*),PROPS(*)
35        REAL(8) Nv, chi, lambda0, detF0, mu_kT, wendu, chi1
36        Nv = PROPS(1)
37        mu_kT = PROPS(2)
38        lambda0 = PROPS(3)
39        detF0 = lambda0**3
40        A0=-12.947
41        A1=17.92
42        B0=0.0449
43        B1=-0.0569
44        wendu = TEMP ! TEMP is used to represent chemical potential
45        chi1=A1+B1*wendu
46        chi0=A0+B0*wendu
47
```

```
48
49          U(1) = Nv/2 * ( 1/lambda0*BI1*AJ**(2.0/3.0) - 3/detF0
50           & - 2/detF0*(3*LOG(lambda0) + LOG(AJ)) )
51           & - chi0/detF0**2/AJ-chi1/detF0**3/AJ**2
52           & - (AJ-1/detF0)*LOG(AJ/(AJ-1/detF0)) - mu_kT*(AJ-1/detF0)
53           & + chi0/detF0+chi1/detF0**2/AJ
54          U(2) = 0
55          UI1(1) = Nv/2/lambda0*AJ**(2.0/3.0)
56          UI1(2) = 0
57          UI1(3) = Nv/3/lambda0*BI1*AJ**(-1.0/3.0)
58           & + (1-Nv)/AJ/detF0 - LOG(AJ/(AJ-1/detF0)) - mu_kT
59           & + chi0/(detF0*AJ)**2+2*chi1/(detF0*AJ)**3
60           & - chi1/detF0**2/AJ**2
61          UI2 = 0
62          UI2(3) = -Nv/9/lambda0*BI1*AJ**(-4.0/3.0) -(1-Nv)/AJ**2/detF0
63           & + 1/AJ/(AJ-1/detF0)/detF0 - 2*chi0/detF0**2/AJ**3
64           & - 6*chi1/detF0**3/AJ**4
65           & + 2*chi1/detF0**2/AJ**3
66            UI2(5) = Nv/3/lambda0 * AJ**(-1.0/3.0)
67          UI3 = 0
68          UI3(4) = -Nv/9/lambda0 * AJ**(-4.0/3.0)
69          UI3(6) = 4*Nv/27/lambda0*BI1*AJ**(-7.0/3.0) + 2*(1-Nv)/AJ**3/detF0
70           & - (2*AJ-1/detF0)/(AJ*(AJ-1/detF0))**2/detF0
71           & + 6*chi0/detF0**2/AJ**4+24*chi1/detF0**3/AJ**5
72           & - 6*chi1/detF0**2/AJ**4
73            RETURN
74            END
75      ------------------------------------------------------
```

B.3. Python: Bending angle calculation Hydrogel-silicone models

The following Python code automates the calculation of the bending angle in the hydrogel models. It relies on the coordinates of the 2 outer particles on the left and the 2 outer particles on the right, illustrated in Figure B.4. Two vectors are constructed and the angle between them is calculated, which is the bending angle.

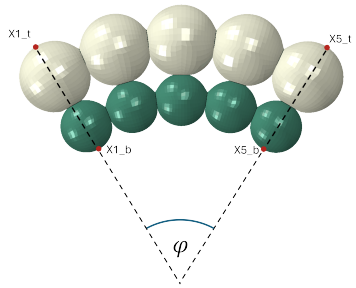

Figure B.4: Nodes on the model highlighted which are used in bending angle calculation.

```python
import math

# Function to parse coordinates from user input
def parse_coordinates(coord_str):
    x, y, z = map(float, coord_str.split(','))
    return x, y, z

# Function to calculate angle between two vectors
def calculate_angle(coords):
    x1_b, y1_b, z1_b = parse_coordinates(coords['x1_b'])
    x1_t, y1_t, z1_t = parse_coordinates(coords['x1_t'])
    x5_b, y5_b, z5_b = parse_coordinates(coords['x5_b'])
    x5_t, y5_t, z5_t = parse_coordinates(coords['x5_t'])

    # Calculate vectors
    v1 = (x1_t - x1_b, y1_t - y1_b, z1_t - z1_b)
    v2 = (x5_t - x5_b, y5_t - y5_b, z5_t - z5_b)

    # Dot product and magnitudes
    dot_product = sum(a * b for a, b in zip(v1, v2))
    magnitude_v1 = math.sqrt(sum(a ** 2 for a in v1))
    magnitude_v2 = math.sqrt(sum(a ** 2 for a in v2))

    # Calculate angle
    angle_rad = math.acos(dot_product / (magnitude_v1 * magnitude_v2))
    return math.degrees(angle_rad)

# Collect input data from the user
print("Enter the coordinates for the following points in the format 'x,y,z':")
x1_b = input("Coordinates for x1_b (bottom of ball 1): ")
x1_t = input("Coordinates for x1_t (top of ball 1): ")
x5_b = input("Coordinates for x5_b (bottom of ball 5): ")
x5_t = input("Coordinates for x5_t (top of ball 5): ")

# Store inputs in a dictionary for processing
coords = {
    'x1_b': x1_b,
    'x1_t': x1_t,
    'x5_b': x5_b,
    'x5_t': x5_t
}

# Calculate the angle
angle = calculate_angle(coords)

# Display the result
print(f"The calculated angle between the vectors is: {angle:.2f} degrees")
```

B.4. Python: Bending angle calculation SMP-SMA models

The following Python code automates the calculation of the bending angle in the SMP models. It relies on the coordinates of three nodes located on the bottom PMMA plate of the deformed structure. The bottom plate is assumed to remain undeformed and flat, allowing any three nodes on its surface to be selected. From these nodes, two vectors are constructed, which are then used to compute a normal vector to the flat surface of the PMMA plate. This normal vector, which is perpendicular to the plate, is then used to calculate the angle between it and the Y-axis. The Y-axis represents the initial orientation of the cylinder in its undeformed state, enabling a precise determination of the bending angle.

```python
from math import sqrt, acos, degrees

# Function to compute vector between two points
def vector(p1, p2):
    return [p2[0] - p1[0], p2[1] - p1[1], p2[2] - p1[2]]

# Function to calculate cross product of two vectors
def cross_product(v1, v2):
    return [
        v1[1] * v2[2] - v1[2] * v2[1],
        v1[2] * v2[0] - v1[0] * v2[2],
        v1[0] * v2[1] - v1[1] * v2[0],
    ]

# Function to compute the magnitude of a vector
def magnitude(v):
    return sqrt(v[0]**2 + v[1]**2 + v[2]**2)

# Function to calculate angle between normal vector and Y-axis (normal to XZ-plane)
def calculate_angle_with_xz_plane(normal_vector):
    y_axis = [0, 1, 0]  # Normal vector of the XY plane
    dot_product = sum(n * y for n, y in zip(normal_vector, y_axis))
    normal_magnitude = magnitude(normal_vector)
    y_magnitude = magnitude(y_axis)  # Always 1
    cos_theta = dot_product / (normal_magnitude * y_magnitude)
    angle = degrees(acos(cos_theta))
    return angle

# Example: Deformed coordinates of three nodes on the surface
node1 = [x1, y1, z1]  # Replace with actual deformed coordinates of Node 1
node2 = [x2, y2, z2]  # Replace with actual deformed coordinates of Node 2
node3 = [x3, y3, z3]  # Replace with actual deformed coordinates of Node 3

# Compute two vectors in the plane of the surface
v1 = vector(node1, node2)
v2 = vector(node1, node3)

# Compute the normal vector using cross product
normal_vector = cross_product(v1, v2)

# Calculate the angle with the XZ plane
angle_with_xz = calculate_angle_with_xz_plane(normal_vector)

# Print the results
print("Normal Vector:", normal_vector)
print("Angle with XZ Plane (degrees):", angle_with_xz)
```

C

Additional results

C.1. Additional mesh-refinement study Hydrogel

In this section additional results can be found for the mesh-refinement study mentioned in section 4.2

The following figures and tables are providing extra information with respect to the mesh refinement study performed.

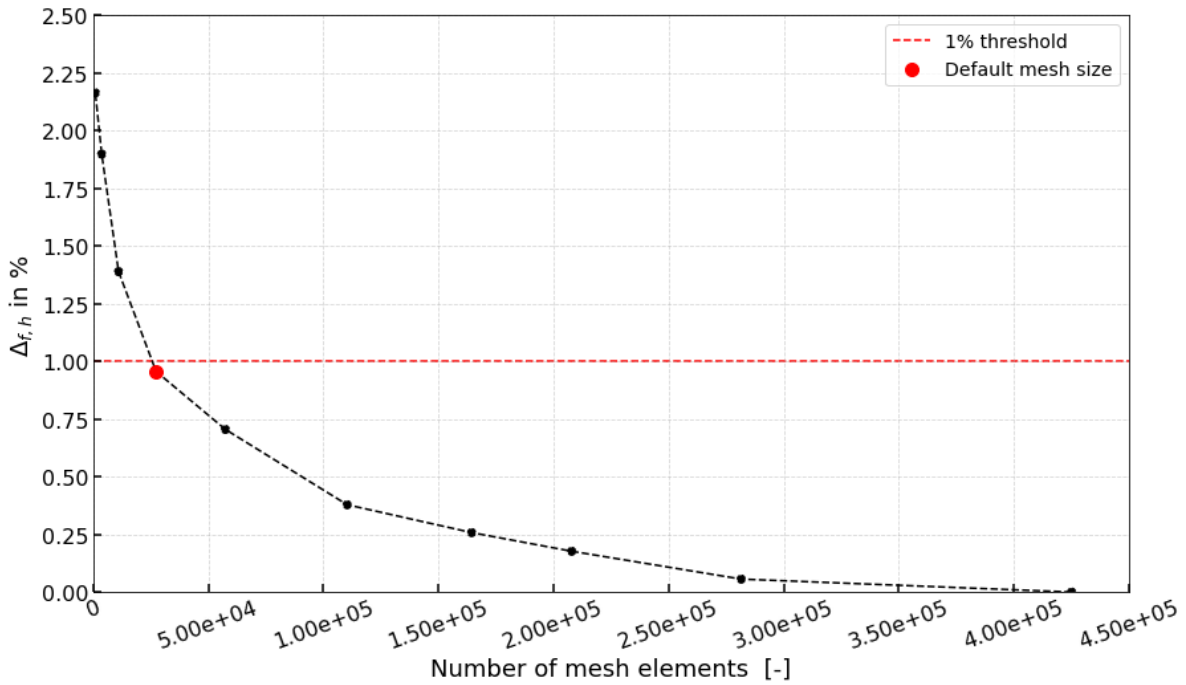

Figure C.1: Mesh elements plotted against the meshsize for hydrogel-silicone models.

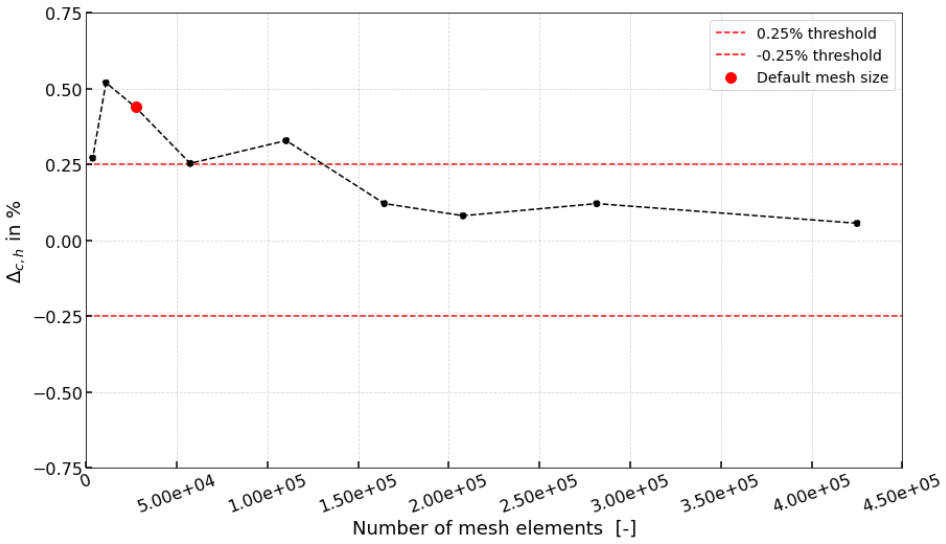

Figure C.2: Plot illustrating the incremental percentage change in bending angle for successive mesh element counts, highlighting how the bending angle evolves with increasing mesh density for Hydrogel-silicone models.

The corresponding data for Figure C.2 can be found in Table C.1

Table C.1: Percentage difference in bending angle for consecutive mesh element counts, calculated relative to the immediately preceding configuration for the hydrogel-silicone models.

Number of elements [-]	Rel. bending angle %
$4.25 \cdot 10^5$	0.0561
$2.82 \cdot 10^5$	0.121
$2.08 \cdot 10^5$	0.0810
$1.64 \cdot 10^5$	0.121
$1.10 \cdot 10^5$	0.329
$5.74 \cdot 10^4$	0.254
$2.73 \cdot 10^4$	0.439
$1.10 \cdot 10^4$	0.519
$3.70 \cdot 10^3$	0.271

C.2. Additional mesh-refinement study SMP

In this section additional results can be found for the mesh-refinement study mentioned in section 5.4. Figure C.3 gives the correlation between the mesh size and the amount of elements generated for the corresponding model.

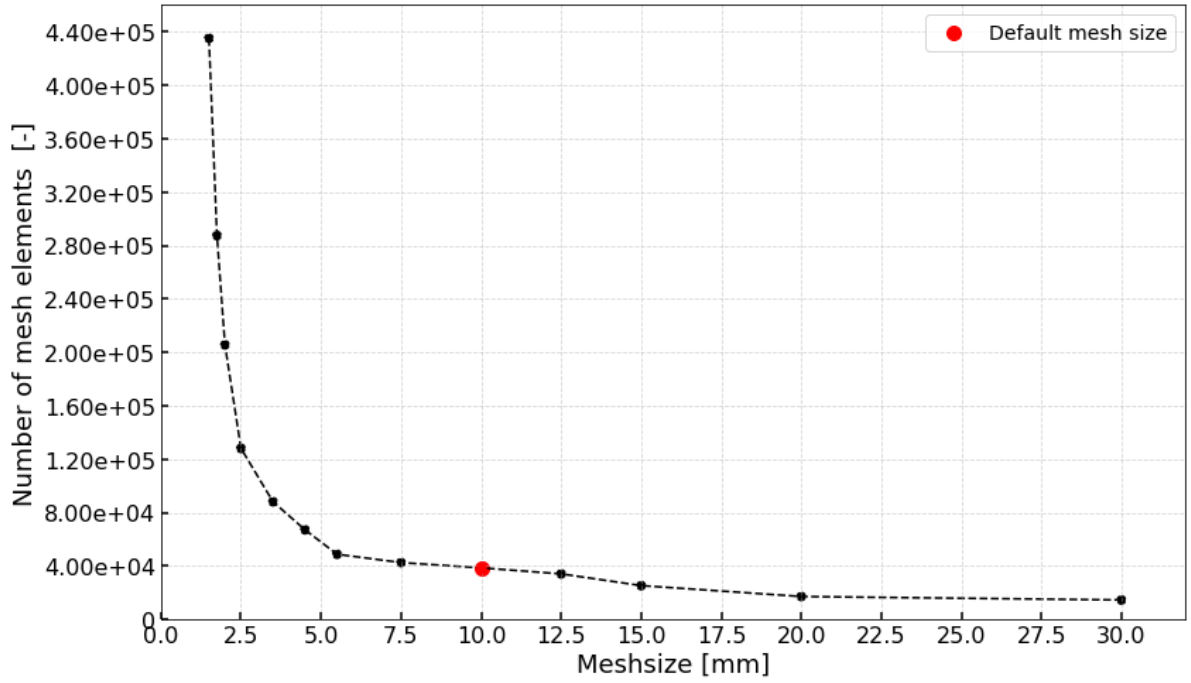

Figure C.3: Mesh elements plotted against the mesh size SMA-SMP models.

The output of mesh-refinement between consecutive trials is plotted in Figure C.4 with the relative change of bending angle for consecutive data points in percentages given for the used element amounts. Equation 5.9 was used for this study. corresponding data for this plot can be found in Table C.2 The threshold is indicated with the two horizontal red lines, indicating the +2% and -2% limit.

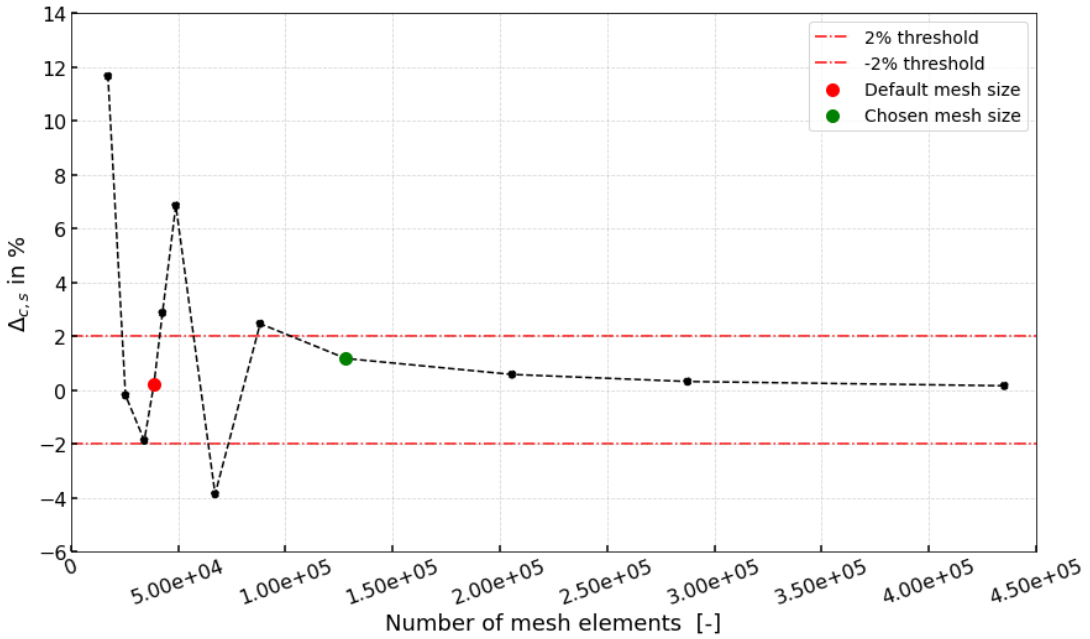

Figure C.4: Plot illustrating the incremental percentage change in bending angle for successive mesh element counts, highlighting how the bending angle evolves with increasing mesh density for SMP-SMA models.

The corresponding data for Figure C.4 can be found in Table C.2

Table C.2: Percentage difference in bending angle for consecutive mesh element counts, calculated relative to the immediately preceding configuration for the SMP-SMA models.

Number of elements [-]	rel. bending angle %
$4.35 \cdot 10^5$	0.16
$2.87 \cdot 10^5$	0.32
$2.06 \cdot 10^5$	0.58
$1.28 \cdot 10^5$	1.17
$8.82 \cdot 10^4$	2.47
$6.72 \cdot 10^4$	-3.86
$4.89 \cdot 10^4$	6.85
$4.27 \cdot 10^4$	2.87
$3.87 \cdot 10^4$	0.22
$3.42 \cdot 10^4$	-1.87
$2.55 \cdot 10^4$	-0.19
$1.73 \cdot 10^4$	11.7
$1.47 \cdot 10^4$	-

C.3. Additional visuals for other geometries tested

An overview is given here of all the deformed states of the other geometries tested in section 5.6.

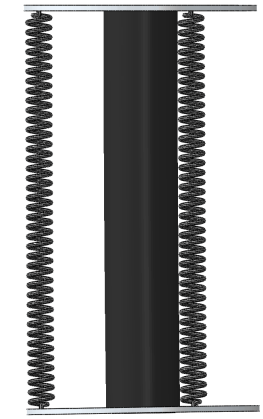

(a) The deformed regular geometry

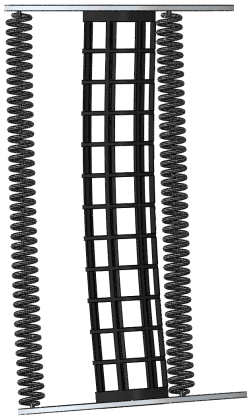

(b) The deformed square geometry

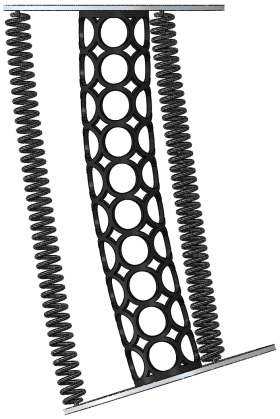

(c) The deformed circle geometry

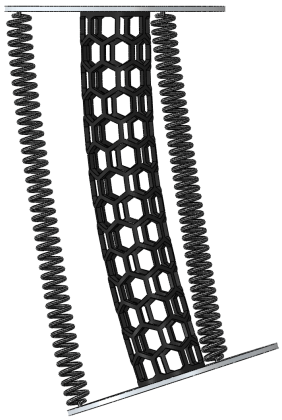

(d) The deformed hex geometry

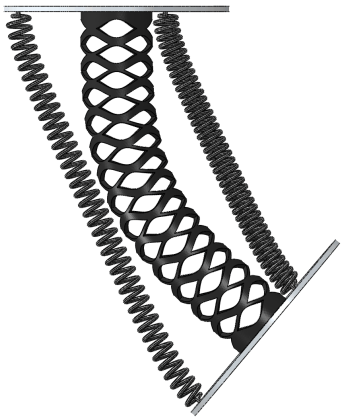

(e) The intelligent block geometry

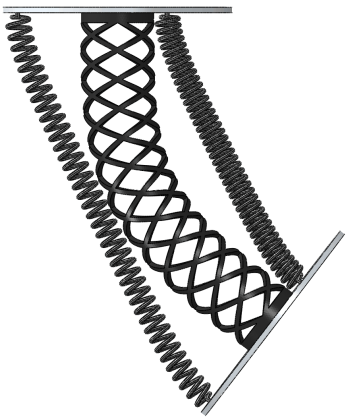

(f) The deformed diamond geometry

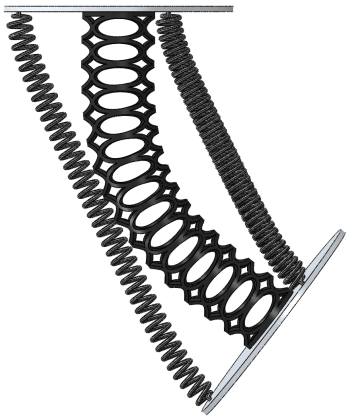

(g) The deformed ellipse geometry

Figure C.5: Corresponding side views (ZX) to display bending angles for each different repeated structure.

D

Additional figures for geometries used

D.1. Additional dimensions SMP models

...

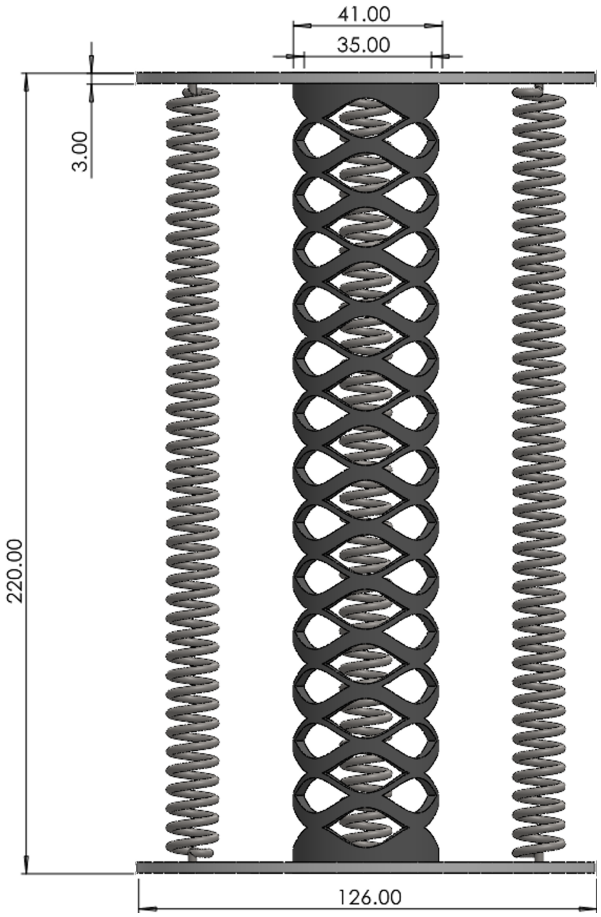

Figure D.1: Global dimensions of the SMP cylinder design which is used as base geometry in the analysis.

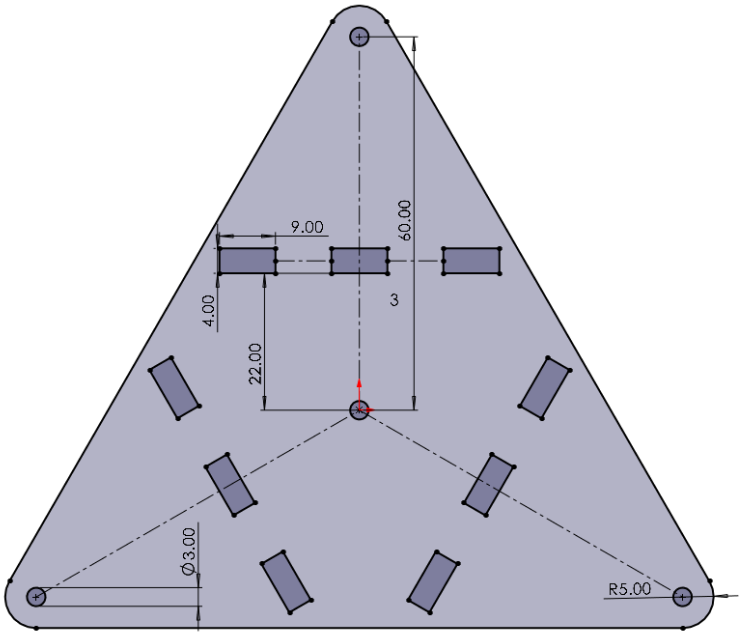

Figure D.2: Dimensions of the PMMA board used in the third SMP design.

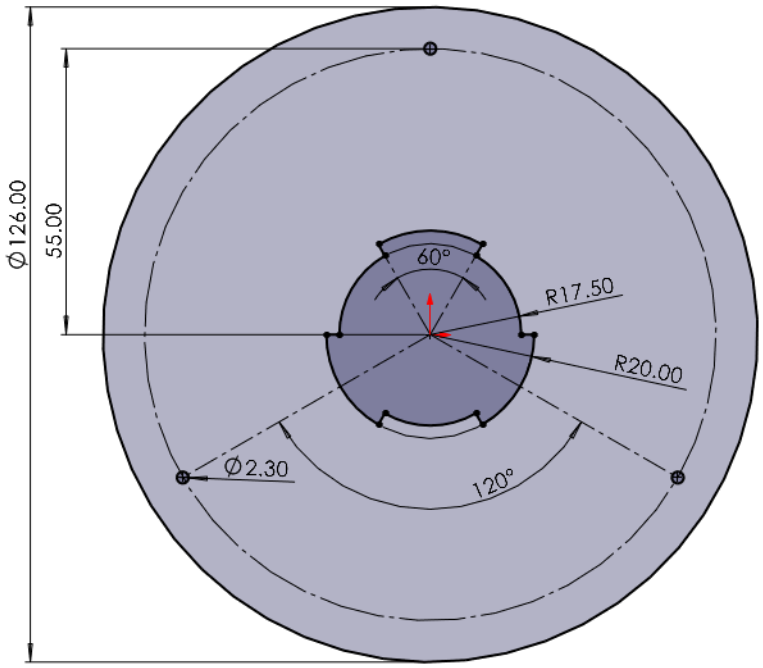

Figure D.3: Dimensions of the PMMA board used in the base design of the SMP geometry, for a cylinder thickness of 2.5 mm

E

Practical experiments for design choices

This chapter explores the design and testing of 3D-printed structures intended for SMP actuators, focusing on the challenges associated with their fabrication and performance. The experiments address key issues such as layer adhesion, structural integrity, and thermal responsiveness during the 3D printing process, particularly with materials like SMP and PLA. Observations from testing these printed structures provided valuable insights into their mechanical and shape-morphing behaviour, revealing critical limitations and guiding refinements in the SMP design. The findings form the basis for optimizing the 3D printing process and improving the functionality of the final actuator system.

Manufacturing effects of 3D printing of plates or strips

- **The printing direction** plays a critical role in determining the quality of the specimen. It is recommended that the printing path be aligned parallel to the natural curves of the design. Printing in this orientation allows for smoother, continuous layering, which preserves the intended curvature and enhances surface finish. In contrast, if the print direction is misaligned with the curves, the curvature is constructed in incremental steps, resulting in a lower-quality specimen with visible layer lines and reduced smoothness, which can be seen in Figure E.1. This incremental approach can also introduce small structural weaknesses due to the uniformity of the layers.
- **The nozzle** significantly impacts the printing quality of the specimen. Residual molten PLA adhered to the nozzle can adversely affect subsequent prints. This impact is particularly evident in the initial layer deposited on the printing plate, which often serves as the foundational layer for the entire structure. When this base layer is compromised by residual material, the stability and quality of successive layers are diminished, impairing the overall structural integrity of the print.
- **Printing plates** that are unclean can have several detrimental effects on the printed structure, ultimately compromising the quality and reliability of the final product. Residual particles, dust, or previously deposited material on the plate can interfere with adhesion, causing the initially printed layers to bond unevenly. Poor adhesion at the base layer can lead to warping, shifting, or detachment during the printing process, which disrupts layer alignment and weakens the structural integrity of the print.
- **Layer heights** that do not match the geometry can result in dimensional inaccuracies, particularly in regions where finer details or smaller features are essential. A 0.4 mm layer height may not capture details intended for 0.3 mm, causing deviations in the printed object's dimensions and potentially affecting the fit or function of the part. In some cases, the printer might not be able to create thin parts of a structure leading to disconnected prints, as can be seen in Figure E.2

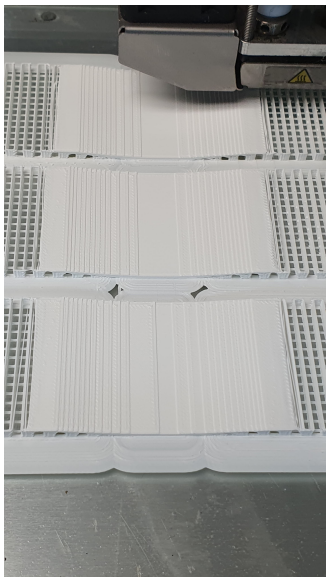

Figure E.1: Single wave samples printed with curves created in layered steps.

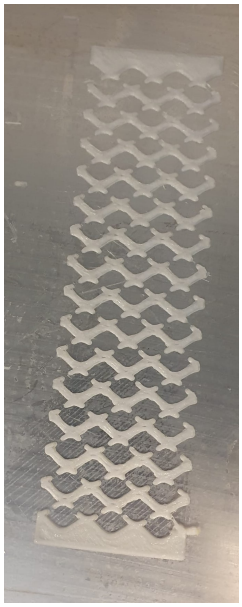

Figure E.2: Flat sample printed with disconnections due to a mismatch in the minimum printer layer thickness and geometrical thickness.

Experimental results - curved strips

- **Elevated temperatures** (exceeding 90°C) lead to the separation of PLA layers, resulting in gaps within the geometry that significantly reduce the structural integrity. Additionally, these cavities create variations in the strip's thickness along its length, compromising uniformity. At such high temperatures, the material's strength diminishes to the extent that gravitational forces alone can induce substantial deformation, requiring minimal external force to produce considerable structural changes.
- **Shrinkage** occurs when fibres are oriented parallel to the loading direction. Upon heating, these fibres contract, resulting in an overall reduction in the strip's length. This decrease in length is offset by an increase in thickness in certain sections of the strip, producing a characteristic wave pattern along its outer surface.

Experimental results - folding plates

- **Buckling** presents a significant challenge for specimens with a plate geometry. When compressive loads are applied to opposite sides of the plate, buckling occurs, leading to localized structural collapse. This deformation, often concentrated in the middle of the specimen, hinders the folding process of the entire sample by compromising its structural stability. A few examples of this can be found in Figure E.3a and Figure E.3b.

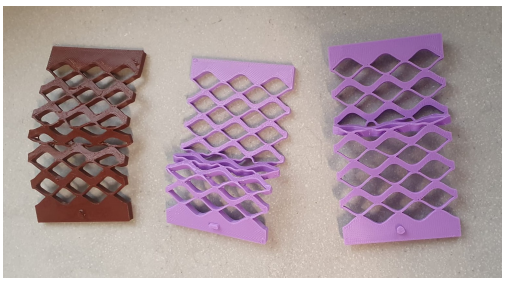

(a) Buckled plates

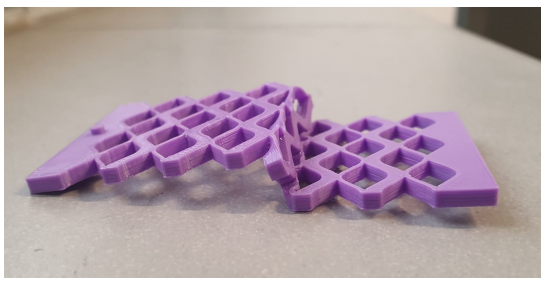

(b) Side view of a buckled plate.

Figure E.3: Examples of buckling in the middle of the sample SMP plates with the intelligent block design.

Experimental results - cylinders

- These cylinders are also easy to deform with warm water. Since no support material was left, the entire structure could deform and compress.
- The cross-section might not be perfectly round after deforming, since it's hard to exert force on the geometry on all sides equally, especially when doing this by hand. This is something that could be fixed with a thicker cylinder. The cylinder in question used a thickness of 1.5 mm.
- The geometry does not fully recover to its original state, as some minor loss in length remains. However, this can be mitigated by performing the heating process twice, with the second cycle showing minimal shortening.